

1 **AFP: A Proposal to Install Proton Detectors at**
2 **220 m around ATLAS to Complement the ATLAS**
3 **High Luminosity Physics Program**

4 L. Adamczyk^a, R. B. Appleby^{b,c}, P. Bańka^d, M. Boonekamp^e, A. Brandt^f, P. Bussey^g,
5 M. Campanelli^h, E. Chapon^e, J. Chwastowski^d, B. Cox^b, E. Delagnes^e, M. Duerenⁱ,
6 A. Farbin^f, J.-F. Genat^j, H. Grabas^e, Z. Hajduk^d, H. Hakopian^k, Z. Janoska^l, O. Kepka^l,
7 A. Kupčo^l, V. Kus^l, S. Liu^m, A. Pilkington^{b,n}, J. Pinfold^m, P. Ponsot^e, K. Potter^{b,o},
8 M. Przybycień^a, M. Rijssenbeek^q, C. Royon^e, P. Ruzicka^l, L. Schoeffel^e, R. Soluk^m,
9 J. Soukup^m, R. Staszewski^{d,e}, T. Sykora^r, H. Stenzelⁱ, M. Tasevsky^l, T. Tic^l,
10 M. Trzebiński^{d,e}, J. Turnau^d, V. Vacek^s, A. Valkarova^r, V. Vrba^l, S. Watts^b, and
11 M. Zeman^{e,l}

12 ^aFaculty of Physics and Applied Computer Science, AGH-University of Science and Technology,
13 Cracow, Poland

14 ^bUniversity of Manchester, UK

15 ^cCERN, Geneva, Switzerland

16 ^dInstitute of Nuclear Physics, Polish Academy of Sciences, Kraków, Poland

17 ^eIRFU, CEA Saclay, France

18 ^fUniversity of Texas Arlington, USA

19 ^gUniversity of Glasgow, UK

20 ^hUniversity College London, UK

21 ⁱUniversity of Giessen, Germany

22 ^jLPNHE, University of Paris 6-7, France

23 ^kUniversity of Yerevan, Armenia

24 ^lInstitute of Physics, Academy of Sciences of the Czech Republic, Na Slovance 2, CZ - 18221 Praha 8,
25 Czech Republic

26 ^mUniversity of Alberta, Canada

27 ⁿUniversity of Durham, UK

28 ^oCockcroft Institute, UK

29 ^qStony Brook University, USA

30 ^rCharles University, Prague, Czech Republic

31 ^sCzech Technical University, Prague, Czech Republic

32 May 5, 2011

Abstract

34 We present the Technical Proposal to build and install forward proton detectors at 220 m from
35 the interaction point on both sides of the ATLAS experiment. The detectors would be designed
36 to operate at high instantaneous luminosities of up to $10^{34} \text{ cm}^{-2}\text{s}^{-1}$. The primary goal is to
37 enhance the ATLAS baseline physics program, particularly the anomalous couplings between γ
38 and W or Z as well as QCD studies. AFP will allow Higgsless and Extra-dimension models to
39 be probed with an unprecedented precision by searching for anomalous couplings between γ and
40 W/Z . We propose the installation of moveable beam pipes housing precision silicon and timing
41 detector to enable this physics program during the 2013-2014 shutdown.

Contents

43	1 Introduction	5
44	2 Physics Case	7
45	2.1 Introduction	7
46	2.2 Acceptance	8
47	2.3 Photon-photon physics	10
48	2.3.1 Lepton pair production	10
49	2.3.2 Vector boson production	11
50	2.4 Diffraction and QCD	12
51	2.5 Summary	13
52	3 Hamburg Beampipe	16
53	3.1 Introduction	16
54	3.2 Hamburg pipe design requirements	16
55	3.3 Movable pipe design	17
56	3.3.1 Pocket design	19
57	3.3.2 Motorization and detector system positioning	20
58	3.3.3 Beam position monitors and alignment	20
59	3.4 System performance and operation	24
60	3.5 Machine induced backgrounds and RF effects	24
61	3.6 Ongoing research and development	25
62	3.7 Conclusions	25
63	4 The Silicon Tracking Detector	26
64	4.1 Introduction	26
65	4.2 Tracking system requirements	26
66	4.3 Tracking system design	27
67	4.3.1 The silicon sensor	27
68	4.3.2 The readout chip	31
69	4.3.3 Location and layout	32
70	4.4 System performance and operation	32
71	4.4.1 Electromagnetic environment	32
72	4.4.2 Radiation tolerance	32
73	4.4.3 Cooling	33
74	4.5 Ongoing research and development	34
75	4.6 Conclusion	34

76	5 Fast Timing System	35
77	5.1 Introduction	35
78	5.2 Timing system requirements	35
79	5.3 Timing system components	36
80	5.3.1 The detectors	36
81	5.3.2 The electronics	37
82	5.3.3 Reference clock	40
83	5.4 Timing system equipment	41
84	5.5 Timing system performance	41
85	5.6 Ongoing research and development	44
86	5.6.1 Detector R&D	44
87	5.6.2 MCP-PMT R&D	44
88	5.6.3 Electronics R&D	45
89	5.7 Timing summary	46
90	6 Timescale, Resources, and Conclusions	47
91	6.1 Timeline	47
92	6.2 Installation	48
93	6.3 Personnel	49
94	6.4 Costing and available or requested budget	49
95	6.5 Conclusion	50
96	7 Appendix I: LHC physics debris collimation studies and their impact on AFP	54
97	detectors acceptance	54
98	7.1 Introduction	54
99	7.2 IR layout and present collimation scheme	54
100	7.3 Optimal collimator settings as studied with beam optics calculations	55
101	7.4 Numerical simulations setup	57
102	7.5 Numerical simulation results	59
103	7.5.1 PTC loss maps without collimators	59
104	7.5.2 PTC loss maps with single collimators	61
105	7.5.3 PTC loss maps with different collimator schemes	61
106	7.6 Conclusion	63
107	8 Appendix II: LHC Optics, Acceptance, and Resolution	65
108	8.1 Beamline	65
109	8.2 Detector Acceptance	66
110	8.3 Momentum determination	69
111	8.4 Mass measurement	74
112	8.5 Calibration	75
113	8.6 Summary	77
114	9 Appendix III: A possible extension of the AFP project using 420 m detectors	78
115	9.1 Physics program in 220+420 stage	78
116	9.2 Central Exclusive Production	78
117	9.2.1 $h \rightarrow b\bar{b}$	79
118	9.2.2 $h \rightarrow \tau\tau$	80
119	9.2.3 $h \rightarrow 4\tau$	80
120	9.2.4 Photon-Photon physics	82

121	9.2.5	Supersymmetric particle production	82
122	9.3	New connection cryostat	83
123	9.4	Summary	87

Chapter 1

Introduction

This Technical Proposal presents Stage I of the ATLAS Forward Proton (AFP) upgrade for ATLAS Upgrade Phase 0. The proposal consists of a plan to add high precision detectors at ~ 220 m upstream and downstream of the ATLAS interaction point to detect intact final state protons scattered at small angles and with small momentum loss. The capability to detect *both* outgoing protons in diffractive and photoproduction processes in conjunction with the ATLAS central detector enables a rich QCD, electroweak and beyond the Standard Model experimental program.

A prime process of interest is Central Exclusive Production (CEP), $pp \rightarrow p + \phi + p$, in which the central system ϕ may be, for example, a pair of W or Z bosons, a pair of jets, or a neutral Higgs boson. The observation of a new particle in the CEP channel allows for a direct determination of its quantum numbers, since to a good approximation only 0^{++} central systems can be produced in this manner. Furthermore, tagging both protons allows the mass of the centrally produced system ϕ to be reconstructed with a resolution (σ) between 3 GeV and 6 GeV per event if both protons are tagged at 220 m, irrespective of the decay products of the central system. Tagging both protons allows the probing of anomalous couplings between γ and W or Z with an unprecedented precision. Simulations show that it is possible to improve the LEP sensitivity by four orders of magnitude with 30 fb^{-1} , which should be sufficient to discover or rule out Higgsless or Extra-dimension models.

To enable this physics program, we propose to install movable beam pipes at ± 216 m and ± 224 m from the ATLAS main detector. This specialized beam pipe will both house the AFP detectors, and allow them to be positioned within a few mm of the circulating beam. The primary detector is a silicon tracking spectrometer which uses points measured along the track at the two stations in conjunction with the LHC dipole and quadrupole magnets to reconstruct the momentum and scattering angle of the final state protons. The acceptance covers fractional momentum losses in the range $0.02 < \xi < 0.2$. For events in which both protons are tagged, this corresponds to a range of central masses from several hundred GeV (depending on the distance of the detectors from the beam) to beyond 1 TeV. The movable beam pipe will also contain precision timing detectors to suppress overlap combinatoric backgrounds.

This proposal was solicited by ATLAS Executive Board following an extensive review of the AFP Letter of Intent [1], which was submitted to ATLAS in fall of 2008. Details of the review process are available at [2]. The major concerns of the review committee (listed here for reference) have largely all been addressed:

1. **Consistency of the AFP schedule with the LHC schedule:** we have addressed this with our staging plan and discuss the key milestones in Chapter 6.

- 160 2. **Silicon detector lifetime issues:** we have removed this concern by switching from the
161 FE-I3 to FE-I4 chip, which is much better designed to deal with the high expected flux
162 rates.
- 163 3. **Micro-channel plate PMT lifetime issues:** these have been reduced by R&D with
164 Hamamatsu, Photonis, and Photek as well as improved detector design; the requirements
165 are also less significant in the moderate luminosity expected up to about 2016.
- 166 4. **Trigger issues:** these include concerns about trigger bandwidth, latency, method, and
167 simulation. Dedicated triggers are not going to be needed due to the acceptance limitation
168 at low mass, removing this entire category from concern. Nevertheless, we will employ a
169 simple Level 1 trigger using the timing system, paving the way for a more sophisticated
170 trigger in Stage II (equivalent timescale to Upgrade Phase I).
- 171 5. **Machine issues:** these include concerns about interference with the collimation system
172 and the cryostats as well as a safety review. We developed an alternate collimation scheme
173 that protects critical LHC components while maintaining sufficient acceptance to enable
174 the AFP physics program. We have deferred the cryostat issues by moving the 420 m
175 installation to Stage II, although we note that the cryostat bypass that we developed
176 has been largely incorporated into the LHC cryo-collimator design, so this is no longer
177 a significant concern. The safety review is only possible after the Technical Proposal is
178 approved, since it requires interaction with the accelerator experts.

179 The outline of this document is as follows: Chapter 2 presents the physics motivation of
180 the proposed 220 m system, Chapter 3 describes the Hamburg movable beampipe solution for
181 housing both silicon tracking and fast timing detectors, Chapter 4 describes the silicon tracking
182 detector, Chapter 5 describes the timing detector, and Chapter 6 present the conclusions, as
183 well as a brief discussion of resources, and a project timeline. The Appendix includes details on
184 collimation and acceptance studies, and a potential future extension of the project by adding
185 detectors at 420 m, which would greatly improve the low mass acceptance.

Chapter 2

Physics Case

2.1 Introduction

The purpose of the new forward detectors described in this technical proposal is to open a possibility to identify and record events with leading intact protons emerging from inelastic collisions occurring in ATLAS. Historically, measurements involving intact leading protons are mainly associated with diffractive analyses (involving soft pomeron exchanges). Probing the structure of a nucleon under special conditions which do not lead to its disruption enhances our understanding of hadrons beyond what is achieved solely by conventional measurements.

With the high energy proton beams at the LHC, forward physics enters a new era. The exclusive productions with leading protons in the event have sizeable cross sections and can be exploited to give very precise electroweak or SUSY measurements. Detecting the leading protons on either one or both sides of the central detector broadens the spectrum of physics analyses that can be carried out and maintains the competitiveness of ATLAS with other experiments, in particular with CMS, which has a better coverage in the forward region and thus has higher sensitivity to the above-mentioned processes.

One possibility for a system ϕ to be produced exclusively is via an exchange of two photons $pp \rightarrow p(\gamma\gamma)p \rightarrow p + \phi + p$ [3, 4, 5]. The two photons may couple to electroweak bosons, leptons or SUSY particles. A schematic diagram of these exchanges is shown in Figure 2.1. The ‘+’ sign denotes the regions devoid of activity, often called rapidity gaps. The cross section falls very quickly as a function of the photon transverse momentum, and the photons move mainly in the longitudinal direction. Outgoing protons therefore scatter at very small angles. The radiation of collinear photons off protons is largely calculable within perturbative Quantum Electrodynamics, and the cross sections have relatively small theoretical uncertainties, especially since rescattering corrections are small. These processes can therefore provide unique precision measurements of the electroweak sector of the Standard Model (SM) and reveal details of the electroweak symmetry breaking also in the case where there is no Higgs boson. The advantage of AFP is that by tagging the outgoing protons and with few relatively simple additional requirements in the central detector, the selected event is ensured to be initiated by two-photons. Electroweak tests can therefore be performed with higher precision than by using the central detector only. As we will see in the following of this chapter, this process will allow to probe anomalous couplings between γ and W/Z with a unprecedented precision at the LHC.

A second topic consists of the exclusive diffractive production. Central exclusive production (CEP) of new particles has received a great deal of attention in recent years [6, 7, 9]. The production is driven by an exchange of a di-gluon system. The color flow is screened by an exchange of an additional gluon such that the produced system is colorless. Due to the very

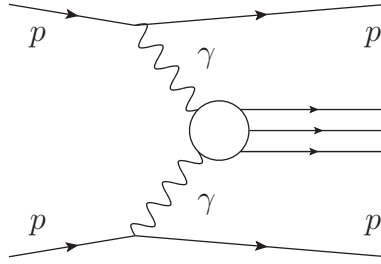


Figure 2.1: Exclusive production occurring via the exchange of di-photon system.

222 small scattering angles of the outgoing protons, this system obeys to a good approximation a J_z
 223 $= 0$, C-even, P-even, selection rule, so that the quantum numbers of the produced system are
 224 constrained, irrespective of the decay channel.

225 It is worth noticing that diffractive physics consists of two groups of topics:

- 226 • “bread-and-butter” physics, such as single diffraction or double pomeron exchange mea-
 227 surements in the jet, Z , W , J/Ψ channels, and the search of exclusive production in the
 228 jet channel for instance. Most of these physics topics can either be done using special
 229 stores at low instantaneous luminosity to avoid suffering from pile-up, or using prescaled
 230 triggers. This topic follows the great results obtained in diffraction at HERA (H1/ZEUS)
 231 and Tevatron (CDF/D0).
- 232 • “explatory” physics and we study in particular the search for anomalous couplings between
 233 γ and W or Z bosons, which allow to probe higgsless or extra-dimension models with an
 234 unprecedented precision at the LHC.

235 The particular physics program of two-photon and CEP physics depends strongly on the
 236 acceptance of the ATLAS Forward Proton Detectors in terms of the mass of the exclusive
 237 system $W^2 = s\xi_1\xi_2$, where ξ is the proton fractional momentum loss and s is the centre-of-mass
 238 energy of the pp collision. The range in ξ to which detectors are sensitive are determined by
 239 the geometrical acceptance of the forward detectors. Reaching as low W masses as possible is
 240 desired to maintain high production yields because diffractive and exclusive production cross
 241 sections roughly fall as $1/\xi$.

242 As discussed in Appendix III, the production and installation of 420 m detectors is much
 243 more intricate than for those at 220 m since they require the installation in the cold region of
 244 the LHC and a dedicated cryogenic design. The detector acceptance in fractional momentum
 245 loss acceptance at 220 m is of the order $\xi \sim 1 - 10\%$, while it is $\xi \sim 0.1 - 1\%$ for those
 246 installed at 420 m. The physics program of the AFP project in the baseline configuration with
 247 detectors at 220 m only is reviewed in this document. They provide an acceptance to relatively
 248 large exclusive masses. The program of a possible extension of the project with more distant
 249 detectors is briefly summarized in Appendix III.

250 2.2 Acceptance

251 To obtain the acceptance in fractional proton momentum ξ and thus the physics possibilities
 252 of our detector, we assume the existence of three collimators called TCL4, TCL5 and TCL6
 253 in front of our detectors at 220 m as described in Fig. 2.2. Compared to the default present
 254 situation, this solution assumes that the positions of TCL4 and TCL5 are at 30 and 50σ from

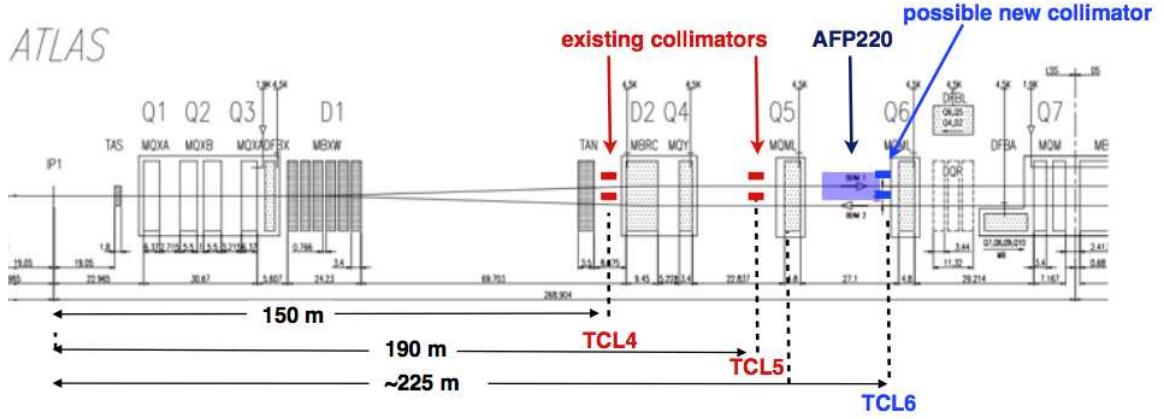


Figure 2.2: Layout of the straight section on the right side of ATLAS.

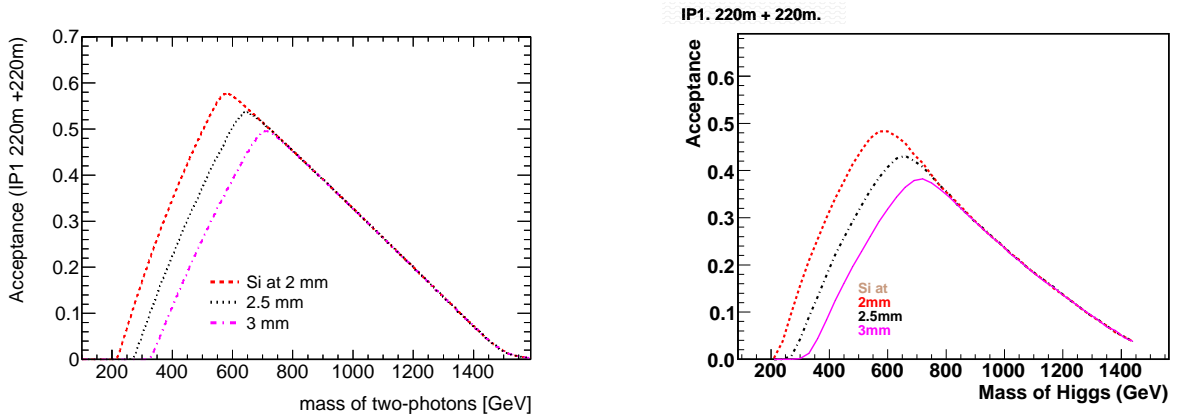


Figure 2.3: Geometrical acceptances due to a limited coverage of the forward detectors in ξ and t in terms of central exclusive mass two-photon exclusive (left) and central exclusive (right) productions.

255 the beam respectively ¹. In addition, the TCL6 new collimator is positioned at 40σ from the
 256 beam. This solution allows to keep a good acceptance for diffracted protons and was admitted
 257 as a possible alternative to the present scheme by the LHC Vacuum group. It is presented in
 258 detail in Appendix I of this technical proposal.

259 The acceptance as a function of mass produced in exclusive events is depicted in Figure 2.3 for
 260 two-photon physics (left) and CEP production (right). They are obtained by means of a complete
 261 simulation of the scattered protons through the LHC optical elements; the proton tracking
 262 through the LHC beam line is discussed in Appendix II. It is shown for various distances of the
 263 forward detectors from the beam - 2, 2.5, and 3 mm, which denote the “optimist”, “realistic”,
 264 and “pessimistic” configuration scenarios. In all cases, the 220 m acceptance removes events
 265 below ~ 300 GeV. Due to larger tails in mass for two-photon production, the acceptance is in
 266 general slightly larger than in CEP. In particular, for the baseline detector distance of 2.5 mm
 267 the acceptance at its maximum $W = 650$ GeV is by about 10% higher than the acceptance for
 268 central exclusive production.

¹We recall that the assumed position of TCL4 and TCL5 for the default scenario is at 15σ from the beam which kills fully the acceptance of our 220 m detectors.

269 Furthermore, the reduced mass acceptance significantly lowers the yield of CEP processes.
 270 For example, only a couple of events are expected for exclusive di-jets with $p_T^{jet} > 60$ GeV. The
 271 double proton tag is required in order to remove pile-up background, in which non-diffractive
 272 di-jet event is overlaid with soft diffractive events giving a proton hit in forward detectors using
 273 the forward detectors. This can be done by comparing the jet and the reconstructed kinematics.
 274 Due to its small yield, the exploratory physics program using central exclusive processes (Higgs
 275 bosons...) is not considered with 220 m detectors only and the focus is made on the two-photon
 276 exclusive production and the standard QCD diffractive measurements. However, the search for
 277 exclusive diffractive events in the jet channel as performed by the CDF collaboration is still
 278 possible [10].

279 2.3 Photon-photon physics

280 In this section we consider inelastic photon-photon collisions, $pp \rightarrow p(\gamma\gamma)p \rightarrow pXp$. The central
 281 system in the final state is separated on each side by a large rapidity gap from forward protons.
 282 Photon-photon fusion opens up a rich electroweak program that complements the QCD physics.
 283 Recently, the exclusive two-photon production of lepton pairs has been observed by the CDF
 284 collaboration [11] and is in good agreement with the theoretical predictions.

285 2.3.1 Lepton pair production

286 Two-photon exclusive production of muon pairs has a well known QED cross section, including
 287 very small hadronic corrections. Thanks to its distinct signature, the selection procedure is very
 288 simple: two muons within the central detector acceptance ($|\eta| < 2.5$), with transverse momenta
 289 above a minimum value $p_T > 10$ GeV depending on the experimental trigger. Using only the
 290 detectors at 220 m detectors to tag the protons, the majority of the events with muon $p_T > 6$
 291 GeV are not in the detector acceptance. For instance, for a detector position at 2.5 mm from
 292 the beam, a muon p_T cut at 15 GeV is enough to keep all events when the protons are detected
 293 at 220 m. We choose a trigger level at 13 GeV which is conservative. To get enough statistics
 294 in order to monitor the instantaneous luminosity, it is clear that one needs to go lower in muon
 295 p_T and the 420 m detectors are needed in addition.

296 After applying this selection criterion and requiring one forward proton tag, the cross section
 297 is ~ 25 fb for the detector distance of 2.5 mm from the beam. Due to the exclusivity of the event,
 298 the dilepton p_T is very much correlated with the proton ξ and cross section is very sensitive to the
 299 position of the edge of the detector with respect to the beam. After requesting one proton tag in
 300 detector placed at 2.0 mm from the beam, only muons with $p_T > 10$ GeV can be measured. This
 301 means that triggers with lower p_T thresholds are not necessary. Using di-muon trigger may help
 302 to keep prescales low for high machine luminosities. As discussed in Appendix II, two-photon
 303 dimuon events can be used for calibration of 220 m detectors to a required accuracy with about
 304 hundred of such events.

305 If 420 m taggers can be installed, the cross section increases to 1.3 pb [4, 5]. This corresponds
 306 to ~ 50 muon pairs detected in a 12 hour run at a mean luminosity of 10^{33} cm⁻²s⁻¹. Apart for
 307 calibration purposes, the large event rate coupled with a small theoretical uncertainty makes
 308 this process a potentially important candidate for the measurement of the absolute LHC lumi-
 309 nosity [12]. The e^+e^- production can also be studied at ATLAS, although the trigger thresholds
 310 will be larger and hence the final event rate reduced.

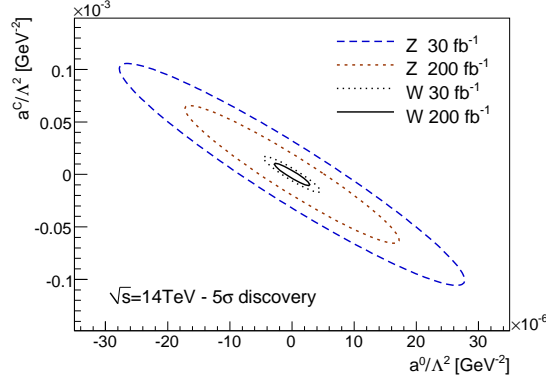


Figure 2.4: 5σ discovery contours for all the WW and ZZ quartic couplings at $\sqrt{s} = 14$ TeV for luminosity of 30 fb^{-1} and 200 fb^{-1} . See [4] for notation.

311 2.3.2 Vector boson production

312 This section describes the main physics topics of AFP which allows to probe electroweak sym-
 313 metry breaking with unprecedented precision.

314 The cross section of exclusive two-photon production of W boson pairs is expected to be
 315 about 100 fb at the LHC [5]. The majority of such events would require one proton tagged at
 316 220 m and one proton tagged at 420 m due to the relatively large mass of the central system.
 317 The easiest selection consists of large missing E_T^{miss} and large p_T of electron or muon. Asking
 318 $E_T^{\text{miss}} > 20 \text{ GeV}$ and $p_T > 25 \text{ GeV}$ together with the double proton tag in 220 m detectors results
 319 in ~ 10 events per 30 fb^{-1} with zero background expected from QCD. The overlap background
 320 is expected to be small due to an intrinsically large cut on mass required by forward 220 m
 321 detectors.

322 Moreover, vector boson pair production provides an opportunity to investigate anomalous
 323 gauge boson couplings, in particular the anomalous quartic gauge couplings (QGCs) $\gamma\gamma VV$.
 324 Note that in the SM, the tree-level pair production of Z bosons by photon-photon fusion is
 325 not allowed and any observation of exclusive ZZ final states implies an anomalous coupling.
 326 Conversely, the SM does allow both triple and quartic gauge couplings, $\gamma W^+ W^-$ and $\gamma\gamma W^+ W^-$
 327 and the anomalous contribution would exist as an excess over the SM prediction.

328 The sensitivity of a forward detector system to anomalous gauge couplings has been investi-
 329 gated in [4, 5] for the leptonic decays $\gamma\gamma \rightarrow W^+ W^- \rightarrow l^+ l^- \nu_l \bar{\nu}_l$ and $\gamma\gamma \rightarrow ZZ \rightarrow l^+ l^- j j$, using
 330 the signature of two leptons (e or μ). In the second set of references, a complete analysis with
 331 numerous diffractive and two-photon backgrounds was carried out for the $220+420 \text{ m}$ detectors.
 332 All background and signal events were considered and passed through a fast simulation of the
 333 ATLAS detector. The anomalous coupling appears predominantly at high two-photon masses
 334 and is selected applying $E_T^{\text{miss}} > 20$, $p_T > 25 \text{ GeV}$, $|\eta| < 2.5$ of the leading lepton and requiring
 335 large invariant reconstructed mass in forward detectors $W > 800 \text{ GeV}$. For instance, the $\gamma\gamma \rightarrow ll$
 336 background is mostly suppressed by a requirement on the difference in azimuthal angle between
 337 the leptons, and requiring high mass produced in the central detector (cut on W) and on the
 338 reconstruction of high p_T leptons gets rid of most of the background. The results are presented
 339 as 5σ discovery contour limits in Figure 2.4, and in Table 2.1. The uncertainties on these limits
 340 are quite low. The QED backgrounds are perfectly known from a theoretical point of view and
 341 this background does not suffer much from a theoretical uncertainty. This is not the case for the
 342 double pomeron exchange background but this background is very small after all requirements

Couplings	OPAL limits [GeV ⁻²]	Sensitivity @ $\mathcal{L} = 30$ (200) fb ⁻¹	
		5 σ	95% CL
a_0^W/Λ^2	[-0.020, 0.020]	5.4 10 ⁻⁶ (2.7 10 ⁻⁶)	2.6 10 ⁻⁶ (1.4 10 ⁻⁶)
a_C^W/Λ^2	[-0.052, 0.037]	2.0 10 ⁻⁵ (9.6 10 ⁻⁶)	9.4 10 ⁻⁶ (5.2 10 ⁻⁶)
a_0^Z/Λ^2	[-0.007, 0.023]	1.4 10 ⁻⁵ (5.5 10 ⁻⁶)	6.4 10 ⁻⁶ (2.5 10 ⁻⁶)
a_C^Z/Λ^2	[-0.029, 0.029]	5.2 10 ⁻⁵ (2.0 10 ⁻⁵)	2.4 10 ⁻⁵ (9.2 10 ⁻⁶)

Table 2.1: Reach on anomalous couplings obtained in γ induced processes after tagging the protons in the final state in the ATLAS Forward Physics detectors compared to the present OPAL limits. The 5 σ discovery and 95% C.L. limits are given for a luminosity of 30 and 200 fb⁻¹

and even applying a large uncertainty factor on this background would not change the results. In this study, the acceptance of the 420 and 220 m detectors ($0.0015 < \xi < 0.15$) was used and a cut on $W > 800$ GeV was applied. We cross checked that the reach remains similar using 220 m detector only. This is due to the fact that these events are produced at high mass ($W > 800$ GeV) and most anomalous coupling events are detected in 220 m detectors only. The averaged acceptance in the ee , $\mu\mu$, and mixed channels is 7.8% which is in agreement with the inclusive WW results from the ATLAS collaboration.

The sensitivities obtained using AFP and 30 fb⁻¹ of data are about 10000 times better than the best limits established at LEP2 [13] and about 100 times better than using the central detector only in analysis studying radiation zero in $pp \rightarrow l^\pm \nu \gamma \gamma$ events ($l = e$ or μ) [14]. These sensitivities reach the values expected for Higgsless or extra-dimension kinds of models (a few 10⁻⁶). This study show the great potential of AFP to probe these new kinds of models with a precision which does not seem to be reachable by other means at the LHC. The studies of the sensitivity using AFP were performed again with a reduced acceptance in mass corresponding to 220 m only. Since large mass $W > 800$ GeV was already required in the previous analysis, the sensitivity is not much degraded. Depending on the anomalous parameter, the limits are between 1000-10000 better than the best limits from LEP2, clearly showing the large and unique potential of such studies at the LHC even using 220 m detectors only. This will allow to probe with an with high precision the electroweak symmetry breaking in the SM model. As mentioned already, such values of the couplings to which AFP is sensitive appear in some Higgsless or extra-dimension models, even though the exact link between the studied effective Lagrangian and the particular theories is difficult to make due to not easy theoretical calculation. New signal not compatible with the SM predictions would surely stimulate the interest in these theories [15].

2.4 Diffraction and QCD

Proton tagging at ATLAS will allow the study of hard diffraction, expanding and extending the investigations carried out at CERN by UA8 [16], more recently at HERA by H1 and ZEUS and at Fermilab by CDF and D0 (see e.g. [17, 18, 20, 19] and references therein). At low luminosity, single diffractive (SD) meson, di-jet and vector boson production, $pp \rightarrow pX$, can be observed. At higher luminosities, double pomeron exchange, $pp \rightarrow pXp$, can be used for similar studies, the

372 lower event rate being compensated by additional rejection against the combinatorial overlap
373 backgrounds (from requiring one extra proton tag and vertex matching using the fast-timing
374 detectors). Note that DPE is distinct from CEP, as the central system contains remnants from
375 the diffractive exchange in addition to the hard subprocess. These processes are sensitive to
376 the low- x structure of the proton and the diffractive parton distribution functions (dPDFs).
377 Inclusive jet and heavy quark production are mainly sensitive to the gluon component of the
378 dPDFs, while vector boson production is sensitive to quarks. The kinematic region covered
379 expands that explored at HERA and Tevatron, with values of β (the fractional momentum of
380 the struck parton in the diffractive exchange) as low as 10^{-4} and of Q^2 up to tens of thousands
381 of GeV^2 .

382 SD and DPE can also be used to determine the soft-survival probability, which is interesting
383 in its own right because of its relationship with multiple scattering effects and hence the structure
384 of the underlying event in hard collisions. Azimuthal correlations between the two forward
385 protons produced in DPE allow the soft-survival factor to be probed as a function of the proton
386 kinematics. More detailed studies, including diffractive di-jet production, W and Z production
387 and B meson production can be found in [20].

388 Besides the diffractive analyses involving a hard scatter mentioned above, forward detectors
389 will allow the analysis of the particle flow in soft diffractive events for example by measuring
390 the charged particle distributions in events with one proton tag. Such studies will be performed
391 at the very beginning of the physics program since the issue of additional pile-up events is less
392 problematic than in hard diffraction. The modeling of the soft diffractive component is quite
393 different between various Monte Carlo generators (such as PYTHIA6/8, PHOJET). The validity
394 of the triple-pomeron approach in Regge theory can be tested by measuring the soft diffractive
395 cross section as a function of the diffractive mass $M^2 = s\xi$ [21, 22].

396 2.5 Summary

397 Forward proton tagging at ATLAS has the potential to significantly increase the physics reach
398 of the experiment. The key experimental channels only accessible using the very precise forward
399 detectors are central double pomeron exchange and photon-photon physics. Two proton tags
400 coupled with time-of-flight information from the forward detectors will allow inclusive (parton-
401 parton) backgrounds to be adequately rejected, even for the fully hadronic final states, at high
402 luminosity running.

403 In the first phase of installation before the inclusion of 420 m detectors, not all the physics
404 measurements are possible. However, the available acceptance however allows us to perform a
405 number of interesting analyses even without the increased acceptance that 420 m taggers would
406 bring. The 220 m detectors will enable us to exploit the range of forward physics while preparing
407 for the possibility of a 420 m upgrade in a second phase. The program that we anticipate to be
408 available is summarised in Table 2.2.

409 It is possible to measure single diffraction in which one proton remains intact and is tagged
410 by a forward detector. The majority of these searches have a large cross section and could be
411 investigated during special runs. Further work is required to determine up to which luminosity
412 the measurements can be made. Single diffraction provides additional information on the dPDFs
413 and soft-survival by measuring di-jet and vector boson production.

414 Photon-photon physics allows absolute luminosity determination and *in situ* forward detector
415 calibration through the well-known QED process, $\gamma\gamma \rightarrow \mu^+\mu^-$, though the statistics will be
416 limited with 220 m detectors. Vector boson production in this channel allows competitive
417 sensitivities to be set on the anomalous quartic gauge couplings even in the 220 m running

Diffraction and QCD	
Soft diffraction	YES
Luminosity monitoring	YES
Survival probability	YES
PDF in Pomeron measurements	YES
Single diffractive W , Z , jets	YES
Double pomeron exchange jets	YES
Double pomeron exchange WW , ZZ	YES
Photon-Photon Physics	
Alignment (lepton pairs)	YES
Luminosity measurement	NO
Anomalous couplings of vector bosons	YES
Threshold scan WW	NO
Light SUSY	NO
$\gamma g \rightarrow tt$	NO
$\gamma g \rightarrow t$	NO
Associated WH production	NO
Central Exclusive Production	
BSM Higgs quantum number measurement	NO
Di-jets, Study of Sudakov suppression	NO

Table 2.2: Summary of measurements which can be performed with a reduced forward detector acceptance using only 220 m detectors with respect to the complete 220+420 m setup described in Appendix III.

418 configuration, and allows to extend the ATLAS sensitivities to Higgsless and extra-dimension
419 models with an unprecedented precision.

420 In the second stage of the forward physics program with 420 m detectors, the study of the
421 Higgs bosons in the supersymmetric extensions, MSSM and NMSSM is made possible. For any
422 resonance production in CEP, the quantum numbers of the produced particle are restricted to
423 $J^{PC} = 0^{++}$ to a very good approximation. In addition, forward detectors provide an excellent
424 mass measurement regardless of the decay products of the produced particle.

425 In two-photon production, the high yields of $\gamma\gamma \rightarrow \mu^+\mu^-$ process allows the absolute luminos-
426 ity determination and, in addition, *in situ* forward detector calibration through the well-known
427 QED process. Charged SUSY pair production could be measured for light SUSY particles and
428 the information provided by the forward detectors will improve the mass measurement of the
429 new particles. Photoproduction allows the study of single top production, allowing limits to be
430 set on the anomalous γut and γct couplings.

431 Double pomeron exchange allows the studies of diffractive parton distribution functions and
432 the soft-survival factor, which is responsible for the factorization breaking observed in hard
433 diffractive interactions between ep and $p\bar{p}$ colliders. Event rates for vector meson, di-jet and
434 vector boson production are very large in this case when lower fractional momentum losses of
435 the protons are detectable.

Chapter 3

Hamburg Beampipe

3.1 Introduction

Near beam detectors are typically housed in Roman Pots, such as those used by ALFA, which allow the detector to remain outside of the machine vacuum and be remotely located close to the beam after injection. Since AFP will host both a Si and timing detector, however, AFP plans to use a moving-beampipe technique developed at DESY [23]. The linear space that will be needed for each Hamburg pipe will be 145/175cm depending on the bellows design, the longer detector to be hosted being the GASTOF timing detector. This so-called “Hamburg beampipe” is a large diameter section of beampipe that has rectangular thin wall “pockets” to house the Silicon pixel detectors and precision Time of Flight detectors used to track and time scattered beam protons at ± 220 m. This specialized section of beampipe is connected at either end to the standard LHC beampipe by bellows that can withstand a transverse displacement of about 25 mm.

The Hamburg pipe mechanics has several advantages over typical Roman Pot technology. It allows a much simpler access to detectors and provides direct mechanical and optical control of the actual detector positions. Unlike the Roman pot system, which has to compensate for the force arising from pressure differences as the detectors are inserted into the vacuum, the Hamburg pipe maintains a fixed vacuum volume. This results in a greatly reduced mechanical stress allowing a very simple and robust design. In effect, the Hamburg pipe is an instrumented collimator. Consequently, the LHC collimator control system and motor design can be adopted with zero modification. The idea is to use the same kind of motors which is used by the standard LHC collimators, which should not raise any safety issue. In this chapter, the main features of the moveable beam pipe design are presented. More detailed information can be found in the FP420 design report [24].

The overall layout of the tracking and timing detectors within the two Hamburg Pipes, placed on each side of the ATLAS IP, is shown in Figure 3.1. The QUARTIC ToF detectors are placed downstream of the Silicon detectors to minimize the effects of multiple scattering on the tracking. Figure 3.2 shows the layout of the movable beam pipe including two detector stations and the support table. The 220 m support table is much simpler than the 420 m table in Ref. [24], since it is already located in a warm region (no cryo bypass needed) and does not need to support any radiation shielding.

3.2 Hamburg pipe design requirements

The Hamburg pipe has the following requirements:

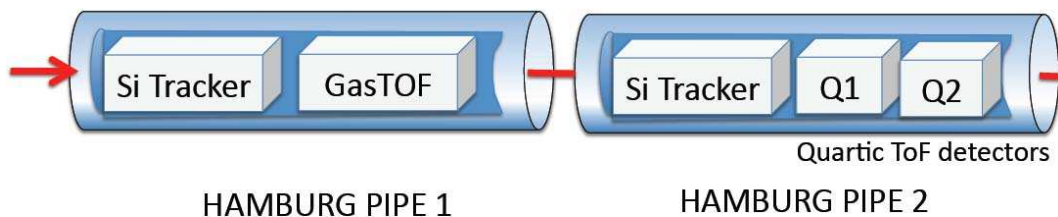


Figure 3.1: Functional layout of the tracking and timing detectors within the two Hamburg Pipes on each side of the ATLAS IP. The red arrow denotes the direction of the beam..

- 470 • It must allow for a precise and repeatable movement of the detectors by ~ 25 mm, so that
 471 the detectors housed in pockets in the Hamburg pipe can be kept a safe distance from
 472 the beam during filling and tuning. We intend to go down to 15σ from the beam, which
 473 means slightly less than 1.5 mm. Taking into account the thin window and the dead zone
 474 for the Si, we can go as close to the beam as 2 mm. In exceptional clean beam conditions,
 475 it might be possible to go closer than 15σ .
- 476 • It must have minimal deformation and a thin vacuum window both perpendicular and
 477 parallel to the beam allowing the detector to be placed within a few mm of the beam.
- 478 • The pockets must be optimized to house the different detectors and allow for secondary
 479 vacuum and cooling.
- 480 • The RF impact of the pockets should be minimal.
- 481 • Wherever possible standard LHC components should be used to ensure compatibility with
 482 the machine and collimator controls.

483 3.3 Movable pipe design

484 Figure 3.3 shows one of the two detector stations equipped with timing and silicon detectors,
 485 two LVDTs (Linear Variable Differential Transformer) in order to measure the position of the
 486 detector and two moving and one fixed beam position monitor (BPM). The BPMs will be used to
 487 measure the beam position with respect to our detector whereas the LVDTs are used to measure
 488 the detector position with respect to the HOME position. The support table and motion system
 489 are shown in Fig. 3.5.

490 For the prototype design, each of the four detector stations (two each at ± 220 m) is composed
 491 of a beam-pipe with inner diameter of 68.9 mm, wall thickness of 3.6 mm and two pockets, with
 492 default lengths 200 mm for the silicon detectors and 360 mm for the fast timing detectors.
 493 Rectangular thin-walled pockets are built into the pipe to house the different detectors that
 494 must be positioned close to the beam. The displacement between data taking position and the
 495 retracted or parked position is 25 mm, which is well within the collimator acceptance. The 25
 496 mm movement will put us in the shadow of the collimator. The ends of the moving beam-pipes
 497 are connected to the fixed beam-pipes by a set of two bellows. The stress level on the bellows at
 498 25 mm corresponds to a force required to move the below of only 9 kg. This test was performed

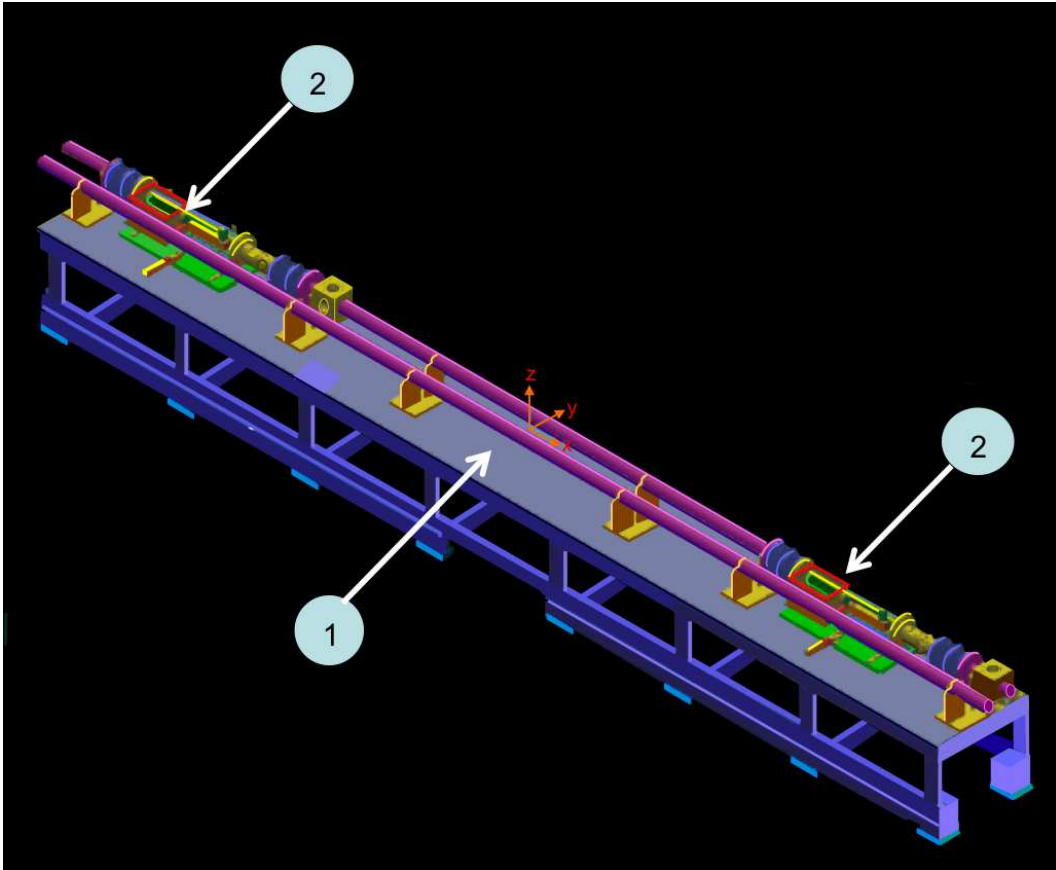


Figure 3.2: Schematic view of the: (1) detector arm with support table; and, (2) detector sections.

499 by Ray Veness with an early design of the bellows and we plan to redo these tests with final
500 bellow designs.

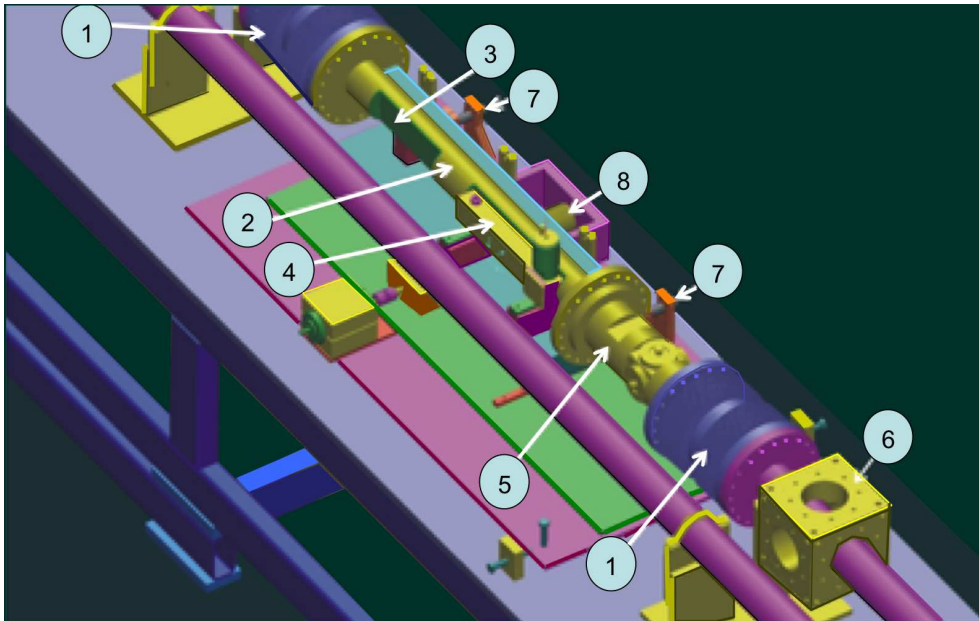


Figure 3.3: Top view of one detector section: bellows (1), moving pipe (2), Si-detector pocket (3), timing detector (4), moving BPM (5), fixed BPM (6), LVDT position measurement system (7), emergency spring system (8).

501 3.3.1 Pocket design

502 A key factor in the pocket design is the desire to maximise detector acceptance, which is achieved
503 by minimizing the distance of the detector edge from the LHC beam. This in turn requires that
504 the thickness of the detector pocket wall should be minimised to limit the dead area. Care must
505 be taken to avoid significant window deformation which could also limit the detector-beam
506 distance.

507 A rectangular shaped detector pocket is the simplest to construct, and minimises the thin
508 window material perpendicular to the beam which can cause multiple scattering and degrade
509 angular resolution of the proton track. Only stainless steel beam tubes are suitable. They
510 will be copper coated for RF-shielding and Non-Evaporative Getter (NEG) coated for vacuum
511 pumping.

512 As a starting point, we chose a 400 micron thick window as a conservative estimate. However,
513 based on the ALFA experience, where a 200 μm window of size 3×5 cm was utilized, we are
514 studying thinner window configurations. Our window size is much longer 2×45 cms. But the
515 shortest dimension is the most critical. We expect that a window thickness of 200-300 microns
516 would be possible and a FEA is in progress.

517 An initial “Multi Pass Adaptive Method” Finite Element Analysis (FEA) study for a 200 μm
518 stainless steel window has been performed. The maximum bowing observed in the $2 \text{ cm} \times 45$
519 cm window was 0.56 mm with the pocket open to the atmosphere. Of course with a secondary
520 vacuum in the pocket region this bowing would be negligible. According to this initial analysis
521 the use of a 200 μm window does not appear to present a problem, although this conclusion my

522 change as our FEA studies and prototype testing program matures. An example of the output
523 of the FEA analysis is shown in Figure 3.4. Studies with different window thicknesses, window
524 sizes and beam-side window to end-window transitions are currently underway.

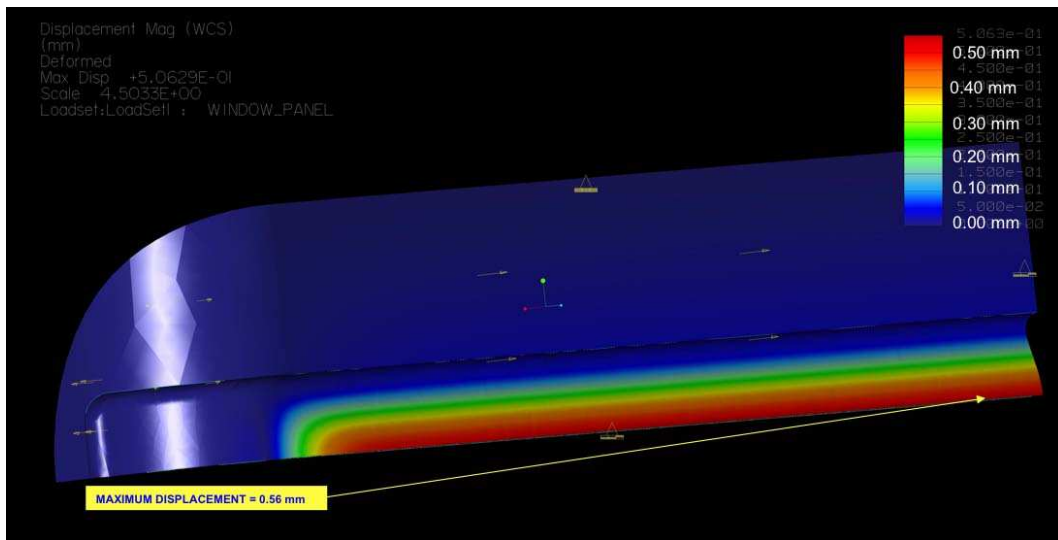


Figure 3.4: FEA analysis output of the window deflection for a 200 micron thick stainless steel window of size 2 cm × 45 cm window. The maximum deflection of the window with a pressure differential of one atmosphere is 0.56 mm.

525 A prototype of the detector box has been already performed by the Louvain group in CMS,
526 and tested in beam tests. However, the box was empty and the design of the Si and timing
527 detectors inside the box (and alignment) is in progress in Saclay.

528 3.3.2 Motorization and detector system positioning

529 In routine operation, detector stations will have two primary positions (1) the parked position
530 during beam injection, acceleration and tuning, and (2) the operational position close to the
531 beam for data taking. The positioning must be accurate and reproducible. Two options have
532 been considered: equipping both ends of the detector section with motor drives which move
533 synchronously but allowing for axial corrections with respect to the beam axis, or a single drive
534 at the centre, complemented with a local manual axial alignment system. A two motor solution in
535 principle allows perfect positioning of the detector station, both laterally and axially. However,
536 it adds complexity to the control system, reduces reliability, and increases cost. Positioning
537 accuracy and reproducibility are also reduced because extremely high precision guiding systems
538 can no longer be used, due to the necessary additional angular degree of freedom. Therefore, a
539 single motor drive system is favoured, accompanied by two precise LVDTs. The aim of position
540 reproducibility is of the order of a few microns. The final decision will come while doing the
541 tests of the movable beam pipe system. The table will be adjusted in the vertical direction for
542 once and only the horizontal motion will be performed in normal stores and data taking.

543 3.3.3 Beam position monitors and alignment

544 The reconstruction of the proton momentum depends in principle only on the optics of the two
545 beamlines and the position of the silicon sensors relative to the beam. In practice, however, the

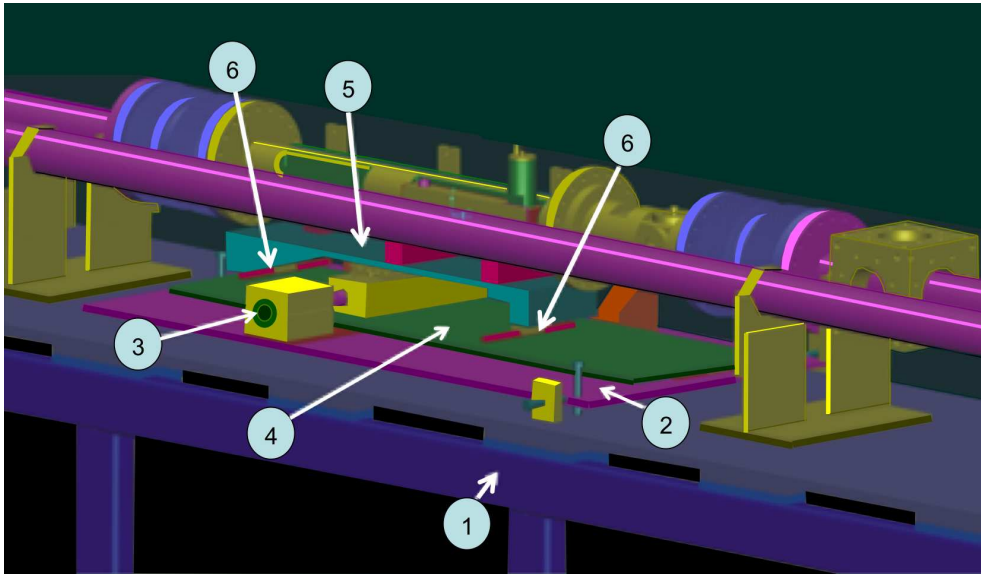


Figure 3.5: Support table (1), drive support table with alignment system (2), drive motor (3), intermediate table for emergency withdrawal (4), moving support table (5), and linear guides (6).

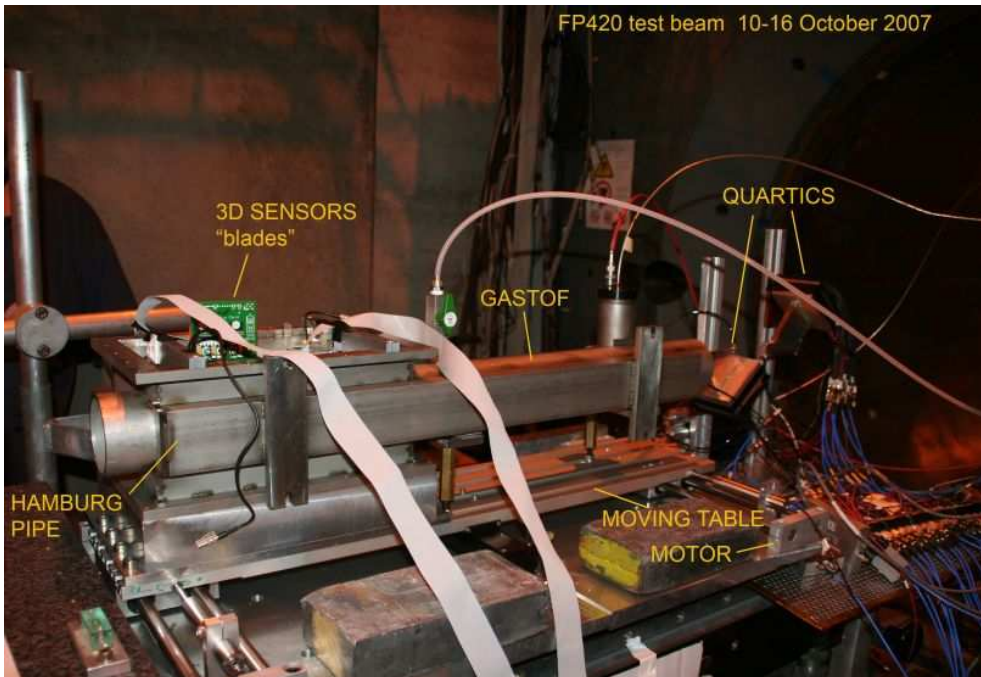


Figure 3.6: Photograph of the prototype beam-pipe section used in the October 2007 CERN test beam.

546 magnet currents will vary from fill to fill, and the fields in the magnets will vary accordingly.
 547 The AFP collaboration considered two independent alignment strategies. One is to use a physics
 548 process detectable in the ATLAS central detector which produces proton tracks in the detectors
 549 of known energy. This strategy is independent of the precise knowledge of the LHC optics
 550 between the IP and the detectors and is described in the physics chapter. It will also be
 551 necessary to have a real-time alignment system to fix the position of the detectors relative to
 552 the beam and provide complementary information to the off-line calibration using tracks.

553 An independent real-time alignment system is also essential for safety purposes while moving
 554 the detectors into their working positions. Two options, both based on Beam Position Monitors
 555 (BPMs), are being considered: a ‘local’ system consisting of a large-aperture BPM mounted
 556 directly on the moving beampipe and related to the position of the silicon detectors by knowledge
 557 of the mechanical structure of the assembly, and an ‘overall’ system consisting of BPMs mounted
 558 on the (fixed) LHC beampipe at the two ends of the system, with their positions and the moving
 559 silicon detectors’ positions referenced to an alignment wire using a Wire Positioning Sensor
 560 (WPS) system. Figure 3.7 shows schematically the proposed ‘overall’ alignment subsystem.
 561 To simplify the illustration only one moving beam pipe section is shown. The larger aperture
 562 BPMs for the ‘local’ alignment system are not shown (one would be mounted on each moving
 563 beam pipe section). It is likely that both the local and overall BPM alignment schemes will be
 564 implemented.

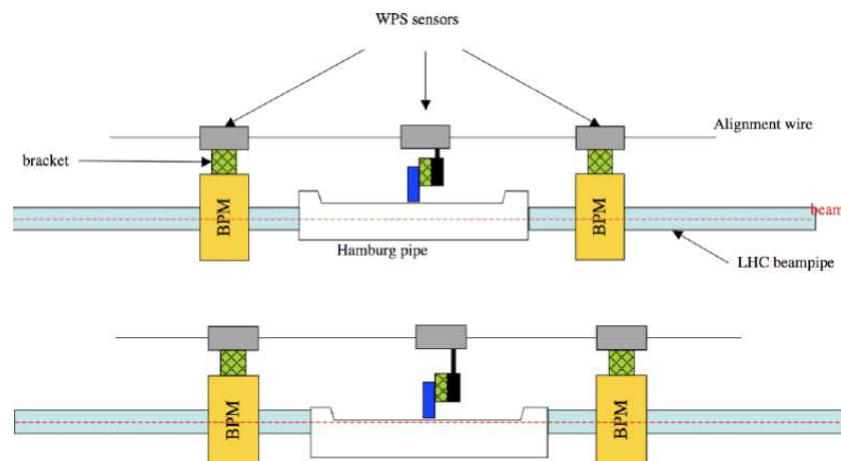


Figure 3.7: The proposed overall alignment system, shown with detectors in garage position (top picture) and in operating position (bottom picture).

565 Sources of uncertainty in such a system include the intrinsic resolution of the WPS system,
 566 the intrinsic resolution (and calibration) of the BPMs, and the mechanical tolerances between
 567 the components. The mechanical uncertainties may be affected by temperature fluctuations and
 568 vibrations in the LHC tunnel, and the movement of the detectors relative to the beam must be
 569 taken into account. The individual components of the system, with comments on their expected
 570 accuracy, are described in the following subsections.

571 **Beam position monitors**

572 A direct measurement of the beam position at the detector positions can be obtained with beam
 573 position monitors (BPMs). Although there are several pickup techniques available, an obvious
 574 choice would be the type used in large numbers in the LHC accelerator itself. The precision and

575 accuracy of these electrostatic button pickups can be optimized through the choice of electrode
 576 geometry and readout electronics. While BPMs can be made with precision geometry, an impor-
 577 tant issue is balancing the gain of the right and left (or up and down) electronics; one can have a
 578 time-duplexed system such that the signals from opposing electrodes are sent through the same
 579 path on a time-shared basis, thus cancelling any gain differences. Multiplexing of the readout
 580 chain will avoid systematic errors due to different electrical parameters when using separate
 581 channels and detuning through time and temperature drift. Preliminary tests with electrostatic
 582 BPMs designed for the CLIC injection line have shown promising behavior on the test bench,
 583 even when read out with general purpose test equipment. More details can be found in [24].

584 Although the requirements are not as demanding for the LHC as for ATLAS FP, it is our ex-
 585 pectation that the necessary level of precision, resolution and acquisition speed can be obtained.
 586 It should be emphasized that the precision will depend to a large extent on the mechanical
 587 tolerances which can be achieved. Several strategies and optimizations have been proposed to
 588 reach precision and resolution of a few microns, and to achieve bunch-by-bunch measurement.
 589 This is being developed by the LHC machine group.

590 Multi-turn integration will improve the resolution at least by a factor 10. Bunch/bunch mea-
 591 surements will still be possible since the bunches in LHC can be tagged, allowing measurements
 592 of each bunch to be integrated over a number of turns. The variation of one specific bunch
 593 between turns is expected to be small.

594 Shortly before the installation of each complete ATLAS FP section (with trackers and BPMs)
 595 a test-bench survey using a pulsed wire to simulate the LHC beam will provide an initial cali-
 596 bration of the BPMs. Further in-situ calibration can be done by moving each BPM in turn and
 597 comparing its measured beam position with that expected from the measurements in the other
 598 BPMs in the system; the potential for success of such an online BPM calibration scheme has
 599 been demonstrated with cavity-style BPMs intended for use in linear colliders [26, 27]. Such cal-
 600 ibration may even be possible at the beginning and end of data-taking runs when the BPMs are
 601 being moved between garage and operating positions, removing a need for dedicated calibration
 602 runs.

603 We expect a resolution of 10 to 15 microns, which required some developments of the readout
 604 electronics for the BPMs. This is in progress in the LHC beam division and this is definitely an
 605 area where help is needed from the beam division.

606 Wire positioning sensors

607 Wire Positioning Sensor (WPS) systems use a capacitive measurement technique to measure
 608 the sensors' positions, along two perpendicular axes, relative to a carbon-fibre alignment wire.
 609 Such systems have been shown to have sub-micron resolution capability in accelerator alignment
 610 applications and will be used in LHC alignment. The principle of operation is shown in Fig. 3.8.
 611 Photographs of a sensor (with cover removed) and of two end-to-end sensors are shown in
 612 Fig. 3.9.

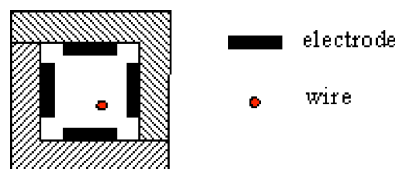


Figure 3.8: A cross-sectional schematic of a WPS sensor and alignment wire.

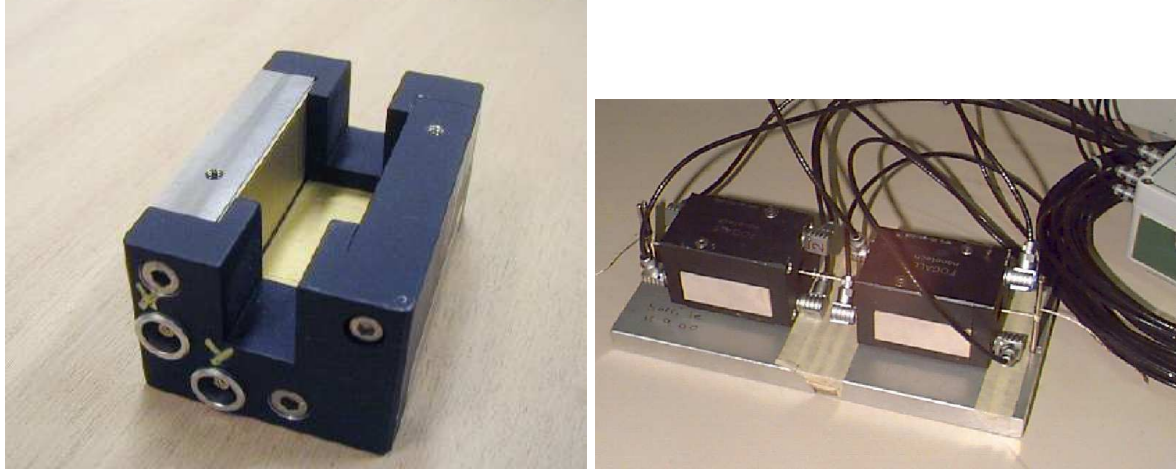


Figure 3.9: A WPS sensor with lid removed (left), showing the electrodes. The aperture is 1cm square. Also shown are two WPS sensors on the test bench (right).

613 3.4 System performance and operation

614 The baseline prototype of the moving beampipe was prepared for use in test beam at CERN in
 615 October 2007. Figure 3.6 shows the one-meter long beam-pipe equipped with two pockets, one
 616 of 200 mm length for the pixel detector and the other of 360 mm length for the gas Čerenkov
 617 timing detector. The vacuum window thickness was 0.4 mm. As we mentioned already, this
 618 width is conservative and we will try to get a thinner window. A detector box for the 3D
 619 detectors was mounted in the first pocket. The moving pipe was fixed on a moving table, driven
 620 by a MAXON motor and guided by two high precision linear guides. The relative position of
 621 the moving pipe was measured with two SOLARTRON LVDT displacement transducers, which
 622 have $0.3 \mu\text{m}$ resolution and 0.2% linearity. The magnitude of the deformation of a 600 mm long
 623 pocket, measured by FP420 [24], was less than $100 \mu\text{m}$. The shorter pockets planned for the
 624 final design is expected to yield significantly less deformation.

625 The AFP detectors incorporated into the beam pipe will operate at all times in the shadow of
 626 the LHC collimators in order to guarantee low background rates and to avoid detector damage
 627 from unwanted beam losses. Therefore, the high-level Hamburg pipe control system will be
 628 integrated into the collimator control system. The interface between low- and high-level controls
 629 will be implemented using the CERN standard Front End Standard Architecture (FESA) [25].

630 The LHC Control Room will position the detectors close to the beam after stable collisions
 631 are established. The precision movement system will be able to operate at moderate and very
 632 low speed for positioning the detectors near the beam. During insertion and while the detectors
 633 are in place, rates in the timing detectors will be monitored, as well as current in the silicon.
 634 The step motor and LVDT's will provide redundant read-back of the position of the detectors
 635 and fixed and moveable BPM's will provide information on the position of the detectors with
 636 respect to the beam. In addition, we plan to design a fast extraction system in case of issues for
 637 instance a change of beam position or high beam losses.

638 3.5 Machine induced backgrounds and RF effects

639 The safe distance of approach of the detectors to the beam depends on the beam conditions,
 640 machine-induced backgrounds, collimator positions and the RF impact of the detector on the

641 LHC beams. Detailed studies have been performed and the machine-induced background from
642 near beam-gas and betatron cleaning collimation was found to be small. A reevaluation of this
643 background is planned based on early LHC data. Extensive simulation and laboratory studies
644 were carried out to test the impact of the Hamburg pipe on the LHC impedance budget [24].
645 The designs described above were found to have a negligible impact on the LHC impedance
646 budget at 420 m, and similar results are expected for the 220 m region.

647 **3.6 Ongoing research and development**

648 After the Technical Proposal has been accepted by the ATLAS Collaboration we can begin the
649 final design phase of the Hamburg pipe. At this point we will repeat impedance studies using
650 the final design and the 220 m optics. We envisage that a joint ATLAS/CMS safety review
651 committee will be instituted together with LHC Vacuum group to assess all safety issues related
652 to the project. This safety review will validate the details of the final design of the Hamburg
653 Pipe mechanics.

654 **3.7 Conclusions**

655 The Hamburg moving pipe concept provides the optimal solution for the 220 m detector systems
656 at ATLAS. It ensures a simple and robust design and good access to the detectors. Moreover,
657 it is compatible with the limited space available at 220 m needed to host both the silicon
658 tracking detectors and the timing detectors. Its reliability is linked to the inherent absence of
659 compensation forces and the direct control of the actual position of the moving detectors.

660 The detectors can easily be incorporated into the pockets, which are simply rectangular
661 indentations in the moving pipes. The prototype detector pockets show the desired flatness of
662 the thin windows, and the first motorised moving section, with prototype detectors inserted,
663 has been tested at the CERN test beam. This was a first step in the design of the full system,
664 including assembling, positioning and alignment aspects.

665 It should be noted that the Hamburg pipe design, development, and prototyping was per-
666 formed with the direct knowledge of the LHC cryostat group. In particular, the Technical
667 Integration Meetings (TIM), held regularly at CERN and chaired by K. Potter, provided an effi-
668 cient and crucial framework for discussions and information exchanges. Similar meetings would
669 re-commence after the Technical Proposal is approved by ATLAS.

Chapter 4

The Silicon Tracking Detector

4.1 Introduction

The silicon tracker system is the heart of the ATLAS Forward Proton detector system. Its purpose is to measure points along the trajectory of beam protons that are deflected at small angles as a result of collisions. The tracker when combined with the LHC dipole and quadrupole magnets, forms a powerful momentum spectrometer. Silicon tracker stations will be installed in Hamburg beam pipes at ± 216 and ± 224 m from the ATLAS IP as discussed in the previous chapter. To reconstruct the mass of the central system produced in ATLAS, it is necessary to measure both the distance from the beam and the angle of the proton tracks relative to the beam with high precision, so beam position monitors (BPM's) are integrated into the Hamburg pipe system.

The smallest distance at which sensors can approach the beam to detect the scattered protons determines the minimum fractional momentum loss (ξ) of detectable protons. The 220 m stations are designed to track protons with fractional momentum losses in the range $0.02 < \xi < 0.2$. For events in which both protons are tagged this corresponds to a range of central masses from a few hundred GeV to beyond one TeV. With a typical LHC beam size at 220 m of $\sigma_{beam} \approx 100 \mu\text{m}$, the window surface of the Hamburg pipe can theoretically safely approach the beam to $15 \times \sigma_{beam} \approx 1.5$ mm. The window itself adds another 0.2 to 0.4 mm to the minimum possible distance of the detectors from the beam (depending on the chosen solution), and any dead region of the sensors should clearly be kept to a minimum. Placing the sensors a few millimeters from the beam imposes high demands on the radiation hardness, the radio frequency pick-up in the detector and the local front-end electronics.

4.2 Tracking system requirements

The key requirements for the silicon tracking system at 220 m are listed below:

- Spatial resolution of ~ 10 (30) μm per detector station in x (y)
- Angular resolution for a pair of detectors of about 1 μrad
- High efficiency over an area of 20 mm \times 20 mm.
- Minimal dead space at the edge of the sensors
- Sufficient radiation hardness

- Capable of robust and reliable operation at high LHC luminosity

The required position and angular resolution is obtained from the tracking studies and is consistent with a mass resolution of ~ 5 GeV. Figure 4.1 shows that an area of about $20 \text{ mm} \times 20 \text{ mm}$ is needed to have full acceptance for scattered protons given that the detector is located 2 to 3 mm from the beam axis.

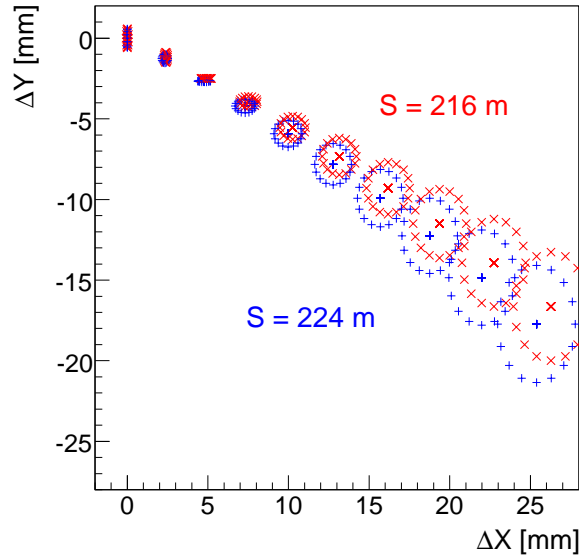


Figure 4.1: The displacement in x and y for scattered protons from the nominal beam axis which is placed at $(x, y) = (0, 0)$. Moving from left to right, different ellipses correspond to increasing values of ξ , the centers of ellipses correspond to $t = 0.0 \text{ GeV}^2$, while the ellipses correspond to $t = 0.5 \text{ GeV}^2$. The red symbols show the results for the station at 216 m, the blue symbols for the station at 224 m from the IP. The largest value of ξ is given by the LHC apertures in front of the stations.

4.3 Tracking system design

The basic building block of the AFP detection system is a module consisting of an assembly of a sensor array, on-sensor read-out chip(s), electrical services, data acquisition (DAQ) and detector control system (DCS). The module will be mounted on the mechanical support with embedded cooling and other necessary services. The module concept and its mechanical size are essentially determined by sensor granularity dictated by physics requirements and the read-out chips employed.

In general, we assume that we have 5 planes of Si detector staggered by half the size of a pixel. A general integration design of the Si detector inside the movable beam pipe pocket is in progress by the Saclay mechanical engineers.

4.3.1 The silicon sensor

The 2008 AFP Letter of Intent [1] had 3D sensors coupled to FE-I3 readout chips as the default silicon option due to the high radiation tolerance and small inactive regions. Since then the

718 Manchester group leading the 3D option has been forced to halt work on AFP due to funding
 719 issues. There have also been significant R&D programmes into 3D and planar sensors for the
 720 Insertable B layer (IBL) project [28], which has a similar time scale and requirements. Finally,
 721 the Prague group involved in the project brings significant planar silicon expertise and resources.
 722 We thus are exploring all the different sensor options and outline them below:

723 3D sensors

724 Different ways to manufacture 3D sensors have been investigated and the two proposed for
 725 IBL are called “double-sided” [29, 30] and single sided “full3D” with active edges [31, 32] (see
 726 Fig. 4.2). Prototypes for both methods have been manufactured and characterized with FE-I3
 727 readout electronics over the past three years with and without magnetic fields and for fluences
 728 expected for the IBL and beyond [33, 34]. The electrode configuration chosen for the IBL is
 729 called “2n-250”. This means that 2 n-type electrodes will be used to span the 250 μm readout
 730 pitch [35]. This configuration has an inter-electrode distance of $\approx 70 \mu\text{m}$ and, for the IBL
 731 radiation dose, is a good compromise between signal efficiency and capacitive noise increases
 732 with the number of electrodes per pixel.

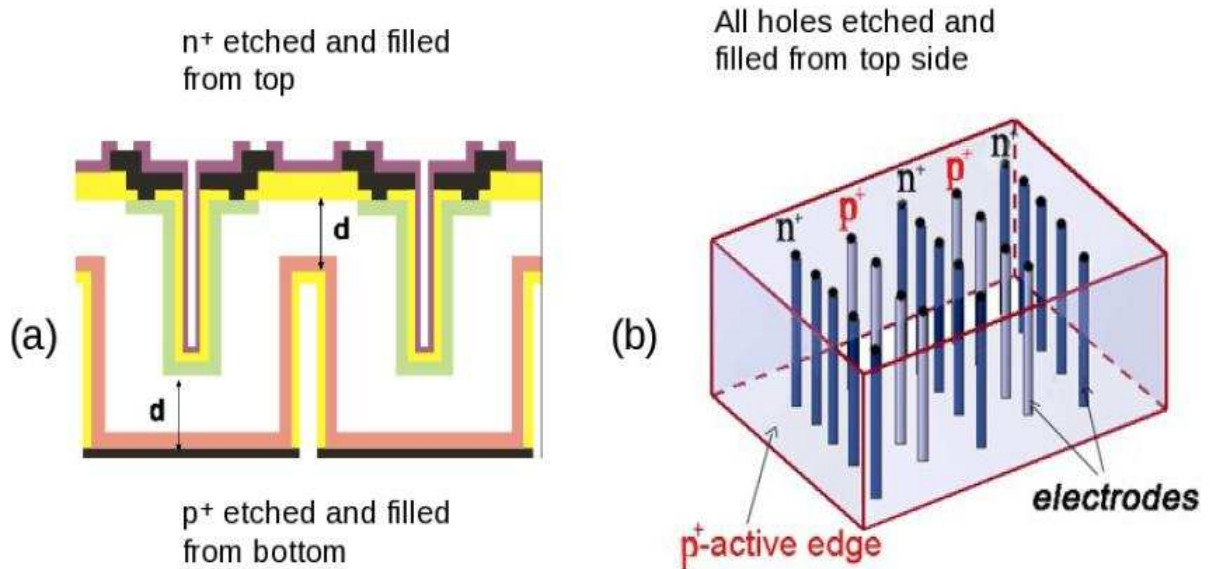


Figure 4.2: Double sided process (a) and full 3D with active edges (b). An un-etched distance d of order $20 \mu\text{m}$ is needed in (a) for mechanical integrity.

733 The signal efficiency for both methods measured with infrared photons and minimum ionizing
 734 particles is shown in Fig. 4.3 a), while the expected most probable signal for a substrate thickness
 735 of $230 \mu\text{m}$ is shown in Fig. 4.3 b). The results for the 3E-400 configuration shown in Fig. 4.3
 736 have been obtained using the FE-I3 chip. Due to the larger readout pitch of the FE-I3 chip the
 737 3E-400 configuration corresponds to the 2E-250 configuration chosen for the IBL.

738 Thanks to a relatively short charge collection in 3D sensors the required bias voltage is low
 739 even in over-depletion, both before and after irradiation, and consequently the power dissipation
 740 is reduced. The 3E-400 operating bias voltages are 80 V before irradiation, 120 V at 5×10^{15}
 741 n/cm^2 , and 180 V at $2 \times 10^{16} \text{n/cm}^2$ fluences. Besides the demonstrated high radiation tolerance,
 742 another strong feature of the 3D sensors is the active edge. A dead region close to the sensor

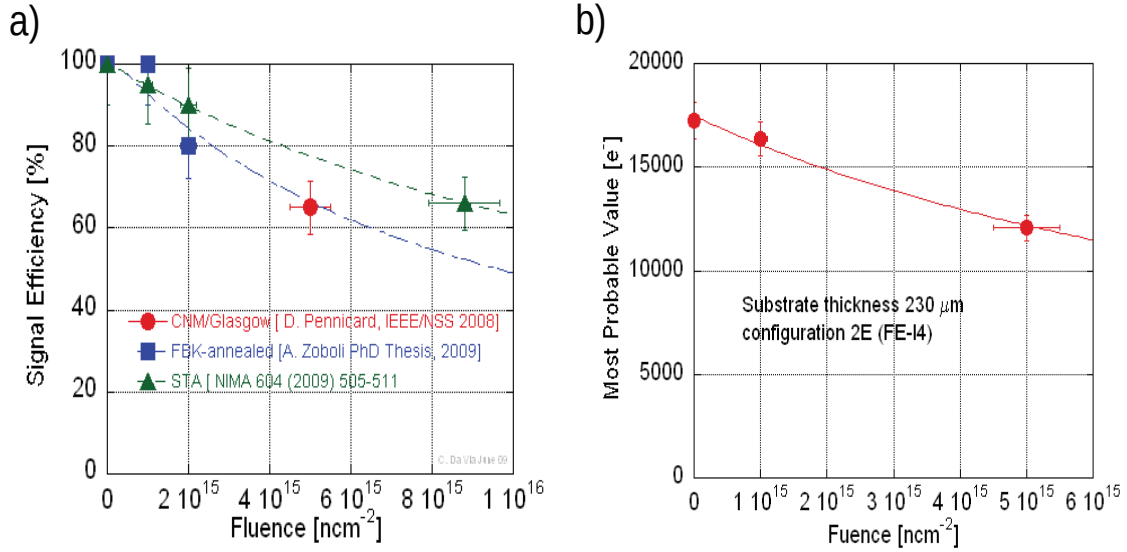


Figure 4.3: (a) Signal efficiency of double sided (CNM and FBK data points) and full3D (STA data points) 3E-400 electrode configurations. (b) Expected most probable signal for a 2E-250 electrode configuration, based on an averaged signal efficiency value from left. All sensors are 230 μm thick.

743 edge of size of a few microns is achieved by etching a trench around the sensor physical edge
 744 and by diffusing in dopants to make an electrode. The electrode center is not fully efficient and
 745 hence to increase the efficiency, the sensors need to be tilted. The efficiency with a 3200 e^-
 746 threshold is 96% at normal incidence and 99.9% at 15° from normal.
 747

748 Planar sensors

749 There are three types of planar sensors under consideration:

750 conservative n-in-n design

751

752 This option (Fig. 4.4 a)) is closest to the current design of the present ATLAS Pixel
 753 detector [36] which has been proven to function reliably. By reducing the number of
 754 guard rings from 16 (current ATLAS Pixel sensor) to 13, one can reduce the inactive
 755 region to 450 μm . It has been shown experimentally that this would typically exceed the
 756 full depletion voltage by more than 150 V. The pixel length in y has to be reduced to
 757 250 μm to match the y -size of the FE-I4 pixel. The n-in-n technology requires double-side
 758 processing. The main advantage of this option is the proven reliability.

759 slim-edge n-in-n design

760

761 The guard rings of the n-in-n design are placed on the p-side of the sensor, and therefore it
 762 is possible to shift them inwards, leading to a partial overlap with the outermost pixel row
 763 (see Fig. 4.4 b)). This has the advantage of reducing the inactive region to about 200 μm .
 764 This shift distorts the field close to the sensor edge, but from simulations [37] the effect is

765
766
767
768

expected to be negligible after irradiation because most of the charge is collected directly below the pixel implant due to partial depletion and trapping. The signal efficiency at the edge still needs to be studied in test beam. The overall sensor design is identical to the conservative design above.

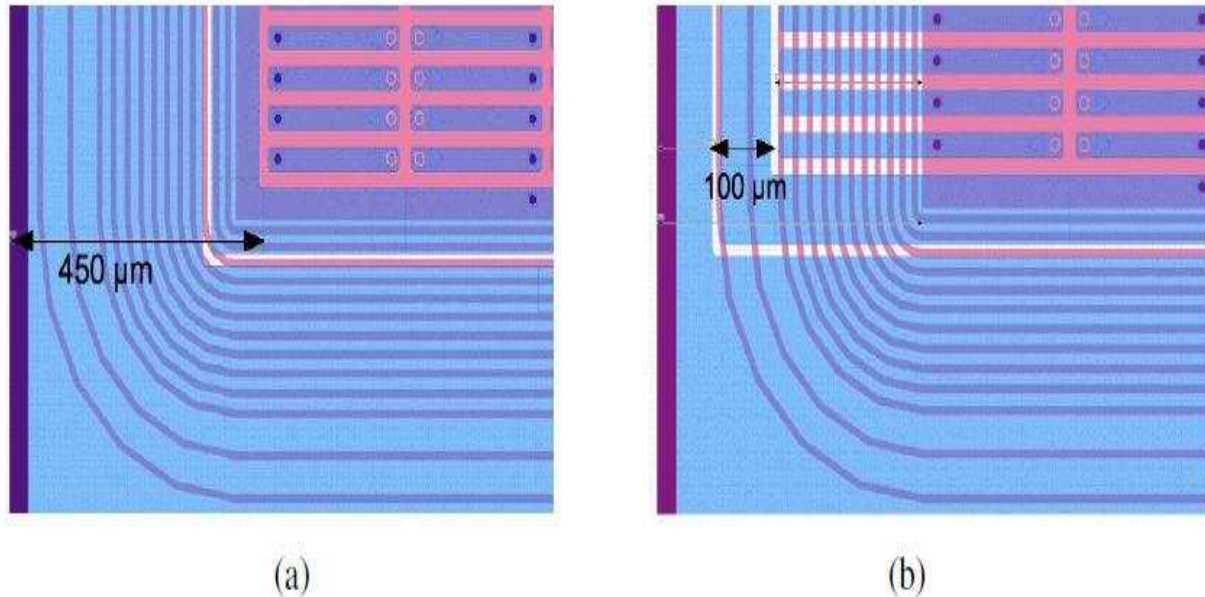


Figure 4.4: a) Conservative n-in-n sensor design. b) Slim-edge n-in-n sensor design.

769
770

thin n-in-p design

771
772
773
774
775
776
777
778
779
780
781
782
783
784

Sensors made on p-bulk are an interesting alternative to the more complex double-sided n-bulk sensors. The n-in-p technology is a choice for future strip upgrades replacing the hole-collecting p-in-n technology which performs poorly after high fluences. Therefore a significant R&D program is taking place within the ATLAS Upgrade environment in collaboration with leading semiconductor manufacturers. The n-in-p technology is being tested by all LHC experiments as well as by the RD50 Collaboration [38]. Performance before irradiation measured with the FE-I3 chip is equal to that of n-in-n sensors. While tests before irradiation showed a sufficient protection, the behaviour after the irradiation is still being investigated. n-in-p sensors offer, in addition to the large number of vendors capable of producing them, easier methods for thinning. A handle wafer method [39] has been developed to process n-in-p sensors down to thicknesses of below 100 μm. Good performance before and after irradiation has been achieved on FE-I3 compatible pixel sensors produced with this technique [40]. The inactive region can also be reduced to 450 μm with this technique [40] (see Fig. 4.5).

785

Sensor conclusions

786
787
788
789

The 3D sensors have full active edges, which is critical for maximizing the light mass acceptance for the 220/420 m AFP configuration, but is of less importance for this 220 m Stage 1 proposal. We note that the IBL decision is expected in June, and even though they are at the TDR stage and are attempting to install in 2013, the sensor choice has not been fully determined, so we

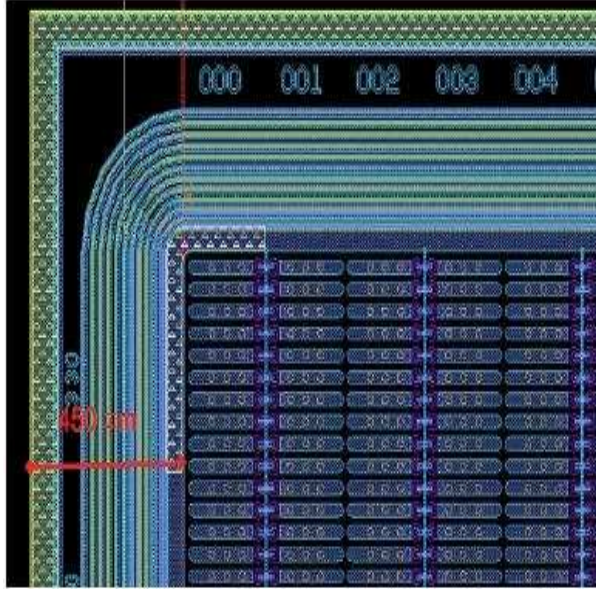


Figure 4.5: n-in-p Sensor design. The number of guard rings is chosen to meet the IBL limit of a $450 \mu\text{m}$ inactive edge.

790 are deferring this decision for now. There would be certain advantages to choosing the same
 791 technology as the IBL, although their requirements for active edges are more modest.

792 4.3.2 The readout chip

793 The present ATLAS pixel detector [43, 44, 45] is read out by the FE-I3 chip which contains
 794 2880 readout cells of $50 \mu\text{m} \times 400 \mu\text{m}$ size arranged in a 18×160 matrix. This system is
 795 currently functioning extremely well. For ATLAS tracking upgrades, starting with the IBL, the
 796 new front-end chip FE-I4 has been developed. The FE-I4 integrated circuit contains readout
 797 circuitry for 26 880 hybrid pixels arranged in 80 columns on $250 \mu\text{m}$ pitch by 336 rows on 50
 798 μm pitch, and covers an area of about $19 \text{ mm} \times 20 \text{ mm}$. It is designed in a 130 nm feature size
 799 bulk CMOS process. Sensors must be DC coupled to FE-I4 with negative charge collection.

800 The FE-I4 is very well suited to the AFP requirements: the granularity of cells provides a
 801 sufficient spatial resolution, the chip is radiation hard enough (up to $\sim 10^{15} \text{ n}_{eq} \text{ cm}^{-2}$), and the
 802 size of the chip is sufficiently large that one module can be served by just by one chip. This
 803 significantly simplifies the design of the AFP tracker, as no special tiling arrangement is needed.

804 Each pixel contains an independent, free running amplification stage with adjustable shaping,
 805 followed by a discriminator with independently adjustable threshold. The chip keeps track of the
 806 firing time of each discriminator as well as the time over threshold (TOT) with 4-bit resolution,
 807 in counts of an externally supplied clock, nominally 40 MHz. Information from all discriminator
 808 firings is kept in the chip for a latency interval, programmable up to 256 cycles of the external
 809 clock. Within this latency interval, the information can be retrieved by supplying a trigger.

810 Recent IBL discussions indicate that slightly modified FE-I4b chip will be ideally suited to
 811 the IBL and AFP. This has the major advantage in that AFP can take full advantage of the
 812 IBL development effort.

813 4.3.3 Location and layout

814 The stations are proposed to be placed at ± 216 m and ± 224 m from the ATLAS interaction
815 interaction point (IP). Two alcoves close to the stations (20 m cables) can house the readout
816 electronics crates that collect signal from the stations, send the trigger data to the Central
817 Trigger Processor (CTP) and receive the signal back from the CTP.

818 Each tracking station will consist of five layers of sensors each read out by a single FE-I4
819 chip. The mechanical design awaits a final sensor determination.

820 4.4 System performance and operation

821 To maximize the acceptance for low momentum-loss protons, the detectors should be active as
822 close to their physical edge as possible, this inactive area will range from a few microns for the
823 3D option to 0.5 mm for standard n-in-n and n-in-p options, due to the sequence of guard rings,
824 which control the potential distribution between the detectors sensitive area and the cut edge
825 to remove leakage current.

826 The dimensions of the individual cells in the FE-I4 chip are $50 \mu\text{m} \times 250 \mu\text{m}$ in the x and y
827 directions, respectively. Therefore to achieve the required position resolution in the x -direction
828 of $\sim 10 \mu\text{m}$, five layers with sensors are required (this gives $50/\sqrt{12}/\sqrt{5} \sim 7 \mu\text{m}$ in x and roughly
829 5 times worse in y). Offsetting planes alternately to the left and right by one half pixel, will
830 give a further reduction in resolution of at least 30%, which should easily meet the performance
831 goals. We note that, ideally, the resolution should in first approximation improve by a factor 5
832 and not $\sqrt{5}$ using 5 layers. However, this is true providing that one can really precisely make
833 the staggering (without any mechanical problem); $\sqrt{5}$ gives a conservative estimate which gives
834 a resolution of about $7\mu\text{m}$, and the optimistic resolution would be about $3 \mu\text{m}$ if staggering is
835 perfect. Obviously, we will do the best we can concerning staggering during mechanical assembly
836 and measure how successful we were, and the result will be somewhere between 3 and $7 \mu\text{m}$.

837 4.4.1 Electromagnetic environment

838 The detectors have to be shielded against the electromagnetic environment in the tunnel by a
839 Faraday cage. The readout chip should be robust with respect to beam-induced EM interactions,
840 power supply noise, ground fluctuations close to the chip inputs, etc. Therefore on-chip pedestal
841 subtraction or proper pulse processing (pulse shaping) prior to the threshold decision is required.
842 The FE-I4 technology (IBM CMOS8RF) itself should provide a good EMC immunity since 8
843 metal layers are used.

844 4.4.2 Radiation tolerance

845 The innermost layer of the ATLAS pixel detector is expected to be exposed to a fluence of
846 about 3.0×10^{14} 1 MeV neutrons per cm^2 ($n_{eq} \text{ cm}^{-2}$) per year at the full LHC luminosity of 10^{34}
847 $\text{cm}^{-2}\text{s}^{-1}$ corresponding roughly to a dose of 200 kGy per year. A fluence of $1.0 \times 10^{15} n_{eq} \text{ cm}^{-2}$
848 corresponds to roughly five years of running LHC at full luminosity. Results from test beams
849 with the silicon pixel sensors in the ATLAS [46] and CMS [47] detectors show that the detection
850 efficiency may be kept above 95% for fluences lower than $\sim 10^{15} n_{eq} \text{ cm}^{-2}$ if the irradiated
851 sensors are operated at sensor bias of 600 V (non-irradiated sensors are normally operated at
852 150 V) and the pixel electron threshold are lowered.

853 Results obtained by the RD50 Collaboration with miniature n-in-p strip detectors ($1 \times 1 \text{ cm}^2$)
854 using 40 MHz clock rate electronics have shown that, even after $2 \times 10^{16} n_{eq} \text{ cm}^{-2}$ planar sensors

855 can yield signal charge equal or even greater than before irradiation [41, 42]. The key feature to
 856 achieve large signal charge after heavy irradiation is high electric field, which for typical sensor
 857 thickness means operating at bias voltages well in excess of 1000 V. However, thin detectors
 858 can achieve high electric fields with lower voltages. Figure 4.6 shows the charge collection vs.
 859 dose in 300 μm sensors limited to 900 V. It can be seen that without relying on either on kV
 860 range bias or thin sensors, the MIP signal charge for planar sensors after $5.0 \times 10^{15} \text{ n}_{eq} \text{ cm}^{-2}$ is
 861 approximately 8000 electrons.

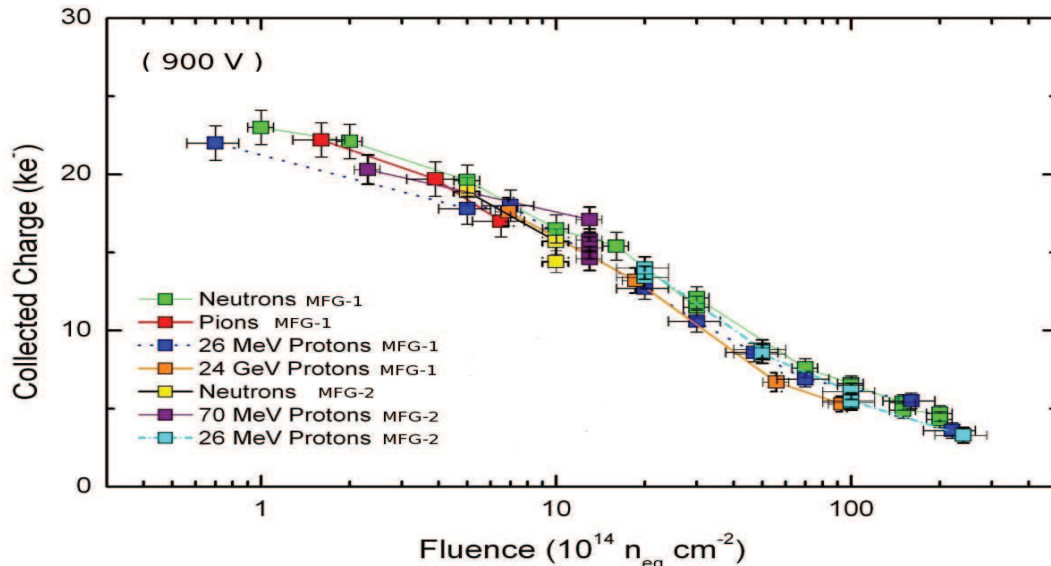


Figure 4.6: Collected charge as a function of fluence up to $2 \times 10^{16} \text{ n}_{eq} \text{ cm}^{-2}$ with planar sensors made by two different manufacturers (MFG) biased to 900 V.

862 Concerning the 3D-silicon sensors, as can be seen from Fig. 4.3 b), after $5.0 \times 10^{15} \text{ n}_{eq} \text{ cm}^{-2}$
 863 the most probable signal is 12000 electrons.

864 4.4.3 Cooling

865 The operating temperature of -10 or -15 degrees is enough for AFP (-15 degree is a baseline
 866 for IBL). Low temperature detector operation extends the detector lifetime and it is needed
 867 especially at the end of data taking, when the detector is already heavily damaged (highly
 868 irradiated). In fact low temperature cooling should not be the same issue for AFP as it is for
 869 IBL since one can exchange part of the silicon detector during any winter LHC shutdown

870 The power to be evacuated is really rather small. The nominal power of one FE-I4 is 1 —
 871 1,5 W and in addition, we have 0,25 W due to the silicon sensor itself.

872 There are three different cooling approaches under considerations based on experience ob-
 873 tained during development of the detector cooling systems for the ATLAS Inner Detector and
 874 the TOTEM detectors. The three options, outlined below, are being tested with simulated heat
 875 loads ranging from hundreds to a thousand watts:

- 876 1. The modified cooling system, which is based on the TOTEM project solution. The selec-
 877 tion of this option depends on the available space for the plant.
- 878 2. The thermosiphon cooling system (prototype under development).

879 3. The Vortex-based Dry Air Cooling System (DACs). A laboratory-scale prototype is avail-
880 able with power up to 500 W per cooling unit with a possibility to manipulate cooling air
881 temperature between -40° and -10° .

882 The choice of the coolant for the first two systems was based on its dielectricity, thermodynamic
883 characteristics and its radiation hardness, and is oriented towards fluorocarbon fluids, namely
884 C_3F_8 . Technology of such systems is well tested and understood. Nevertheless, unavoidable
885 difficulties with these options are the expected large distance between the cooling plant and
886 the targets (detector plus electronics) to be cooled down, resulting in rather long refrigerant
887 pipelines. While the decision and full study is still in progress, the third solution is the preferred
888 one, since its small size and use of dry air as coolant allows for local placement next to the
889 detector and electronics, and we favour this solution with respect to the CO_2 one chosen by
890 IBL due to its simplicity. Tests with realistic AFP detector engineering mockups are envisaged.
891 These should include design supports with integrated cooling channels respecting the geometrical
892 layout of the equipment.

893 4.5 Ongoing research and development

894 Once the sensor choice is made, the mechanics and cooling will be developed, and prototypes
895 will be built and tested.

896 4.6 Conclusion

897 Although the final sensor choice has yet to be made, the switch from the FE-I3 to FE-I4 readout
898 chip has dramatically simplified the silicon tracker design for the 220 m region. Given that
899 the sensor choice is made within the next few months, the other issues (mechanics, cooling,
900 etc.) will naturally fall into place and there will be sufficient time for prototyping, production,
901 and installation, of the 5-plane AFP silicon detector system (four of these are needed to fully
902 instrument the 220 m region). Using the same readout technology as the IBL project enables
903 us to forgo extensive R&D with its concomitant costs and manpower requirements.

Chapter 5

Fast Timing System

5.1 Introduction

Overlap background due to multiple proton-proton interactions in the same bunch crossing will become prevalent at the LHC as the instantaneous luminosity increases. Much of this background can be removed by kinematical matching between the central system as measured by the central detector (for example, jets from Higgs decay), and inferred from the protons measured in the AFP silicon detectors. For rare processes, the background may still be too large to make a significant measurement, motivating the fast time-of-flight detector. Consider an event with a central massive system and two oppositely directed small angle protons. If the protons are from the same interaction as the central system, the position of the vertex as measured by the central tracks will be consistent with the position as determined from the time difference of the outgoing protons. A time resolution of 10 ps corresponds to a 2.1 mm vertex position resolution, which given the approximately 5 cm width of the luminous region and the 50 μm uncertainty of the central vertex will yield an additional rejection factor of about 20 against this fake background.

5.2 Timing system requirements

The final timing system should have the following characteristics

- 10 ps or better resolution
- acceptance that fully covers the proton tracking detectors
- efficiency near 100%
- high rate capability ($O(10)$ MHz/pixel)
- segmentation for multi-proton timing
- Level 1 trigger capability
- radiation tolerant
- robust and reliable

930 For the first stage, 220 m at modest luminosity, the requirements are not quite as stringent:
931 20 ps resolution will suffice, the rate should not exceed 2 MHz/pixel, and the Level 1 trigger
932 capability is not strictly necessary.

933 Another important aspect for this system is its stability and monitoring. For this reason,
934 we are planning to add an ADC to measure the pulse height, which would allow us to monitor
935 any PMT aging effects and also to perform a residual time walk correction. In addition, we are
936 adding a fiber pulser system which will also allow us to monitor the whole electronics chain.
937 Finally, we will collect samples of hard diffractive events with two protons and two central jets
938 that can be used to monitor the stability of the z-vertex position.

939 Since the driver for the highest precision of timing is pileup at the highest luminosity levels,
940 especially for light resonances, it is clear that 20 or 30 ps is adequate for the first stage when we
941 only have 220 detectors. We will, of course, have the best possible resolution for 220 m that we
942 can obtain in 2013: we believe this will be ~ 10 ps. It is likely that parts of the system would
943 be upgraded in a 420 m stage leading to better timing resolution.

944 5.3 Timing system components

945 The main components of the timing system are: i) the detector comprised of the radiator that
946 produces light when a proton passes through it and the photo-sensitive device that converts the
947 photons into an electrical pulse; ii) the electronics system that reads out the pulse and interfaces
948 with the ATLAS data acquisition and trigger system; and iii) the reference timing system that
949 provides a low jitter clock signal allowing the correlation of the detector stations which are
950 hundreds of metres apart. Below we describe each of these components.

951 5.3.1 The detectors

952 Typically high energy physics time-of-flight detectors have a resolution of about 100 ps [48], an
953 order of magnitude worse than our requirements. Recently spurred by a sub-10 ps measurement
954 obtained in Ref. [49], the focus for dramatically improving time-of-flight resolution has turned
955 towards detectors employing a quartz Cerenkov radiator coupled with a microchannel plate
956 photomultiplier tube (MCP-PMT).

957 We note that the detector design of Ref. [49] does not suit our needs, since it requires putting
958 the MCP-PMT directly in the beam. Over the past several years, we have studied Cerenkov
959 detectors with gas (GASTOF) and quartz (QUARTIC) radiators [50, 24, 1]. Cerenkov radiation
960 is emitted along a cone with an angle defined by the Cerenkov angle $\theta_c \approx \cos^{-1}(1/n)$, where n
961 is the index of refraction of the radiator.

962 Figure 5.1(a) shows a schematic diagram of the QUARTIC detector, which consists of four
963 rows of eight $5 \text{ mm} \times 5 \text{ mm}$ quartz or fused silica bars ranging in length from about 8 to 12
964 cm and oriented at the average Cerenkov angle ($\sim 48^\circ$ for quartz). Photons are continuously
965 emitted as the proton passes through the bars; those emitted in the appropriate azimuthal
966 angular range are channeled to the MCP-PMT. Any proton that is sufficiently deflected from
967 the beam axis will pass through one of the rows of eight bars, providing, in principle, eight
968 independent time measurements along the track, and an overall resolution that is $\sqrt{8}$ smaller
969 than the single bar resolution of 30 ps. Our studies have shown that there are various cross
970 talk effects that correlate the measurements, dominated by optical and charge sharing between
971 neighboring channels. Due to the isochronous detector design, however, the cross talk signal is
972 approximately in-time, as a result we do observe the \sqrt{n} scaling of the single bar resolution.

973 Figure 5.1(b) shows a schematic diagram of the GASTOF detector. It has a gas radiator

974 at 1.3 bar in a rectangular box of 20 to 30 cm length, with a very thin wall adjacent to the
 975 Hamburg pipe pocket. The protons are all essentially parallel to the axis. A thin 45° concave
 976 mirror at the back reflects the light to an MCP-PMT. The gas used in tests is C₄F₈O, which is
 977 non-toxic and non-flammable, and has a refractive index of $n = 1.0014$ giving a Čerenkov angle
 978 ($\beta = 1$) of 3.0°.

979 Figure 5.1(c) shows a schematic of an MCP-PMT which consists primarily of a photocathode
 980 and microchannel plates. The photo-cathode converts the radiation to electrons, and the MCP's,
 981 which are lead glass structures with an array of 3 to 25 micron diameter holes (pores), serve as
 982 miniature electron multipliers converting the incoming photons to a measurable signal for the
 983 downstream electronics. Phototubes under consideration for QUARTIC Stage 1 are the Photonis
 984 Planacon a 64 channel 2 inch square tube with either 10 or 25 μm pores, or the Hamamatsu
 985 SL10 a 16 channel 1 inch square tube with 10 μm pores, while a Photek 210 single channel 1 cm
 986 tube with 3 μm pores or a Hamamatsu R3809U-50 with 6 μm pores are the leading candidates
 987 for GASTOF.

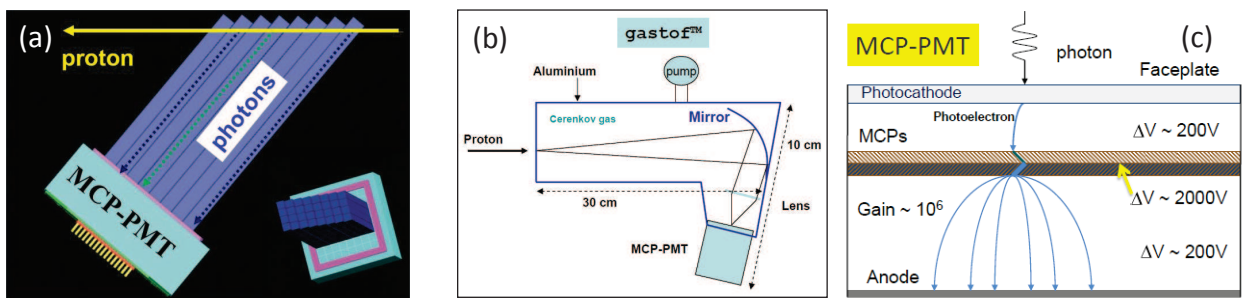


Figure 5.1: (a) A schematic side view of the proposed QUARTIC time-of-flight counter, which shows Čerenkov photons being emitted and channeled to the MCP-PMT as the proton traverses the eight fused silica bars in one row. The inset shows a rotated view with all four rows visible. (b) A schematic view of the proposed GASTOF time-of-flight counter. (c) A schematic view of an MCP-PMT as described in the text.

988 The AFP R&D effort has focussed on the QUARTIC detector, which is segmented and
 989 thus meets the requirements of Sec. 5.2 better than the GASTOF detector. The QUARTIC
 990 longitudinal segmentation provides multiple measurements of the same proton, reducing the
 991 necessary precision for any single measurement to 30 to 40 ps, while the transverse segmentation
 992 provides the ability to measure multiple protons in the same detector. It is also useful to have
 993 a GASTOF, however, since it makes one excellent measurement (better than 20 ps), providing
 994 a useful cross check for QUARTIC.

995 5.3.2 The electronics

996 The electronics system is designed to provide a 20 ps or better resolution measurement of
 997 the time-of-flight of protons scattered at small angles, provide a Level 1 trigger, and record
 998 the time measurements in the ATLAS data stream. The electronics are optimized for the
 999 QUARTIC detector, which makes multiple measurements in the 30 ps range, but can also be
 1000 used for GASTOF, which makes a single measurement in the 10 to 20 ps range. Figure 5.2
 1001 presents a schematic overview of the electronics system and includes photos of the primary
 1002 constituents: pre-amplifiers, constant fraction discriminators, trigger, and high precision time-
 1003 to-digital converters (HPTDC). The reference timing system, which provides a stable clock
 1004 signal, is described in Sec. 5.3.3.

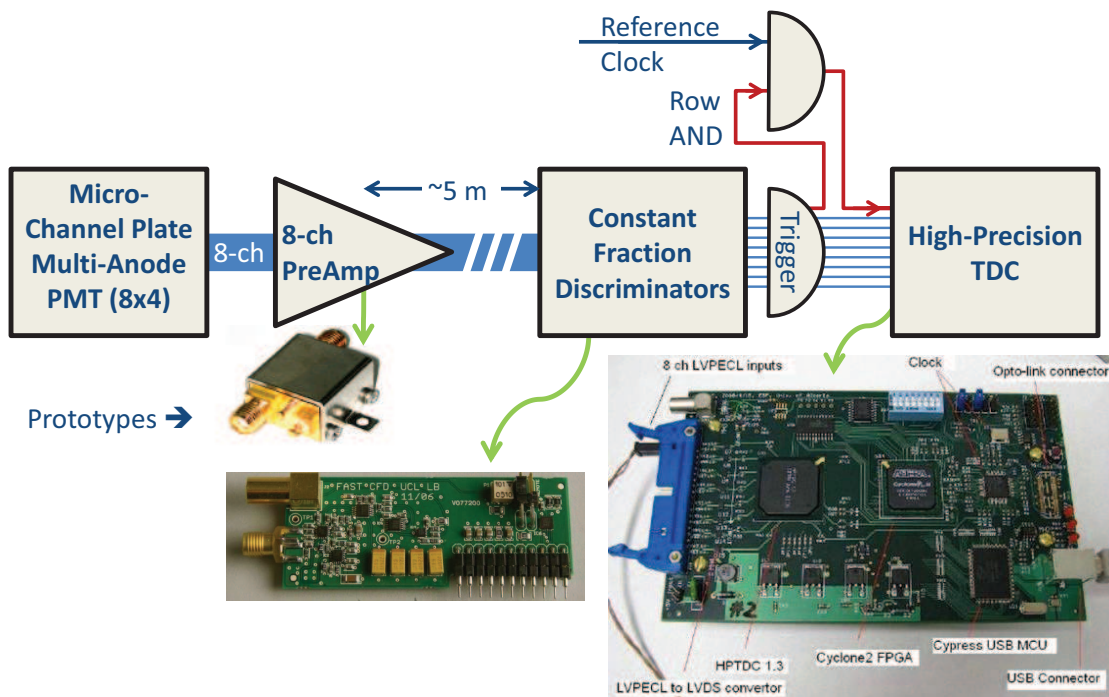


Figure 5.2: A schematic diagram of the electronics chain described in the text. The photographs show a low noise Minicircuits ZX60 pre-amplifier, a constant fraction discriminator daughter board, and the HPTDC board used in laser and beam tests.

1005 **Pre-amplification.** Given proton rates on the MHz level, the MCP-PMT gain should be
 1006 as low as possible to maximize the device lifetime and minimize the saturation of the pores.
 1007 We have determined that a $\times 50$ pre-amplification allows us to run the Burle Planacon tube
 1008 at low gain, while still yielding the several hundred mV signals required for optimal timing
 1009 performance. In Sec. 5.5 we show that for multiple photoelectrons one can run at lower gain
 1010 without compromising the timing resolution. The exact gain factor required depends on the final
 1011 choice of the MCP-PMT. Tests have been performed using two $\times 10$ Minicircuits 8 GHz ZX60
 1012 amplifiers in series, separated by a $\times 2$ attenuator and a diode to protect the second amplifier
 1013 from large signals in the case of shower events. Although a bandwidth of 1–2 GHz would suffice
 1014 for a typical multi-anode MCP-PMT (with a rise time of about 400 ps), we did not find an
 1015 amplifier in this bandwidth range that had the desired gain as well as low noise (1 dBm) and
 1016 reasonable cost (\$50 per channel). For the final detector electronics we will replace the ZX60
 1017 with a 3mm \times 3mm Minicircuits QFN low profile surface mount pre-amp, and incorporate this
 1018 and the other discrete components on a PCB board that will plug directly onto the MCP-PMT.

1019 **Constant fraction discriminator.** The amplified signals will then be sent via ~ 30 metre
 1020 long high speed coax cables to the constant fraction discriminator (CFD) boards located in a
 1021 readout crate in the alcove at 240 m. Preliminary tests indicate that a several meter cable
 1022 run does not introduce significant jitter (recall a single measurement requires a precision of
 1023 “only” about 30 ps). Tests of the signal integrity with the final cable type and distance will be
 1024 performed soon. The CFD system is based on a design developed by the University of Louvain
 1025 for FP420 [24] with a NIM unit mother board that filters the NIM power and houses 8 single
 1026 channel CFD daughter boards. These provide a NIM output for testing and an LVPECL output
 1027 to the HPTDC board that digitizes the time. The final system may be VME based instead of
 1028 NIM, and will also form a trigger signal prior to being digitized.

1029 **Trigger.** A coincidence of several CFD channels in the same row can be used to form a
 1030 trigger. The row triggers can be ORed to form a global trigger that can be sent to Level 1
 1031 on a dedicated large diameter air core cable. This global trigger would be satisfied when a
 1032 proton passes anywhere through the detector. A more sophisticated trigger could be formed in
 1033 a second Stage of AFP after the L1 Calorimeter upgrade, by correlating the row trigger with the
 1034 calorimeter η to chose events in a specific mass range. In addition to providing a global trigger,
 1035 the row triggers can be used to limit the occupancy of the HPTDC board by only passing on
 1036 the CFD signals for events that pass a multiplicity cut within a row. These row triggers will
 1037 also be used to filter the reference clock signal, such that the clock signals are only passed to
 1038 the associated HPTDC chips when the row in question has a proton passing through it.

1039 The trigger circuit is still in the conceptual design stage. We plan to implement a simple
 1040 resistive sum of digital CFD signals (or fractions thereof) and input this signal into a fast
 1041 comparator to provide a multiplicity trigger. The ADCMP582 used in the current Alberta CFD
 1042 is the leading candidate for this tas: it has a 200 fs random jitter and 180 ps propagation delay.
 1043 The CFD signals must be delayed by this amount (cable delay) and then be gated. The gate will
 1044 either be built from discrete components or with LVPECL chips and should have small transit
 1045 time and jitter. The random jitter of the output drivers (SY58601 Micrel.com) in the current
 1046 Alberta CFD is less than 1 ps and a typical transit time is 125 ps; other Micrel components,
 1047 like their gates, have the same specification on random jitter and transit times less than 200 ps.
 1048 Recall that an individual QUARTIC measurement is on the 30 ps scale, consequently jitter of a
 1049 few picoseconds in the trigger circuit would not impact the overall system jitter.

1050 **HPTDC board** The filtered CFD and clock LVPECL signals are sent to the HPTDC board
 1051 via ribbon cable. This board uses the 25 ps least bit 8-channel HPTDC chip developed by CERN
 1052 for the ALICE Time-of-Flight detector [51]. Our HPTDC board also includes control signals

1053 and an optomodule which interfaces to the existing ATLAS Readout Driver (ROD). Our studies
1054 indicate that if operated in the standard 8-channel high resolution mode (25 ps least bit), the
1055 occupancy of the HPTDC board will eventually exceed 2 MHz causing a loss of data. Simulations
1056 show that by doubling the internal clock speed to 80 MHz and using only four channels per chip,
1057 the occupancy limit can be increased to 16 MHz at less than 0.1% losses. This capability is
1058 satisfactory for our expected maximum 10 MHz trigger rate, and using the filtering described
1059 above will also reduce the rate of the reference timing signal to acceptable levels.

1060 5.3.3 Reference clock

1061 The final component of the time-of-flight system is the reference clock used to tie together
1062 measurements hundreds of metres apart. Practically, this is done by taking the time difference
1063 with respect to a stabilized clock signal. For the clock signal to cancel in the time difference
1064 it must have a jitter of 5 ps or less, or it would not be negligible relative to the proton time
1065 resolution. The reference timing stabilization circuit is based on a design developed at the
1066 Stanford Linear Accelerator Center (SLAC) by Joe Frisch and Jeff Gronberg (LLNL). It uses
1067 a phase locked loop (PLL) feedback mechanism as shown in Fig. 5.3(a). A voltage controlled
1068 oscillator (VCO) launches a signal down the cable from the tunnel near the proton detector to
1069 the interaction point (IP), where it is reflected and sent back. At the IP end of the cable the
1070 signal is sampled with a directional coupler where it is compared in the mixer with the 400 MHz
1071 Master Reference, provided in this example from the LHC RF signal. The result is a DC voltage
1072 level that is fed back to the VCO to maintain synchronization. Changes in the cable's electrical
1073 length cancel when the original and returned signal are added. A high quality large diameter
1074 air core coaxial cable was used with a 476 MHz RF signal for preliminary tests (the LHC RF is
1075 400 MHz, so minor modifications are needed to adapt the SLAC design), and the stabilization
1076 circuit yielded a 150 fs jitter over a 100 m cable. Figure 5.3(b) shows results from a second test,
1077 with a 300 m cable, which was left outside to verify the temperature stability of the circuit. A
1078 low noise amplifier was used to boost the return signal to recover the cable and power coupling
1079 losses, which are a function of cable length (the measured attenuation was about 7.5 dB for the
1080 300 m cable). The unstabilized circuit was observed to have a variation of 80 ps/10 degrees C,
1081 while the stabilized circuit (shown in the figure) reduced the variation to 4 ps/10 degrees C.
1082 Given that the ambient temperature in the tunnel is stable within a degree or two, the effect of
1083 temperature drift is less than one picosecond.

1084 The stabilized 400 MHz RF wave will then be converted to a 40 MHz square wave that will
1085 provide an input signal to the trigger board, such that the clock will be provided to the HPTDC
1086 only for triggered events. This is necessary to keep the HPTDC occupancy below 15 MHz.

1087 The PLL does need a 400 MHz signal, and we can generate our own signal if not available,
1088 since it is just a time stamp and is not associated with the scattering. We stabilize this generic
1089 400 MHz signal to within a picosecond, and in the tunnel we convert this to a stabilized 40 MHz
1090 signal that we write out with the timing data.

1091 Although this stabilized clock signal can drift with respect to the beam, this is not an issue
1092 since this drift will be identical for both sides and will cancel in the time difference. We will
1093 use double pomeron dijet events, which will provide both central vertices and correlated protons
1094 to calibrate the central vertex and the timing vertex, and monitor the stability of the reference
1095 system.

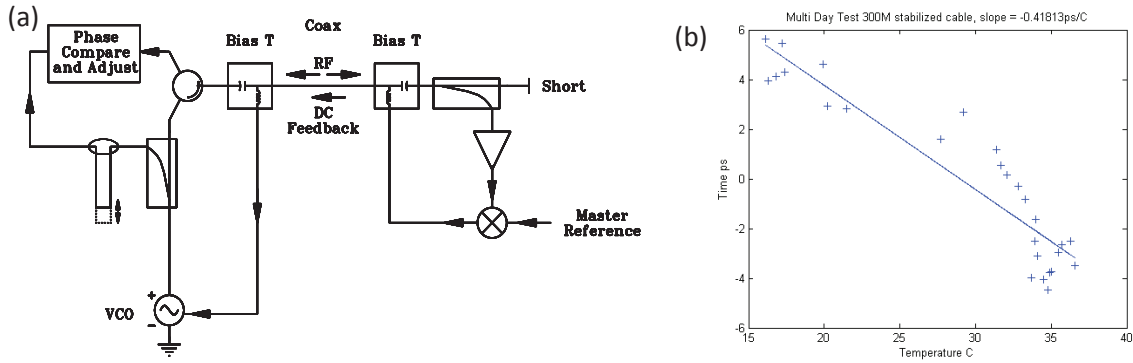


Figure 5.3: (a) Schematic of the Reference timing system as described in text.(b) Results of temperature stabilization test showing a mild drift with temperature (about 4 ps for 10 degrees C).

5.4 Timing system equipment

1096

1097 The Stage I timing system will consist of two to four 32 channel QUARTIC detectors, one or
 1098 two on each side, with a channel count of 64 to 128. Each detector would be readout by one
 1099 Photonis Planacon or two Hamamatsu SL10 MCP-PMTs. The natural unit of the electronics
 1100 is eight channels based on the number of pixels in each row of the Planacon, so we will need 16
 1101 amplifier boards, trigger boards, and HPTDC boards for the four detector option. Including the
 1102 possibility of a two-channel GASTOF detector for each side and two spares, brings the quantity
 1103 of electronics boards to 20. The infrastructure will consist of high voltage for the MCP-PMT's
 1104 (CAEN 1491 or similar, one module required per side plus a spare), low voltage for the amplifiers
 1105 (12 V filtered), five VME crates (two per side plus a spare), and cables. The reference timing
 1106 system will consist of two transmitter boxes, two receiver boxes, and one 300 m high quality
 1107 cables per side. Including a Level 1 trigger cable and a spare for each side brings the total to
 1108 six high quality cables.

5.5 Timing system performance

1109

1110 We have extensively studied the proposed QUARTIC detector, using simulations, beam tests,
 1111 and laser tests. Figure 5.4 (reprinted from the Letter of Intent) shows data from a 2008 CERN
 1112 test beam run with (a) the time difference between between two 90 mm long QUARTIC bars
 1113 interfaced to a Photonis Planacon with 10 μm pores and read out by the constant fraction
 1114 discriminator described above, and (b) the efficiency across the width of a bar. The time
 1115 difference has an rms of about 56 ps, corresponding to 40 ps per bar (assuming the bars are
 1116 equivalent and uncorrelated), while the efficiency is seen to be uniformly greater than 95%
 1117 across the bar. The test beam data are consistent with 10 to 15 detected photoelectrons per bar
 1118 confirming expectations from detector simulations.

1119 Since the 2008 test beam most of the performance testing has been using a pulsed 405 nm
 1120 laser at the UTA Picosecond Test facility. In this setup we replace the light from the detector
 1121 with light from the laser, allowing us to explore in a controlled environment all aspects of the
 1122 system from the MCP-PMT through the electronics. We have obtained a CFD resolution of
 1123 better than 5 ps, assuming that the pulse is sufficiently amplified (typically we amplify the
 1124 pulse to ensure an average pulse height of about 500 mV; pulses above 250 mV have very little

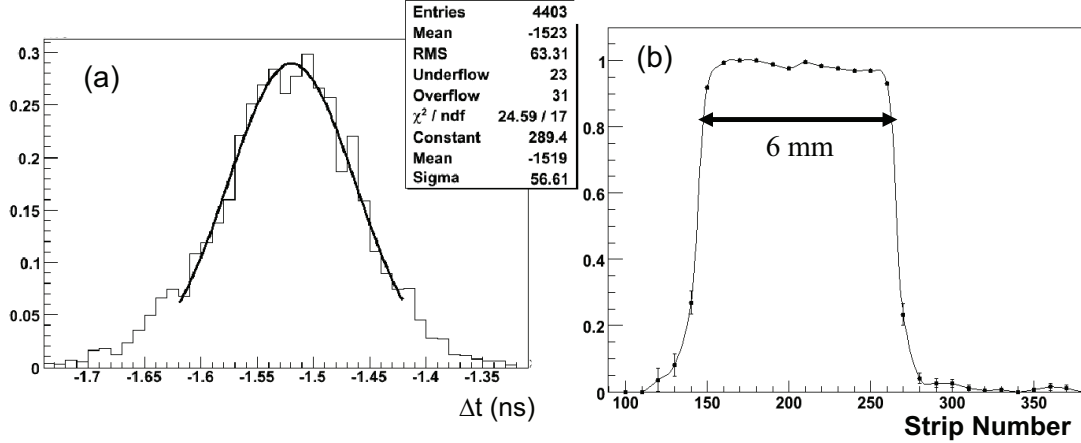


Figure 5.4: (a) The time difference between two 90 mm long QUARTIC bars described in text. (b) the fraction of track events that have a valid time in a QUARTIC bar, as a function of silicon strip number.

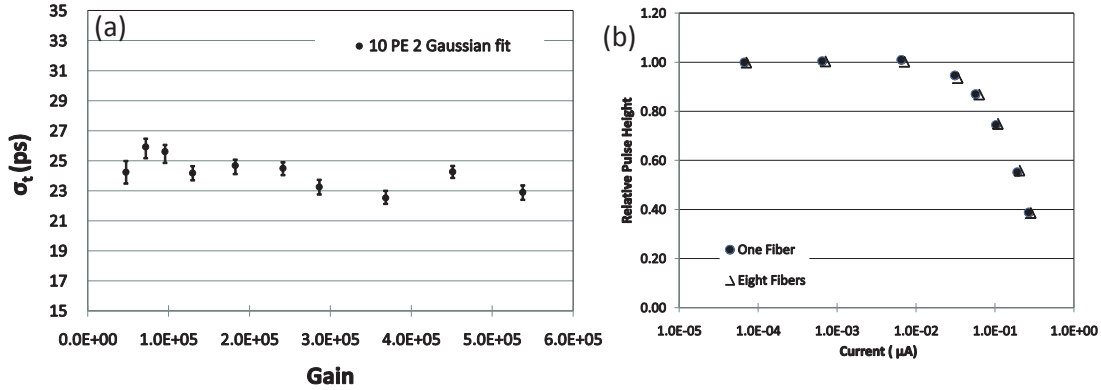


Figure 5.5: (a) Timing resolution versus gain and (b) the relative gain versus current (solid circles with one pixel hit in a row of eight and open triangles when all eight pixels hit in a row) for the 64 channel 10 μm Photonis Planacon tube.

1125 residual timing dependence on pulse height after using the CFD). We have obtained an HPTDC
 1126 resolution of about 14 ps, consistent with pulser tests done at Alberta. The 15 ps overall
 1127 contribution from the CFD/HPTDC is quite acceptable given our overall goal of 30 ps/channel.

1128 Figure 5.5(a) shows a key result from the laser tests, namely that the timing for the 10
 1129 μm pore 64 channel Photonis Planacon tube has very little gain dependence for gains as low
 1130 as 5×10^4 . This result is obtained for a laser setting with 10 pe's, the working point of the
 1131 QUARTIC detector. The validation of low gain running is important as the main technical
 1132 issues regarding MCP-PMTs are rate and lifetime concerns, both of which are reduced by a
 1133 factor 20 compared to operation at the canonical 10^6 gain.

1134 Figure 5.5(b) shows the relative gain as a function of calculated output current for our work-
 1135 ing point. We note for a laser frequency of 5 MHz (last point), corresponding to a calculated
 1136 current of about 0.4 μA over a 0.2 cm^2 pixel, there is about a 60% gain reduction due to satura-
 1137 tion of the pores which have a 1 ms recovery time. For the two previous points, corresponding to
 1138 the expected maximum rates for Stage 1 of 1 to 2 MHz, the gain is only reduced by 20 to 40%. If

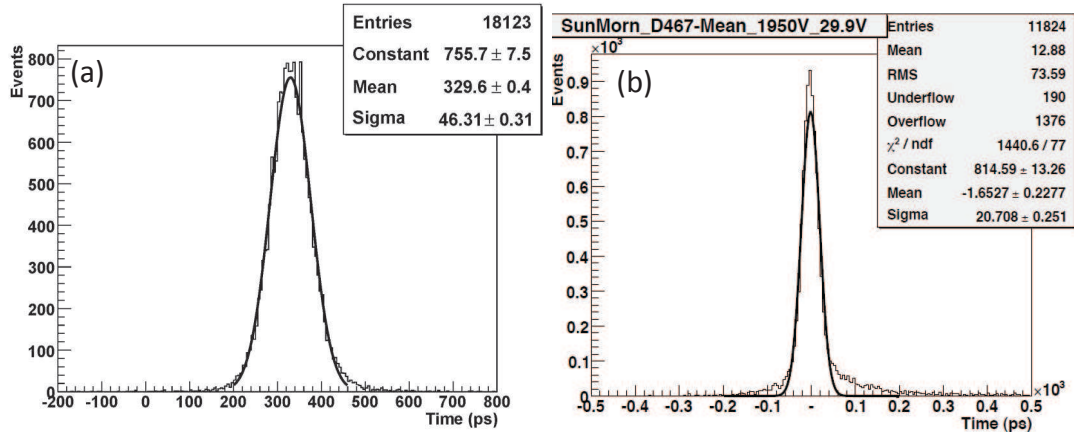


Figure 5.6: Results from November 2010 Fermilab test beam showing (a) the time difference between the CFD signal from two non-adjacent QUARTIC bars (bar 4 and 6) using the LeCroy 8620a oscilloscope (b) the time difference between a reference detector and the average time of three of the QUARTIC bars.

1139 the amplification is augmented sufficiently, the timing resolution is observed to be independent
 1140 of this saturation. This is within a factor of 10 of our expected maximum rate, and this final
 1141 factor can be attained with a high current version of the Photonis tube already developed, thus
 1142 meeting our maximum rate needs. We also note that this single channel result (closed circles) is
 1143 unchanged when fibers are plugged into all eight pixels in a row (open triangles). demonstrating
 1144 that saturation is a local effect.

1145 More recent test beam data (Fermilab November 2010) using a better constructed single
 1146 row prototype detector with a $25 \mu\text{m}$ Planacon yield better results. Figure 5.6 (a) shows the
 1147 time difference as measured with a LeCroy 8620a oscilloscope of the CFD pulse from two non-
 1148 adjacent bars. Although this MCP-PMT has inferior intrinsic time resolution due to the larger
 1149 pore size (versus the $10 \mu\text{m}$ PMT, this is more than compensated for by the higher light yield
 1150 (about 15 photoelectrons per bar) due to a higher quantum efficiency and a better constructed
 1151 detector. The 46 ps width implies a single bar resolution of 33 ps including the CFD. Non-
 1152 adjacent bars were chosen to minimize the correlation between channels. Figure 5.6(b) shows
 1153 the time difference between a reference signal and the average time from three quartz bars.
 1154 The reference signal is obtained using a quartz bar interfaced with a silicon photomultiplier
 1155 (estimated to have 25 photoelectrons and a resolution of 13 to 15 ps). Taking into account the
 1156 resolution of the reference signal, the 20 ps overall resolution implies that the three bar system
 1157 resolution is about 15 ps (note this does not include the HPTDC resolution). Including HPTDC
 1158 resolution we obtain better than 20 ps with 100% efficiency for a single 8 channel detector.

1159 Figure 5.7 shows the time difference between two GASTOF detectors from a 2010 CERN
 1160 test beam run, with $\delta t = 14 \text{ ps}$ (r.m.s.) implying a single detector resolution of 10 ps (measured
 1161 with oscilloscope). Including the HPTDC resolution is expected to result in a better than 20 ps
 1162 measurement, with some inefficiency.

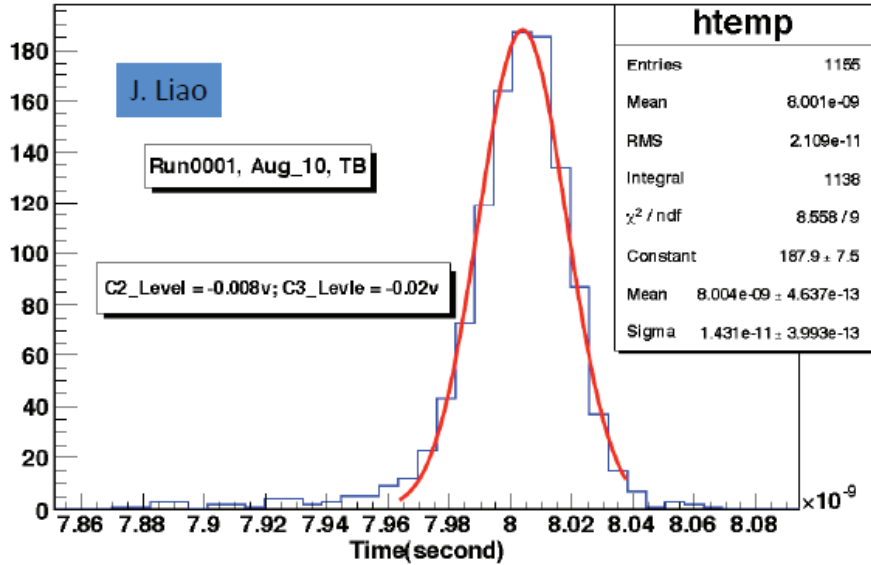


Figure 5.7: The time difference between two GASTOF detectors as described in text.

5.6 Ongoing research and development

We have developed a proof-of-concept of the fast timing detector system demonstrating a sub-20 ps resolution. We believe the current system is capable of 10 ps without any major adjustments, and are working on some minor refinements. There is still R&D in progress on several fronts, as outlined below, although no one in AFP is currently working on the GASTOF detector.

5.6.1 Detector R&D

The detector development effort to date has demonstrated that fused silica bars produce enough light within a reasonable time range to meet our detector resolution goals. Prototype tests have generally been one row (8 channels), while the final detector design needs to be refined to incorporate all the channels, and offset the two detectors to reduce the bin size and avoid “cracks” (regions of poor acceptance). We have preliminary indications that a low pass filter is somewhat beneficial to the overall resolution—less light implies worse resolution, but a narrower color range would reduce the resolution broadening from color dispersion.

Another development issue is reducing the size of detector bins close to the beam, while maintaining the same MCP-PMT pixel size to equalize the rate per unit area. Not only would this improve the multi-proton timing capability (which becomes important at high luminosity, where the overlap background is worst), but it would also reduce the rate and lifetime requirements of the MCP-PMT, which are dominated by the pixels closest to the beam. Variable detector bin size could be achieved most easily with quartz fibers instead of quartz bars, and such an option is being explored by Giessen, but can also be done using quartz bars connected to fibers or channeling the light with short air light guides or Winston cones.

5.6.2 MCP-PMT R&D

A key issue is the degradation of the quantum efficiency of the MCP-PMT photocathode from back-scattered positive ions. We have estimated that at high luminosity the hottest pixels of the MCP-PMT’s would receive 10 to 20 C/cm², which would render them unusable on a few week

1188 time scale, so development of an MCP-PMT with a 20 to 30 times longer life is essential. The
1189 standard approach to improving the lifetime is to add an ion barrier, a thin film that inhibits
1190 the flow of positive ions. The ion barrier method, originally developed for use in night vision
1191 devices [52], has been adapted for MCP-PMT's and has been observed to give at least a factor
1192 of five lifetime improvement [53]. Recent results with the Hamamatsu SL10 indicate that the
1193 lifetime is stable to several C/cm² which could already be acceptable for Stage 1.

1194 UTA is working on a Small Business proposal with Arradance and Photonis, incorporating
1195 atomic layer deposition (ALD) coated MCP's into the Photonis Planacon, and evaluating the
1196 lifetime. Initial results are very promising, and this approach could be used in conjunction with
1197 an ion barrier to provide the life time improvement required for Stage 2. We are also involved
1198 with Photek, another MCP-PMT vendor that is interested in making long life MCP-PMT's
1199 using a more robust "solar blind" photocathode, and could combine this with the other lifetime
1200 improvements into an Ultra long life MCP-PMT.

1201 5.6.3 Electronics R&D

1202 We have developed and tested a prototype of the full electronics chain, but some R&D is still in
1203 progress. We are developing an amplifier PCB board to replace the discrete components, and
1204 the trigger circuit must be validated. The location of the detectors close to the beam pipe but far
1205 from the ATLAS IP, requires moderately radiation-hard electronics on-detector. The location at
1206 220 m from the ATLAS IP has expected radiation levels around $2 \cdot 10^{11}$ neutron-equivalent per
1207 cm² at the beam pipe (this corresponds to a luminosity of 100 fb^{-1} , or 10^7 at an instantaneous
1208 luminosity of $10^{34} \text{ cm}^{-2} \text{ s}^{-1}$) decreasing with distance. At the position of the MCP-PMT and
1209 the pre-amplifier, the levels are expected to be 10^{10} or less. This leads to an integrated dose
1210 on the order of ~ 200 Grays for a luminosity of 100 fb^{-1} . We expect to install the remainder
1211 of the timing electronics will in the alcove at 240 m, where the expected dose is of the order
1212 of 0.1 to 1 Gray). We plan to analyze radiation monitoring data as the luminosity increases,
1213 to develop a more thorough understanding of the radiation environment of the detector. We
1214 then plan radiation studies of the quartz bars or fibers, the amplifier board, and the MCP-PMT
1215 itself. With a lower priority we will irradiate the remote electronics as well. components as well,
1216 but note that all other electronics are located away The mechanics, grounding, and shielding
1217 will have to be studied in detail based on the final choice of MCP-PMT. We also must conduct
1218 further studies to minimize the effect of the coax signal cable runs on the timing resolution and
1219 jitter.

1220 The existing Constant Fraction Discriminator (ALCFD) works well, but it would be beneficial
1221 to have programmable gain (or adjustable attenuation) for optimal CFD performance. We will
1222 also explore the feasibility of adding a low resolution 8 bit ADC for monitoring the MCP-PMT
1223 gain, and perhaps correcting for small or pathological pulses. We plan to route the fast timing
1224 signals to the motherboard where the fast trigger circuitry will be implemented. The fast signals,
1225 the reference time signal, and the row trigger signal will be transmitted via the analog backplane
1226 to the time digitizer modules. A dedicated VME trigger module forms the OR of all row triggers
1227 into a single-arm master trigger for transmission to the ATLAS central trigger processor.

1228 When a trigger occurs, the high-precision reference clock signal is passed along with the
1229 row signals for digitization. The trigger logic must preserve the channel timing resolution and
1230 introduce a channel jitter of less than 5 ps. The trigger logic, although quite straight-forward
1231 remains to be designed and implemented.

1232 We have developed and tested a single chip HPTDC board, but will need to redesign it to use
1233 3 HPTDC chips to account for the 80 MHz internal clock as described above, which limits the
1234 chip to four useful channels, one of which is dedicated to the clock signal. Minor modifications

1235 are needed to the reference timing circuit developed by SLAC to adapt from the 476 MHz SLAC
1236 RF to the 400 MHz LHC RF, and to convert the 400 MHz stabilized clock to 40 MHz and
1237 interface it with the trigger board.

1238 We anticipate that the timing front-end electronics will be developed and tested by 2013, if
1239 either of two pending U.S. grants to support this development are funded. Without funding, we
1240 still expect to be able to develop a working prototype of the entire chain, but would not be able
1241 to build the production version. A first prototype of the amplifier board should be ready for test
1242 beam this summer. The connection to the ATLAS DAQ chain via the RODs can be achieved
1243 within a year. The radiation testing of the front-end amplifier will be carried out within the
1244 next year, allowing time for any necessary iteration of the design.

1245 5.7 Timing summary

1246 We are in the process of developing an ultra-fast TOF detector system that will have a key
1247 role in the AFP project by helping to reject overlap background that can fake our signal. Tests
1248 of the current prototype detector design imply an initial detector resolution of 10 to 15 ps,
1249 including the full electronics chain. For a luminosity of $\mathcal{L} \approx 2 \times 10^{33} \text{ cm}^{-2}\text{s}^{-1}$, a 30 ps detector
1250 would be sufficient to keep the overlap background to the level of other backgrounds for the
1251 dijet channels, and render it negligible for other final states. For $\mathcal{L} \approx 5 \times 10^{33} \text{ cm}^{-2}\text{s}^{-1}$, a 10 ps
1252 detector (still with loose vertex cuts to maximise signal efficiency) would be desirable to keep
1253 overlap backgrounds totally under control, without any loss in signal efficiency. For substantially
1254 higher luminosity, we would control the background by improving the timing detector resolution
1255 to the 5 ps range and/or tightening the vertex window or other background cuts (a factor of
1256 several in rejection is possible with modest loss of efficiency).

1257 The simplest approach to achieving faster timing is minor upgrades to current detector
1258 technologies. For the QUARTIC detector a next generation MCP-PMT with smaller pixel sizes
1259 would allow finer x segmentation for improved multi-proton timing. A smaller pore size would
1260 also be expected to give a modest improvement in the time resolution. Better electronics, such
1261 as a second generation HPTDC chip under discussion (5 to 10 ps least bit) could also give
1262 an incremental improvement and be beneficial for the GASTOF detector which is electronics-
1263 limited. Recent improvements in siPM's are promising (could have a QUARTIC-like design read
1264 out by SiPM's which would avoid the radiation hardness questions by keeping the SiPM's away
1265 from the main flux of particles). We will continue to follow R&D in this area, as well as monitor
1266 advances in other technology for possible upgrades for Stage 2.

Chapter 6

Timescale, Resources, and Conclusions

6.1 Timeline

An overview of major milestones of the AFP Stage I project from now through installation assuming approval:

- *04/2011*: Forward Detector group endorses project, AFP recognized as ATLAS R&D project, AFP group fully integrated in Forward Group
- *7–12/2011*: Development of first silicon prototype and Hamburg pipe prototype, timing detector electronics full chain test with laser
- *end of 2011*: Beam tests of Si and timing detectors
- *2012* AFP recognized as ATLAS upgrade project, finalize R&D, beam test of full system prototype; preparation, submission, and review of TDR
- *beginning of 2013*: Approval of AFP by ATLAS/LHCC and testing of final prototypes
- *2013*: Construction and testing of production detectors, software development
- *1–3/2014*: Installation of 220 m system

A proposal of the timescale for the project is outlined below for the different parts of the project:

- Movable beam pipe
 - *05/2011*: Continue interactions with CMS/LHC Vacuum group on movable beam pipe design
 - *starting Summer 2011*: Safety committee created together with CMS/LHC Vacuum group
 - *beginning 2012*: Construct prototypes of movable beam pipe
 - *mid 2012*: Integrated beam tests with movable beam pipe, QUARTIC, silicon sensors
- Silicon Pixel detectors
 - *Autumn 2011*: First sensors ready - Bump-bonding of first sensors to FEI4 chips by Fraunhofer (Berlin)

- 1295 – *09/2011*: Cabling of bare modules
- 1296 – *12/2011*: First detector ready for beam tests, prototype of cooling system
- 1297 – *end 2011-2012*: Alignment and support studies
- 1298 – *December 2011*: Prototype of cooling system
- 1299 – *end 2012*: Production of final detectors
- 1300 • Timing detectors (see timing chapter for detailed R&D plan)
- 1301 – *fall 2011*: Test beam with fiber detector prototype and quartz bar prototype and full
- 1302 electronics chain
- 1303 – *2012* Radiation tests and finalize electronics and detector design, PMT development
- 1304 continues, final prototype tests
- 1305 – *2013* Tests of production system with final detector and MCP-PMT

1306 6.2 Installation

1307 The proposal is to install the following during the 2013/2014 shutdown:

- 1308 1. the movable beam pipes located at 216 and 224 m on both sides of the ATLAS detector
- 1309 2. cables and fibers in tunnel connecting the AFP stations to ATLAS trigger and readout
- 1310 3. local cables and electronics including LV/HV and reference timing receiver box in alcove
- 1311 near detectors
- 1312 4. silicon tracking detectors (and cooling) in each of the four stations
- 1313 5. QUARTIC timing detectors: one in each 224 m station after silicon

1314 If for some reason only a partial system could be installed, it would be desirable to at
 1315 least complete the first two items, as the last three could in principle be installed during a
 1316 minor access period. We fully expect to have production timing detectors as well, and at a
 1317 minimum would plan to install prototypes. The silicon detector timescale depends critically on
 1318 IBL development. It seems likely that at least some prototypes would be ready for installation,
 1319 while the final detectors might be delayed until the next winter shutdown. If sufficient manpower
 1320 and funds were added to the project (motivated by a BSM Higgs discovery in 2011 for example),
 1321 the proposal could be upgraded to include installation of 420 m detectors as well on the same
 1322 timescale (or else they would have to wait for the next long shutdown).

1323 Following the recommendations from the referees, we decided to simplify the installation
 1324 aims for the 2013-14 shutdown as follows:

- 1325 • **Movable beam pipe:** At 216 m, we will build the movable beam pipe with one pocket
 1326 which will contain the Si detector, while at 224 m, we will have either a two pocket solution
 1327 (same short pocket for the silicon plus another shortish pocket for the QUARTIC) or one
 1328 medium pocket to house both detectors. By fixing the Hamburg pipe length at 50 cm
 1329 or so, we would have one single Hamburg pipe motion system, and could change pocket
 1330 length as needed by simply swapping out that section of pipe in a modest length shutdown.
 1331 Deferring the GASTOF detector will simplify the beam pipe design and avoid the gas flow.
 1332 This can be upgraded in a next phase of the project if needed (the cost of the movable
 1333 beam pipe is moderate as shown further in the document)

Institute	Activity	Manpower Total People	Manpower FTE
Armenia	timing detectors	2	1
Czech Republic	Pixel Si detector Cooling	12	5
France, CEA Saclay	Mechanical Engineering Timing detector electronics	10	4
Germany, Giessen	Timing detectors	2	1
Poland	Power supplies	8	4
USA, Texas Arlington	QUARTIC trigger	3	1.5
USA, Stony Brook	QUARTIC	2	1.3
Alberta, Canada	QUARTIC trigger	4	2

Table 6.1: Minimum manpower foreseen to be available through installation if AFP project approved.

- 1334 • **Silicon detector:** We will follow the IBL decision concerning the type of Si detector
1335 to be built (either n-on-n or 3D). This will allow us to benefit from the IBL experience
1336 concerning the sensors, tests and software developments and to collaborate with them.
1337 If the 3D solution is not chosen, it could be an upgrade of our detector for the 2017-18
1338 shutdown since this is the best detector for us (the edgeless aspect allows to detect protons
1339 closer to the beam, the dead zone being smaller)
- 1340 • **Timing detector:** as we mentioned in the first bullet, we plan to concentrate on QUAR-
1341 TIC detectors only in the first phase of the project and would install one in each 224 m
1342 station.

1343 6.3 Personnel

1344 Due to this project's current lack of status within ATLAS, the active manpower is extremely
1345 limited. The current effort is primarily limited to timing detector R&D. Approval of the technical
1346 proposal would immediately ramp up involvement of several groups as shown in Table 1. Other
1347 groups that have expressed interest would also likely join the effort and new groups would be
1348 recruited.

1349 The manpower available as well as the activities concerning the Si detector which could be
1350 covered by Prague are detailed in Tables 6.3 and 6.3.

1351 6.4 Costing and available or requested budget

1352 A detailed cost for the different parts of the project is given in Tables 6.4, 6.1, 6.4 and 6.4. The
1353 total cost for the project is about 1.9 million CHF, to which we need to add the cost of the two
1354 collimators to be added if the LHC beam division does not pay for it.

1355
1356 The available and requested budgets per country for the project are given in the following
1357 (please note that this is just indicative at this stage of the project):

Task	Planar n-n	3D
Sensor design	IBL	
Sensor production	x	
Sensor lab tests	x	
Flip-chip bonding	IBL	
FE-I4 production	IBL	
Test beams	x	x
Irradiation tests	IBL	x
Module assembly	x	
Installation	x	
DAQ development	x	x
Power supplies	x	x
External services	x	
Off-sensor readout	x	x
Det.Control System	x	x
Cooling	x	x

Table 6.2: Activities which can be performed in Prague in collaboration with the IBL group if the n-on-n or 3D option is chosen.

- 1358 • **Armenia:** Some money can be requested once project is approved.
- 1359 • **Canada:** 70 kCHF available now for engineer/technician salaries, additional money can
1360 be requested once the project is approved
- 1361 • **Czech Republic:** Money is available for wafers, FEI4 chips, n-on-p sensors (production,
1362 tests, flip-chip bonding), if this solution is chosen, as well as cooling of the Si detector
- 1363 • **France:** Some funds will be available to develop Stage II fast timing electronics when the
1364 AFP project is an ATLAS project; engineers can be committed to the project (salaries
1365 paid)
- 1366 • **Germany:** 50% post-doc for timing detector development now, possibility to submit a
1367 funding application to BMBF if project considered as an ATLAS project by the end of
1368 this year
- 1369 • **Poland:** A grant from Polish government can be requested once the project is an ATLAS
1370 project and the MoUs are signed
- 1371 • **USA:** UTA MCP-PMT development project funded (\$150,000), Stony Brook Electronics
1372 technician funded (\$35,000), DOE ADR submitted for timing electronics development
1373 (\$173,000), other fundinf requests planned if approved.

1374 6.5 Conclusion

1375 This Technical Proposal has presented the Stage I plan of the ATLAS Forward Proton (AFP)
1376 upgrade: to add high precision silicon and timing detectors housed in specialized movable beam
1377 pipes at ~ 220 m upstream and downstream of the ATLAS interaction point to detect intact final
1378 state protons scattered at small angles and with small momentum loss. The detectors would be

Task	# people	time
Sensor design and production	2	4m/2011
Test beams	2	2m/2011-2013
Lab tests	4	2m/2011-2012
Irradiation tests	2	1m/2011-2012
Module assembly	2	1m/2011, 4m/2012
Installation	2	4m/2013
DAQ development	2	6m/2011-2013
Power supplies	1	1m/2011-2013
External services	1	1m/2011-2013
Off-sensor readout	1	1m/2011-2013
Det.Control System	1	1m/2011-2013

Table 6.3: Manpower (person month) available for the pure AFP part of the Si detector in case the n-on-n solution is chosen. Much more manpower from Prague is devoted to the IBL project benefitting directly to AFP since we will follow the recommendations from the IBL group.

element	unit cost	total cost
Single/double pocket pipe, flanges, SV box	15	60
Tables	7	28
Bellow units	4.5	36
BPMs	10	120
Movement system (with mechanics)	80	320
Vacuum pump (secondary vacuum)	2	6
Total		570

Table 6.4: Cost of the movable beam pipes (in kCHF).

1379 fully integrated into ATLAS forming a new proton detection capability during standard running
1380 thus enabling a rich QCD, electroweak and beyond the Standard Model experimental program.
1381 For this project to succeed, it must rapidly be declared an ATLAS upgrade project, enabling
1382 funding for the final R&D needed for the Technical Design Report. Given final ATLAS/LHCC
1383 approval by late 2012 and the procurement of sufficient funds it would be possible to install the
1384 full 220 m system in early 2014. Finally, we would like to acknowledge the tremendous work
1385 done by the UK groups which initiated this project and sadly have been forced by their funding
1386 agencies to abandon it.

Item	Minimal System Number	Full System Number	Unit Cost	Minimal Cost	Full Cost	Spare Cost	Min Spare Cost	Min Cost w/spares	Full Cost w/Spares
Detectors									
QUARTIC	2	4	\$7,000	\$14,000	\$28,000	\$14,000	\$14,000	\$28,000	\$42,000
QUARTIC PMT	2	4	\$20,000	\$40,000	\$80,000	\$40,000	\$40,000	\$80,000	\$120,000
GASTOF		2	\$8,000	\$0	\$16,000	\$8,000		\$0	\$24,000
GASTOF PMT		2	\$24,000	\$0	\$48,000	\$24,000		\$0	\$72,000
Gas System		2	\$14,000	\$0	\$28,000	\$2,000		\$0	\$30,000
Detector Cost				\$54,000	\$200,000	\$88,000	\$54,000	\$108,000	\$288,000
Electronics									
8-ch Preamps	8	18	\$400	\$3,200	\$7,200	\$800	\$800	\$4,000	\$8,000
8-ch CFD	8	18	\$3,400	\$27,200	\$61,200	\$6,800	\$6,800	\$34,000	\$68,000
HPTDC	8	16	\$3,450	\$27,600	\$55,200	\$6,900	\$6,900	\$34,500	\$62,100
8-ch ADC	10	18	\$128	\$1,280	\$2,304	\$256	\$256	\$1,536	\$2,560
Trigger Logic	2	2	\$2,500	\$5,000	\$5,000	\$2,500	\$2,500	\$7,500	\$7,500
Calibration Pulsar	2	2	\$3,600	\$7,200	\$7,200	\$3,600	\$3,600	\$10,800	\$10,800
Reference clock	2	2	\$17,150	\$34,300	\$34,300	\$17,150	\$17,150	\$51,450	\$51,450
Electronics Cost				\$105,780	\$172,404	\$38,006	\$38,006	\$143,786	\$210,410
Cables									
Clock Cables	2	2	\$7,800	\$15,600	\$15,600	\$15,600	\$15,600	\$31,200	\$31,200
Trigger Cables	2	2	\$7,800	\$15,600	\$15,600	\$15,600	\$15,600	\$31,200	\$31,200
HV cables			\$5,000	\$5,000	\$5,000	\$500	\$500	\$5,500	\$5,500
Low Voltage Cables			\$5,000	\$5,000	\$5,000	\$500	\$500	\$5,500	\$5,500
Other Cables			\$10,000	\$10,000	\$10,000	\$1,000	\$1,000	\$11,000	\$11,000
Fibers			\$5,000	\$5,000	\$5,000	\$500	\$500	\$5,500	\$5,500
Cable Cost				\$56,200	\$56,200	\$33,700	\$33,700	\$89,900	\$89,900
Infrastructure									
HV	2	2	\$10,000	\$20,000	\$20,000	\$10,000	\$10,000	\$30,000	\$30,000
LV	2	2	\$5,000	\$10,000	\$10,000	\$5,000	\$5,000	\$15,000	\$15,000
VME-type crates with PS	2	2	\$7,500	\$15,000	\$15,000			\$15,000	\$15,000
VME-ROD controller	2	2	\$5,000	\$5,000	\$5,000			\$5,000	\$5,000
ROD	2	2	\$6,000	\$5,000	\$5,000			\$5,000	\$5,000
TTC Modules	2	2	\$5,000	\$10,000	\$10,000			\$10,000	\$10,000
Infra cost				\$65,000	\$65,000	\$15,000	\$15,000	\$80,000	\$80,000
TOTAL COST				\$280,980	\$493,604	\$174,706	\$140,706	\$421,686	\$668,310

Figure 6.1: Costs for the timing detectors. The number in red are not yet precisely known.

50 chips/5 wafers	Planar n-n	3D
masks	11.5	
wafers	0.7	
processing	6.4	
testing	0.5	
Total	19.1	30.8

Table 6.5: Cost of the chips and wafers for the n-on-n and 3D options.

System	Item	Description	Cost (kCHF)	
			IBL	AFP220
Module	1	Sensor - prototype, production, procurement & QC	752	15
	2	FE-I4 prototype, production, test	1372	100
	3	Bump-bonding, thinning, bare module -prototype, prod. & QC	726	100
Stave	4	Local support: CF structure, TM, pipe-prototype, prod. & QC	467	46.7
	5	Module assembly, stave loading, flex-hybrid, internal electrical services - design, prod. & QC	436	43.6
Off-detector	6	R/O chain: opto-board, opto-fiber, TX/RX, BOC, ROD, TDAQ (S-link, TIM, SBC, ROS, crate)	1025	102.5
	7	Power chain: HV/LV PS, PP2 regulators, type 2, 3 & 4 cables, interlocks, DCS	505	50.5
Integration	8	Integration in SR1 & System test	492	49.2
Cooling plant	9	Cooling plant & cooling services to PP1	461	100
Total			6236	608

Table 6.6: Costs of the Si detector for IBL and AFP.

Chapter 7

Appendix I: LHC physics debris collimation studies and their impact on AFP detectors acceptance

This chapter is a summary of a sLHC project note written by F. Roncarolo, R. Appleby, K. Potter, P. Bussey and C. Bracco, CERN-sLHC-Project-Note-0029.

7.1 Introduction

The ATLAS Forward Proton (AFP) group is proposing to upgrade the forward region of ATLAS by installing forward proton detectors at 220 m from the interaction point on both sides of the LHC ATLAS experiment. For this purpose, at 220 m location, it is proposed to install movable beam pipes which will host silicon tracking and fast timing detectors (i.e. four independent detector stations). The detectors are designed to operate at intermediate and high instantaneous luminosities of up to $10^{34} \text{ cm}^{-2} \text{ s}^{-1}$.

At 220 m a system similar to that developed for FP420 is proposed. The 220 m region is less demanding than the 420 m one from an engineering perspective since a cryogenic bypass is not required. However, the experimental acceptance at 220 m is dependent upon the setting of two collimators designed to protect the LHC straight section and dispersion suppressor around ATLAS (and CMS) from the physics debris generated at the two high luminosity experiments. Such two collimators (at about 140 m and 190 m from the IP) are foreseen to be in a closed position, as needed for machine protection, for luminosity higher than a few $10^{33} \text{ cm}^{-2} \text{ s}^{-1}$.

7.2 IR layout and present collimation scheme

The layout of the first 250 m on the right side of ATLAS is shown in Fig. 7.1, in which the proposed location of the AFP detectors at 220 m is indicated. The two collimators presently foreseen for operation at high LHC luminosity runs are also indicated. Throughout the note these two collimators will be labelled as TCL4 and TCL5. The location for a possible new collimator (TCL6), that will be discussed later in this note, is also indicated. For the issues discussed here, the layout of the left side of ATLAS is practically symmetric.

Both TCL4 and TCL5 are installed on the beam pipe hosting the LHC beam that emerges from ATLAS, after the beam pipes divided. TCL4 has been designed to protect the separation dipole D2 from physics debris and also the first matching section quadrupole Q4 and possibly other

1417 downstream magnets. TCL5 has been designed to protect Q5 and possibly other superconductive
 1418 elements down to the dispersion suppressor (DS) at about 400 m. TCL5 was proposed in the
 1419 year 2000, before any proposal for a TCL4, and the details can be found in [54], where the
 1420 authors proved with simulations the need for the protection of Q5 and estimated the beneficial
 1421 effects of TCL5 in terms of beam losses reduction in the DS region. At the end of their note,
 1422 they assess the need for a TCL4 collimator without presenting detailed studies. The TCL5
 1423 studies were performed using the LHC optics Version 6.1 and the presented results give as $15 \sigma_x$
 1424 a convenient collimator half gap for guaranteeing the LHC protection.

Given the TCL4 and TCL5 interference with the proposed AFP physics, the availability of

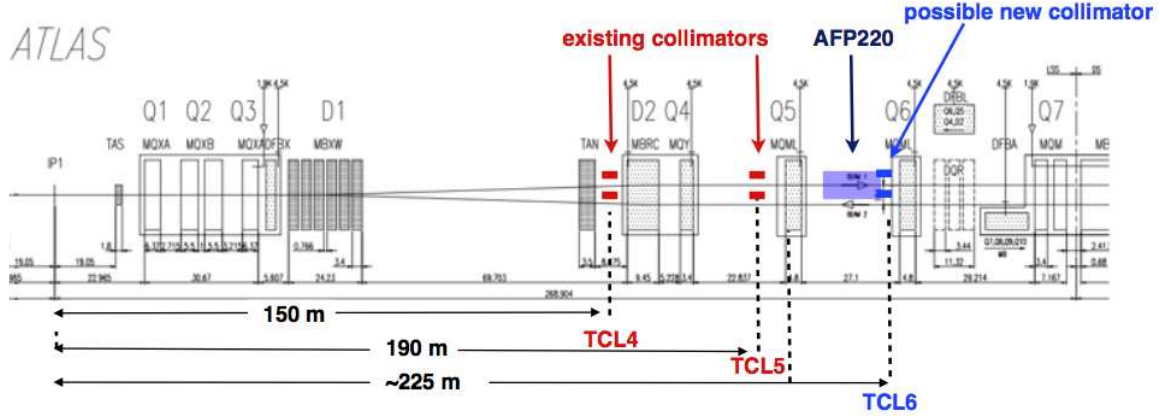


Figure 7.1: Layout of the straight section on the right side of ATLAS.

1425 the new LHC optics Version 6.503 and the lack of information about the TCL4 effectiveness,
 1426 the AFP collaboration decided to carry out a new study in order to investigate a physics debris
 1427 protection scheme that allows safe LHC operation as well as full forward protons acceptance at
 1428 220 m. In the following sections, we present the result of analytical considerations accounting
 1429 for the new LHC optics and of numerical simulations aimed at generating beam loss patterns
 1430 for different collimation settings.
 1431

1432 7.3 Optimal collimator settings as studied with beam optics cal- 1433 culations

1434 According to linear beam dynamics, the transverse motion of particles has two amplitude terms.
 1435 The betatronic one is described by the betatron functions $\beta_{x,y}(s)$ variation along the accelerator
 1436 structure. A second term is proportional to the particle momentum offset with respect to
 1437 the reference momentum dp/p , with the dispersion function $D_{x,y}(s)$ as proportionality factor.
 1438 Considering the horizontal plane, the maximum excursion of a particle with momentum offset
 1439 dp/p as function of location s is equal to:

$$x_{max}(s) = \sqrt{\beta_x(s)\epsilon_x + \left[\frac{dp}{p} \cdot D_x(s)\right]^2}, \quad (7.1)$$

1440 where ϵ_x is the geometric horizontal emittance describing the particle mapping of the horizontal
 1441 phase space. The horizontal trajectories of a 7 TeV proton and of three off-momentum protons
 1442 (with $dp/p = -1 \cdot 10^{-3}$, $-1 \cdot 10^{-2}$ and $-1 \cdot 10^{-1}$ respectively), as calculated with PTC [55] using

1443 the MADX LHC optics V6.503, are shown in Fig. 7.2. Since in all four cases the tracking starts
 1444 at IP1 with $(x,x',y,y') = (0,0,0,0)$, there is no betatronic contribution and the particle deviation
 1445 from the reference orbit is only due to the energy dependent term of Eq. 7.1.

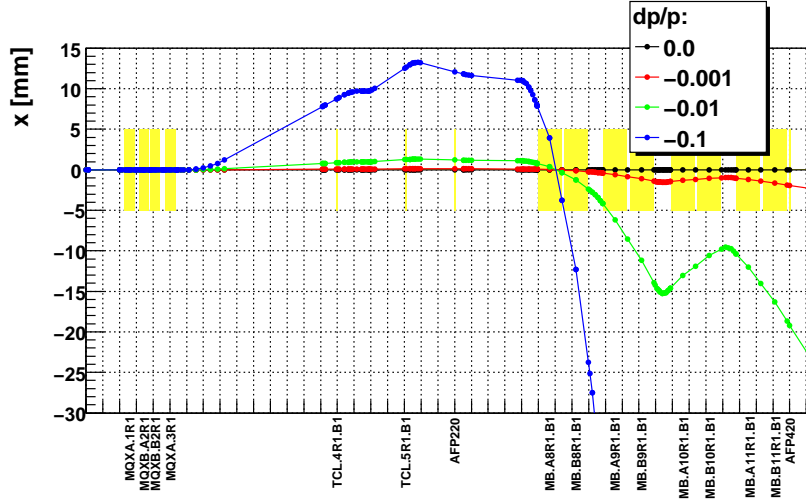


Figure 7.2: Horizontal trajectory of a 7 TeV proton and of three off-momentum protons, as simulated with PTC. For all particles the initial coordinates are at $(x,x',y,y') = (0,0,0,0)$.

1446

1447 Assuming a collimator at a location $s = s_c$ with a full gap centered around the reference
 1448 beam closed orbit, it is possible to determine the minimum collimator half gap ($x_c(s)$ or $y_c(s)$)
 1449 necessary to intercept a particle with momentum offset dp/p . Considering the horizontal plane,
 1450 such a quantity defined in units of the betatronic beam size $\sigma_x(s) = \sqrt{\epsilon_x \beta_x(s)}$ results:

$$\frac{x_c(s)}{\sigma_x(s)} = \frac{D_x(s)}{\sigma_x(s)} \cdot \frac{dp}{p} = \frac{D_x(s)}{\sqrt{\beta_x(s)\epsilon_x}} \cdot \frac{dp}{p} = \frac{1}{\epsilon_x} \cdot D_x^n(s) \cdot \frac{dp}{p}, \quad (7.2)$$

1451

1452 where $D_x^n(s) = D_x(s)/\sqrt{\beta_x(s)}$ is called the *normalized dispersion* function. The normalized
 1453 dispersion and the collimator half gap, as defined in Eq. 7.2, are shown in Fig. 7.3 and Fig. 7.4
 1454 respectively, for the two LHC beams outgoing from IP1. It must be noted that in this case D_x
 1455 is the *unmatched* dispersion function (different from the periodic lattice dispersion) accounting
 1456 for the fact that protons experience a $D_x = 0$ at the location where they are generated (the IP).
 1457 The necessary collimator half gap has been plotted for three values of the proton momentum
 1458 offset with respect to 7 TeV ($dp/p = 2 \cdot 10^{-2}, 5 \cdot 10^{-2}$ and $10 \cdot 10^{-2}$) that cover the range of
 1459 particles that needs to be intercepted in order to minimize the risk of quenching superconductive
 1460 elements in the long straight sections and dispersion suppressors. The location of the two existing
 1461 collimators (TCL4 and TCL5) and of a possible additional collimator (TCL6) are indicated. As
 1462 an example these calculations indicate that, for intercepting a proton with $dp/p = 2 \cdot 10^{-2}$ (black
 1463 line in the figure), TCL5 needs to be closed to less than $10 \cdot \sigma_x$ whereas it would be enough to
 keep TCL6 at about $35 \cdot \sigma_x$.

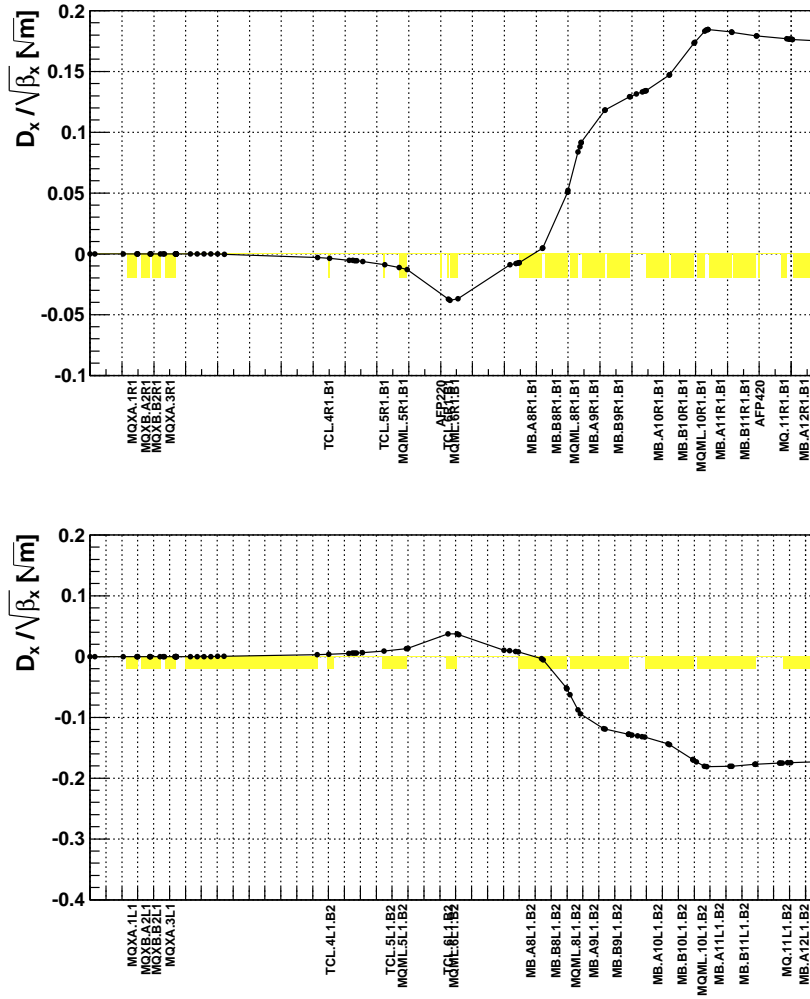


Figure 7.3: Normalized horizontal dispersion in the straight section on the right side of ATLAS for Beam 1 (top) and on the left side for Beam 2 (bottom).

7.4 Numerical simulations setup

1464

1465 In order to confirm the analytical calculations discussed above, a set of numerical simulations
 1466 have been implemented. The numerical simulations consisted in tracking distributions of pro-
 1467 tons, representing a sample of forward protons generated by p-p collisions, downstream, in the
 1468 LHC straight section and dispersion suppressor. The tracking included the best available ap-
 1469 proximation of the LHC physical aperture and were performed with different collimator settings
 1470 in order to evaluate the effectiveness of the machine protection. Two tracking codes have been
 1471 used and compared:

- 1472 - PTC (Polymorphic Tracking Code) [55], that is based on a 'thick lens' model of the accelerator
 1473 elements and offers an exact Hamiltonian of the magnetic elements; in such a way the
 1474 trajectory of off-momentum protons is described in the best approximation available for the
 1475 LHC model; the simulations performed with PTC considered any aperture limit, including
 1476 collimators, as black absorbers.

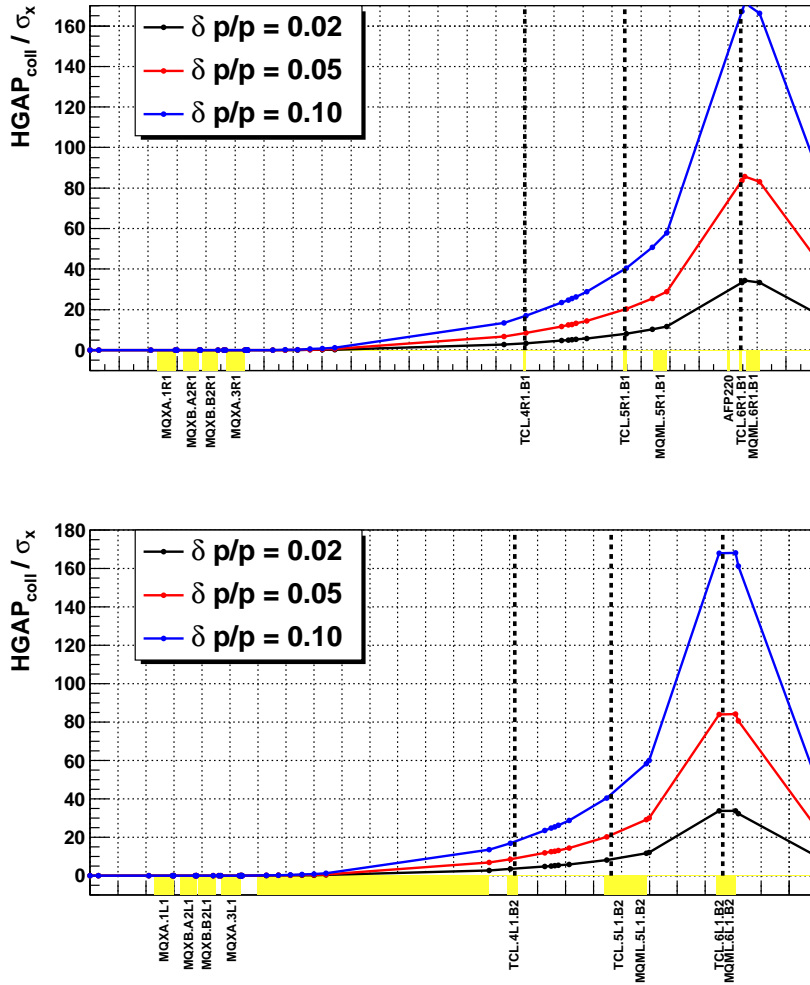


Figure 7.4: Collimators horizontal half gap necessary to intercept protons with 3 different momentum offsets as function of collimator position, for Beam 1 (top) and Beam 2 (bottom).

1477 - SIXTRACK [56], that is based on a 'thin lens' model of the accelerator elements; in particular,
 1478 a special version of the code including the COLLTRACK tools, that has been designed for
 1479 fast multi-turn tracking and extensively used for designing the LHC collimation system;
 1480 SIXTRACK is supposed to be less accurate in tracking protons with more than 10%
 1481 momentum offset, but has the advantage of simulating elastic and inelastic scattering on
 1482 the collimators. Therefore, with respect to PTC, it does not neglect the contribution of
 1483 scattered protons to the losses on the downstream superconducting elements.

1484 Both codes have been interfaced to the MADX LHC optics V6.503 and were given the same LHC
 1485 aperture model. The aperture model used for the right side of IR1 is shown in Fig. 7.5. The
 1486 plot covers the region from $s=0$ to $s=230$ m, even though the aperture has been modeled and
 1487 considered by the tracking up to 450 m. The considered aperture model was the one available
 1488 in MADX at the moment of the simulations and may well be replaced by better approximations
 1489 for future studies. Despite some uncertainties (e.g. vertical aperture of experimental beam pipe
 1490 before the TAS) the studies presented here focus on comparisons between different codes and
 1491 different collimator settings and the results significance must be considered as unbiased.

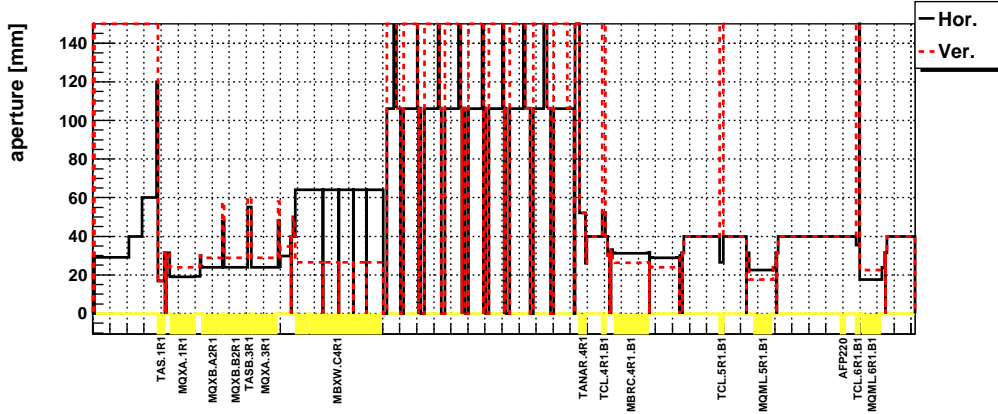


Figure 7.5: Aperture model in the first 230 m from IP1 (Beam 1), used for both the PTC and SIXTRACK simulations.

7.5 Numerical simulation results

7.5.1 PTC loss maps without collimators

For all results presented in this document, the loss maps refer to forward protons generated at IP1 and tracked along the LHC Beam 1 direction (right side of ATLAS) for 450 m in the dispersion suppressor region. For the LHC design, the majority of the DPMJET protons surviving this region will be lost in the cleaning insertions IR3 and IR7.

The first set of loss maps produced with PTC has been performed without TCL collimators installed in the lattice and the estimated number of protons per meter and per second at nominal LHC luminosity is shown in Fig. 7.6. Like in many of the figures that will be presented, the horizontal blue line at $8 \cdot 10^6$ $p/m/s$ indicates an estimation of the quench level threshold for the superconductive magnets in the studied region. Such a value assumes that all protons have a momentum of 7 TeV. This approximation is the one used for all machine protection studies before the LHC provides any data.

The average momentum offset (with respect to 7 TeV) of the lost protons and the number of lost protons weighted for the proton momenta are shown in Fig. 7.7 and 7.8 respectively. The three plots yield the following considerations:

- a few peaks of Fig. 7.6 in the final focusing triplets region ($s=0-80$ m) exceed the estimated quench limit. However, since most of the protons lost in this region have very low momentum, all peaks fall below the quench limit when normalizing for the proton momentum, as evident in Fig. 7.8.
- the TAN absorber at about 140 m indeed intercepts a large number of forward protons as indicated by the peak reaching 10^8 protons per meter per second; but it cannot quench.
- the losses along the Q5 quadrupole at about 190 m approach the estimated quench limit and require a protection;
- the estimated losses from about 250 m to the dispersion suppressor result in an order of magnitude safety with respect to the estimated quench limit.

The calculated energy deposition expressed in Watt per meter is shown in Fig. 7.9. The values resulting from the loss maps are well in agreement with the LHC Design Report [57], stating

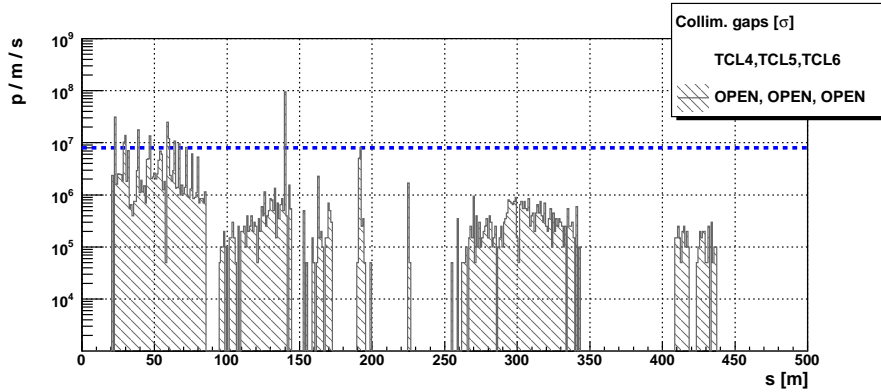


Figure 7.6: PTC loss maps with no TCL collimators installed in the IR1 straight section. The horizontal blue line indicate the estimated quench limit assuming 7 TeV protons.

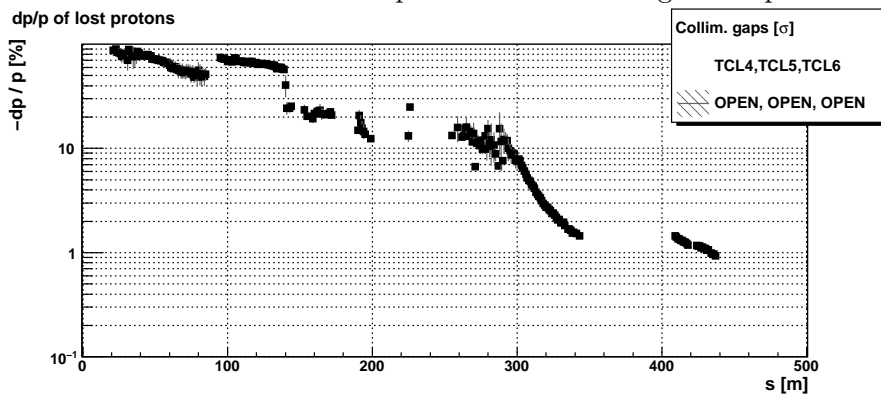


Figure 7.7: Average momentum offset with respect to 7 TeV of the protons lost according to the distribution of Fig. 7.6

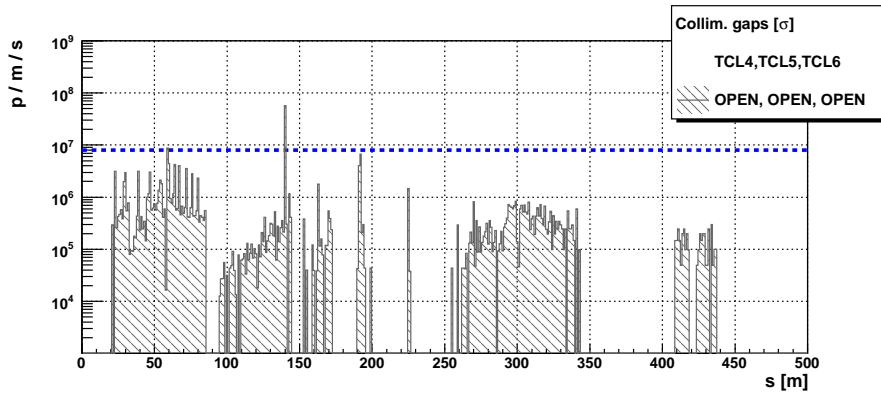


Figure 7.8: PTC loss maps with no TCL collimators installed in the IR1 straight section, scaled to the factor p/p_0 where p is the lost protons momentum and $p_0=7$ TeV. The horizontal blue line indicate the estimated quench limit assuming 7 TeV protons.

1520 that the deposited energy in the triplets can reach the level of 10 Watts per meter.

1521 **7.5.2 PTC loss maps with single collimators**

1522 The loss maps produced with PTC for different settings of the TCL4 collimator, while maintain-
1523 ing all other collimators wide open, are shown in Fig. 7.10 for all the region on the right side of
1524 ATLAS. The plots indicate that TCL4 at $30\sigma_x$ (blue line) is sufficient to protect all magnets (Q4
1525 included) in the region from 150 m to 180 m from the interaction point. For the same settings
1526 the losses on the Q5 magnet are reduced by a factor of 10. On the other hand, even an extreme
1527 closure of TCL4 (e.g. red line in the figure) only partially reduces the integrated losses from
1528 250 m downstream.

1529 The loss maps produced with PTC for different settings of the TCL5 collimator, while main-
1530 taining all other collimator wide open, are shown in Fig. 7.11. In this case, the plots indicate
1531 that TCL5 at $50\sigma_x$ (yellow line) is sufficient to protect all magnets (Q5 and Q6 included) in
1532 the region from 190 m to 250 m from the interaction point. For the same settings the integrated
1533 losses in the region from 250 m to 350 m are slightly reduced, whereas the peak losses remain, as
1534 without collimators (black line), one order of magnitude below the estimated quench limit. In
1535 this second region, even when the TCL5 collimator is closed to $10\sigma_x$ (red line), the peak losses
1536 remain unchanged even though the integrated losses are reduced by about a factor of 5.

1537
1538 It is very relevant to notice that neither TCL4 or TCL5 have any effect on the losses after
1539 350 m from the IP, even when closed to $10\sigma_x$.

1540 **7.5.3 PTC loss maps with different collimator schemes**

1541 This section discusses two possible collimation schemes that, according to the simulations, guar-
1542 antee the same LHC protection as with the existing scheme and allow enough forward proton
1543 acceptance at the AFP detectors proposed at 220 m. Both proposals envisage the presence of a
1544 collimator (TCL6) at about 230 m, in front of the Q6 quadrupole.

1545 The first alternative implies the displacement of the TCL5 collimator from the slot just
1546 upstream of Q5 to the one upstream of Q6. The loss maps produced with PTC with both TCL4
1547 and a new TCL6 at $30\sigma_x$ is shown in Fig. 7.12 (green line) and compared to the situation without
1548 collimators (black) and with a possible configuration of the present scheme (red, TCL4 at $30\sigma_x$
1549 and TCL5 at $15\sigma_x$). This alternative configuration results in the reduction of a factor 10 (w.r.t.
1550 the case of no collimators) of the peak losses on Q5 and reduces by a factor of 3 (w.r.t. the
1551 existing solution) the integrated losses in the region from 250 m to 350 m. This solution would
1552 not require the production of a new collimator.

1553 The second alternative implies the fabrication of a new collimator and its installation in front
1554 of Q6, while leaving in place the TCL5 collimator. The loss maps produced with PTC while
1555 setting TCL4 at $30\sigma_x$, TCL5 at $50\sigma_x$ and a new TCL6 at $40\sigma_x$ is shown in Fig. 7.13 (green line)
1556 and compared to the situation without collimators (black) and to the first alternative presented
1557 above (red). This second alternative would guarantee a full cleaning of the losses in the Q5
1558 region, while reducing by a factor of about 2 (w.r.t. the existing solution, red line in Fig. 7.12),
1559 the integrated losses in the region from 250 m to 350 m.

1560 As discussed later in the note, both alternatives would allow enough forward proton accep-
1561 tance at the AFP detectors proposed at 220 m.

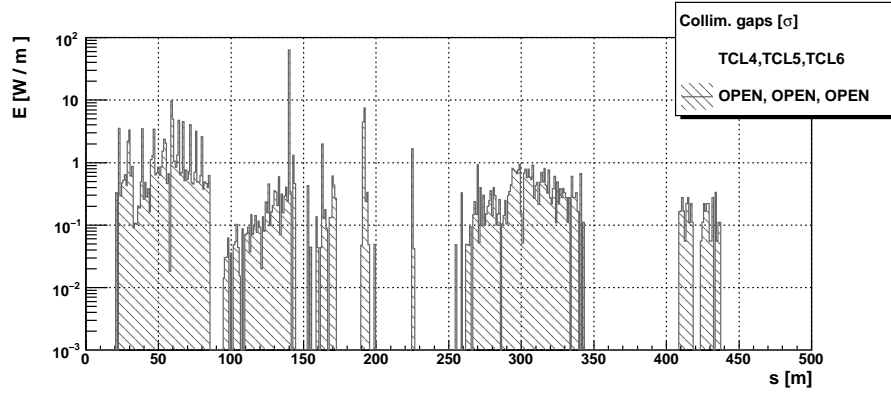


Figure 7.9: Energy deposition corresponding to the loss map shown in Fig. 7.6. Hence, it should be better if p/p_0 is considered (see Fig. 7.8).

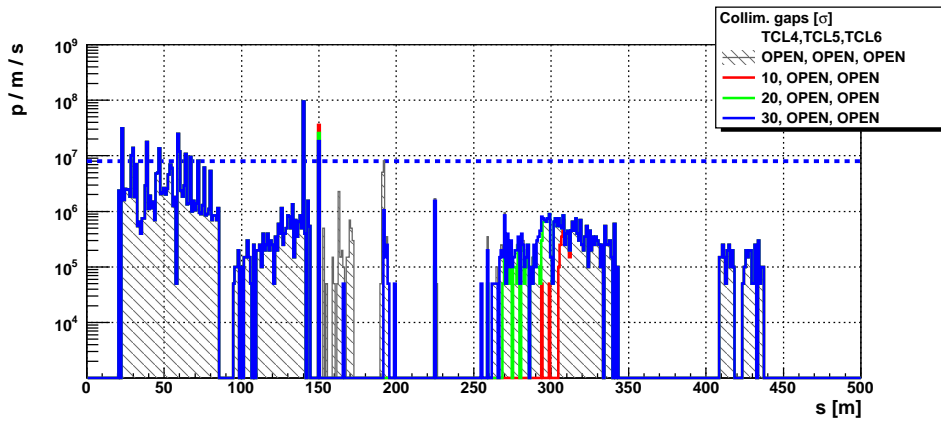


Figure 7.10: PTC loss maps with different settings of the TCL4 collimator installed at about 140 m from IP1. The horizontal blue line indicate the estimated quench limit assuming 7 TeV protons.

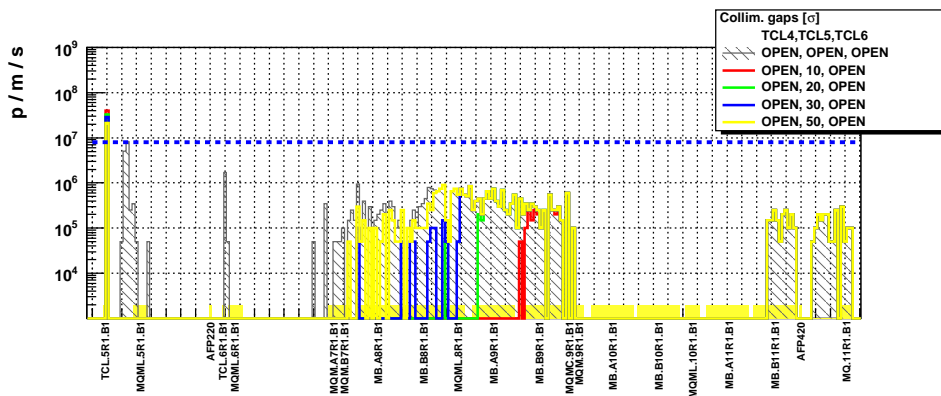


Figure 7.11: PTC loss maps with different settings of the TCL5 collimator installed at about 190 m from IP1. The horizontal blue line indicate the estimated quench limit assuming 7 TeV protons.

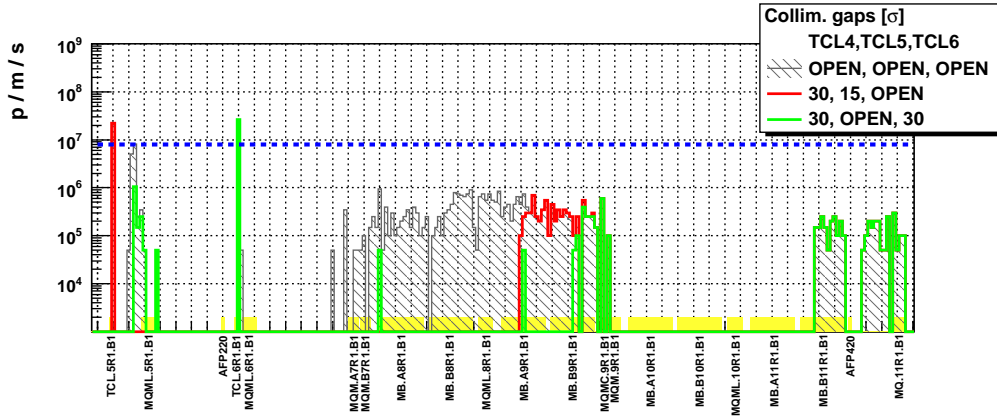


Figure 7.12: Comparison between loss maps with the presently foreseen collimation scheme (red) and a first alternative scheme (green) implying the displacement of TCL5 in front of Q6.

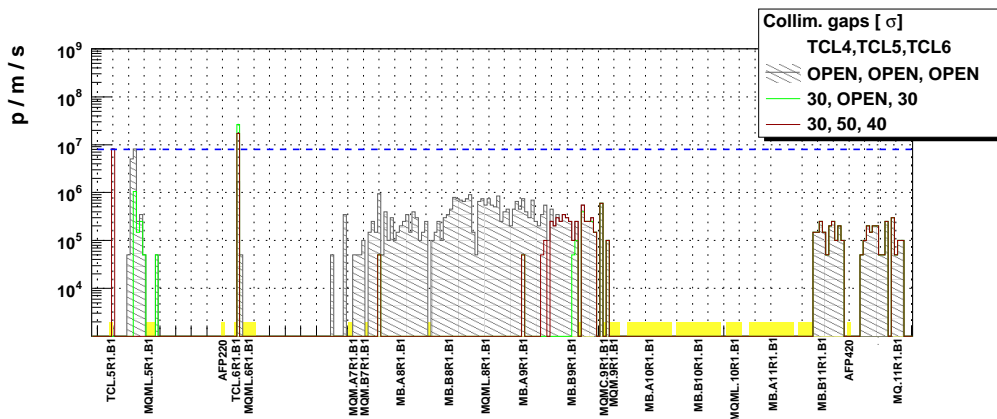


Figure 7.13: Comparison between loss maps with a second alternative scheme (green) implying the installation of a new collimator in front of Q6 and the first alternative presented in Fig. 7.12.

1562

7.6 Conclusion

1563

1564

1565

1566

1567

1568

1569

1570

1571

1572

1573

1574

1575

1576

The analytical calculations and tracking simulations presented in this note provide two alternative collimation schemes to the one presently foreseen in the ATLAS (and CMS) straight section regions. According to these studies, the two alternatives would guarantee the LHC protection from physics debris and enough acceptance for the detectors proposed at 220 meters from the IP. Both alternatives imply the installation of a collimator between the Q5 and Q6 magnets, as close as possible to Q6. This looks possible after studying the present LHC layout and a visual inspection in the tunnel. However, a detailed study of the collimator integration is necessary for validating the proposal.

The overall study interpretation depends on the estimated quench limit for the superconducting elements and the early LHC runs will give information about the accuracy of such estimation.

Even though the studies considered a perfectly linear model of the LHC optics, the relative comparison among loss maps produced with different collimation schemes is considered accurate. Indeed, the numerical simulations reproduced nicely the results of Baichev-Jeanneret performed

1577 with a different tracking code and p-p generator. In addition, the two independent codes PTC
1578 and SIXTRACK exhibited very consistent results when using the same LHC model in terms of
1579 optics and aperture.

1580

1581 The absolute simulation accuracy can be improved by considering magnetic field errors mea-
1582 sured in the laboratory and magnet elements misalignment measured in the LHC tunnel. The
1583 results could also be improved by using the accelerator optics as measured during the early LHC
1584 runs.

1585

1586 A complete estimation of the effect of the physics debris on the LHC elements can be achieved
1587 by modeling the electromagnetic and hadronic showers resulting from the scattering of the of
1588 the proton on the TCL. This can be done with Monte Carlo codes such as Geant4 and FLUKA,
1589 with the showers initiated from the PTC loss maps in the collimators.

Chapter 8

Appendix II: LHC Optics, Acceptance, and Resolution

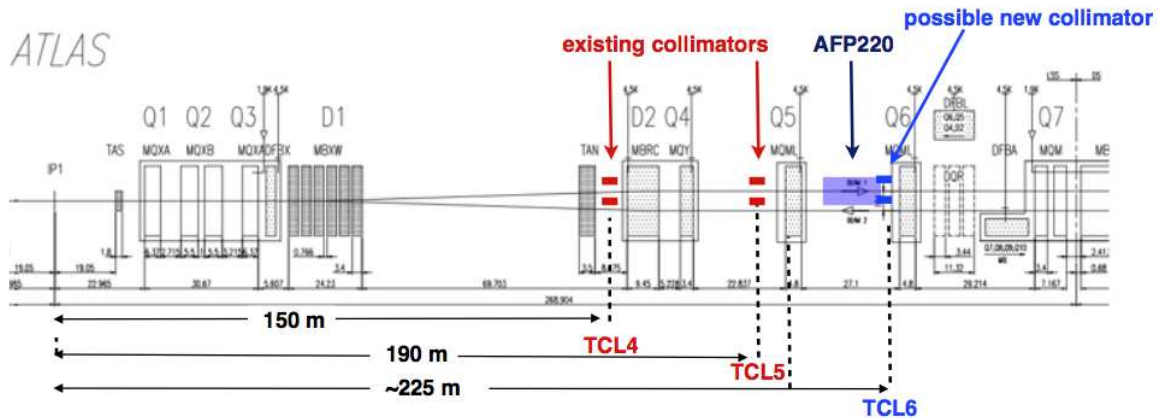


Figure 8.1: schematic view of the beamline at IP1.

8.1 Beamline

The configuration of the LHC beamline around the interaction points is shown schematically in Figure 8.1. The proposed forward detector stations are to be installed in the regions located at approximately 220 m from the IP1 interaction point in both beamlines downstream of the central detector. A similar installation is planned for the IP5 region. Protons that have lost energy in the primary interaction are not focussed to travel long distances around the beamline and emerge laterally after passing through bending magnets. At 220m we can observe protons that have lost typically 100 GeV or more in the primary interaction. The acceptance and the ultimately achievable energy resolution of the forward detectors depends on the LHC beam optics and on the position of the detectors relative to the beam.

The AFP Collaboration has written a tracking program, FPTrack [58], which has been incorporated into the ATHENA package. It tracks protons (or other particles) that emerge in a forward direction from the interaction region, and tracks them through the system of magnets and collimators that form the beamline, in either direction. FPTrack is much easier and faster to use in this context than the MAD-X program, the standard beam transport program used at

1608 CERN, and detailed comparisons have been carried out to ensure that the two programs give
1609 results that are in agreement. A model of the LHC beamline optics is implemented, and it can
1610 be updated when new beam optics configurations are announced. The CMS collaboration also
1611 have their own tracking program and, again, checks have been made that the programs are all
1612 equivalent. All calculations presented here are in terms of the planned 7000 GeV beamline.

1613 The tracking operates by applying thick-magnet bending using a full momentum-dependent
1614 formula at each beamline element. This is essential owing to the non-linearities in the system
1615 when off-axis and off-momentum particles are being tracked. Collimators are taken into account,
1616 as are the apertures of the beamline elements. Two collimator conditions are considered, “open”,
1617 in which the collimators TCL.4, TCL.5 and TCL.6 are opened, and “closed”, in which they are
1618 set at positions that have been calculated to protect the beam elements with minimal obstruction
1619 to the beam. In this context the configuration “30,50,40” described in Appendix I has been used.

1620 It should be noted that the beamline contains dipole and quadrupole magnets only, with
1621 no sextupoles. Therefore the horizontal and vertical bending and focussing of the protons are
1622 independent of each other. All the most important properties of the beamline of relevance here
1623 depend only on the horizontal behaviour of the beam apart from aperture effects, which are
1624 fully taken into account in both dimensions.

1625 Unless otherwise stated, we use the ExHuME or FPMC Monte Carlo [59] to generate outgoing
1626 protons from the central exclusive production of a SM Higgs Boson, although the results will
1627 apply for any double-diffractively produced system. Version 6.503 of the LHC optics files have
1628 been used with: $\beta^* = 0.55$ m; angular divergence at the IP $\sigma_\theta = 30.2 \mu\text{rad}$; crossing angle =
1629 $142.5 \mu\text{rad}$ in the vertical (horizontal) plane at IP1 (IP5); beam energy spread $\sigma_E = 0.77$ GeV.
1630 The energy spread of the 7000 GeV beam is taken into account and is an irreducible limiting
1631 factor on the mass resolution obtainable by proton tagging detectors at the LHC

1632 8.2 Detector Acceptance

1633 The position and direction of a proton as it hits the 220 m detectors (for a given LHC optics)
1634 depend on the energy E and scattering angle θ of the proton as it emerges from the primary
1635 interaction, and on the z -vertex position where this occurs, although the latter has a relatively
1636 weak effect. The variables E and θ are directly related to ξ , the fractional longitudinal momen-
1637 tum loss of the outgoing proton, and $-t$, the square of the four-momentum transfer. Figure 8.2
1638 shows the acceptance in the ξ - t plane for the 220 m regions for beam 1 and beam 2 respectively,
1639 around IP1. The acceptance is averaged over the azimuthal angle of the emerging proton, and
1640 hence can take intermediate values in the range (0., 1.).

1641 The acceptance is affected by the collimator settings used. To illustrate this, the figures
1642 shows acceptances with the collimators referred to above open and closed. Unless mentioned, all
1643 quantities in the present section refer to calculations made with the closed-collimator configura-
1644 tion. There are regions of parameter space where the acceptance, averaged over the azimuthal
1645 angle of the proton, is excellent, and these are not greatly impacted by the necessary use of the
1646 collimators.

1647 Figure 8.3 shows the proton distributions in the horizontal coordinate x at 220 m from
1648 the interaction point. The distribution is averaged over the proton momentum distribution
1649 and depends on the type of physics process that is generating the protons. There are differences
1650 between the two beamlines which it is necessary to keep under scrutiny. The upper distributions
1651 are obtained as an average over a range of masses of a centrally double-diffractively produced
1652 object, between 180 and 1440 GeV. The lower distributions are obtained from a model of the
1653 main diffractive processes that are expected to occur in proton-proton interactions at 7000+7000

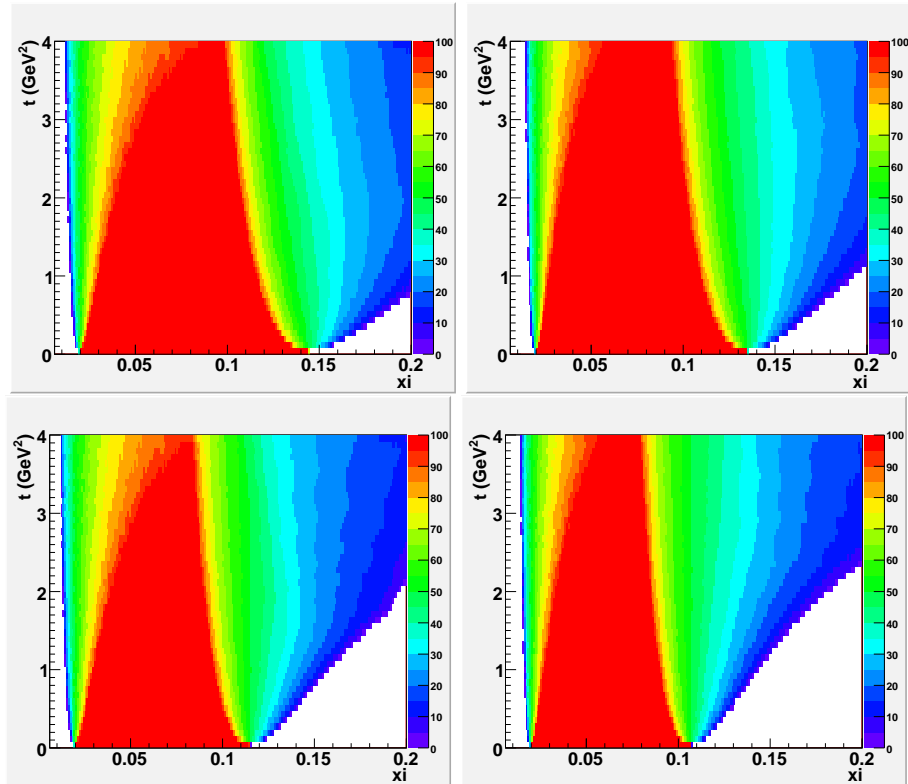


Figure 8.2: Acceptance in the ξ , t plane for protons to reach planes at 220 m in beam 1 (left) and beam 2 (right) around IP1, where ξ is the fractional energy loss of the proton. The variable plotted as t is the modulus of the squared momentum transfer to the proton at the IP and ξ its fractional energy loss; no detector effects are included here. Upper (lower) plots: collimators open (closed).

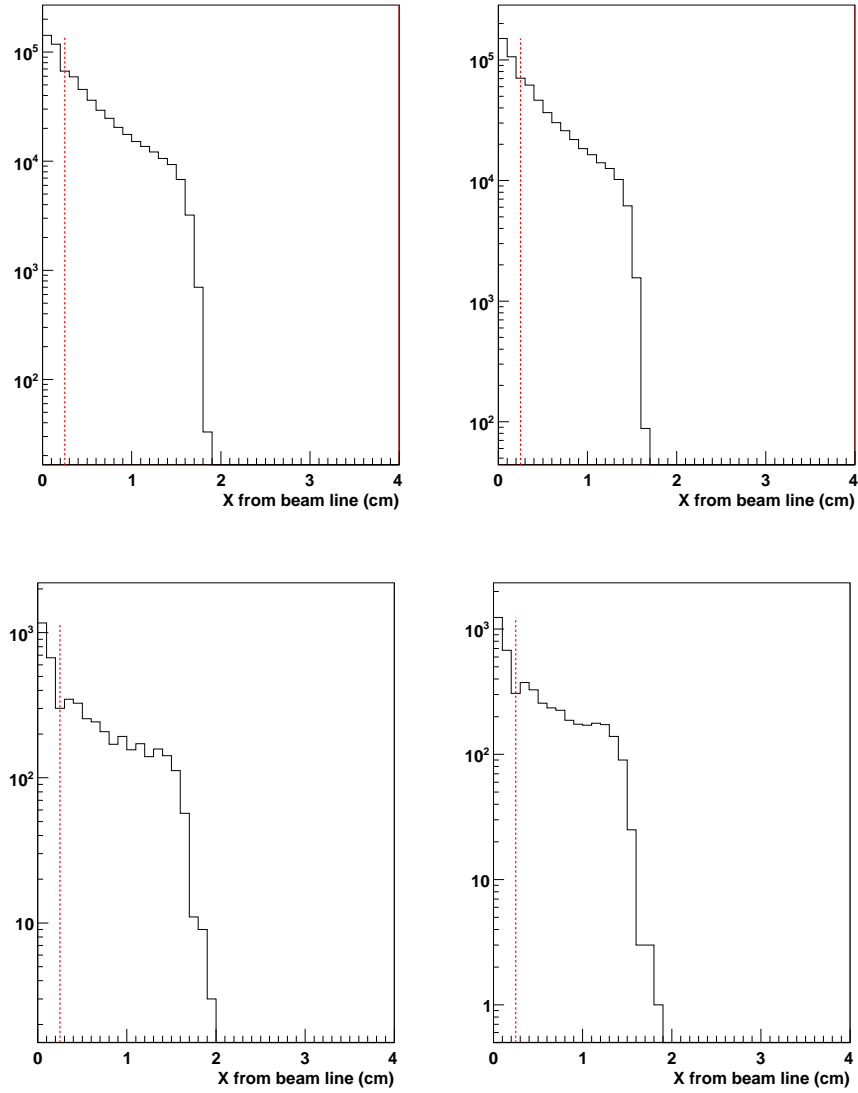


Figure 8.3: Distributions in x for protons at the plane at 220 m in beam 1 (left) and beam 2 (right) around IP1. The distributions are for single protons arising from the central exclusive production of an object with mass averaged over the mass range 180 to 1440 GeV (upper). The lower plots are for protons produced in association with diffractive production.

1654 GeV. These are of physics interest in their own right, but will form a background to any processes
1655 of a rarer nature.

1656 In order to understand the issues that determine the design of the silicon detector systems,
1657 a further set of plots (fig 8.4) shows the x distributions obtained from protons originating from
1658 centrally produced objects generated over a selection of masses. The general feature is that at
1659 lower masses the protons emerge closer to the beamline, with broader distributions developing
1660 as the mass increases. In the plots shown in this figure, a pair of protons in coincidence is not
1661 demanded, and just the single protons are plotted, since the probability of a coincidence is
1662 small at masses below about 400 GeV. In fig. 8.5, proton distributions are shown at higher
1663 masses with the requirement that a proton is detected in both silicon detector systems. Fig. 8.6
1664 shows the proton hit distributions for different region in diffractive mass.

1665 Fig. 8.7 shows the acceptance of the system for detecting a proton in the 220m systems
1666 in both beamlines in coincidence, as a function of the mass of a double-diffractively produced
1667 central object X . It varies substantially with the distance of the silicon detectors from the beam,
1668 which for convenience is taken here to be the same in both beamlines, although in practice this
1669 is not a necessary constraint. As the distance increases, the lower end of the range of accepted
1670 masses increases, but the upper end is not affected. The acceptances shown are calculated with
1671 our best available model of the collimator settings that could be used.

1672 The position of the silicon detectors that we can use will be determined in close collaboration
1673 with the accelerator experts, and will need to allow for an inevitable “dead region” occupied by
1674 the wall of the movable beam pipe and the edge of the silicon detectors. The permitted distance
1675 between the beam and the closest physical material is normally assumed to be 10 times the
1676 Gaussian width “sigma” of the beam, where sigma at 220m is 0.09 mm horizontally according
1677 to the currently assumed optics. We show results for the separation between the beam and the
1678 active silicon detection region having an “optimistic” value of 2 mm, a “realistic” value of 2.5
1679 mm and a “pessimistic” value of 3 mm.

1680 8.3 Momentum determination

1681 The mapping of the energy loss and outgoing angle of a proton at the interaction point on to
1682 a position and angular measurement in the detector at 220 m or 420 m can be visualized using
1683 chromaticity plots. Figure 8.8 shows iso-energy and iso-angle curves for protons with energy
1684 loss ranging from 0 to 1000 GeV in steps of 100 GeV at 220 m, evaluated at points in the
1685 range $\pm 250 \mu\text{rad}$ in steps of $10 \mu\text{rad}$. If the protons were bent out of the beamline in a simple
1686 manner, the isoenergetic sets of points would be vertical, corresponding to a fixed value of x for
1687 a given proton momentum. However the non-linear nature of the beam optics, involving energy
1688 dependence of the transfer matrices, produces chromaticity plots that are very different from
1689 such a situation.

1690 The chromaticity plots show that the measurement of the energy of the outgoing proton
1691 requires good measurements of both position and angle in the detector stations. Thus, at low
1692 momentum losses ξ an excellent position measurement is required, whereas the measurement of
1693 higher momentum losses becomes increasingly determined by the angular measurement. Hence
1694 we shall require detector stations distributed suitably along the space available to us at 220m.

1695 Polynomial-based parametrization formulae have been developed in order to evaluate the
1696 proton momenta from the measured parameters in the silicon detectors. The formulae are based
1697 on fits to the calculated positions and angles, using the generated values of the momentum and
1698 emission angle at the IP, and averaging over the width of the beam-beam interaction region.
1699 Further development in this area is in hand, using the ALFA code to unfold the initial parameters

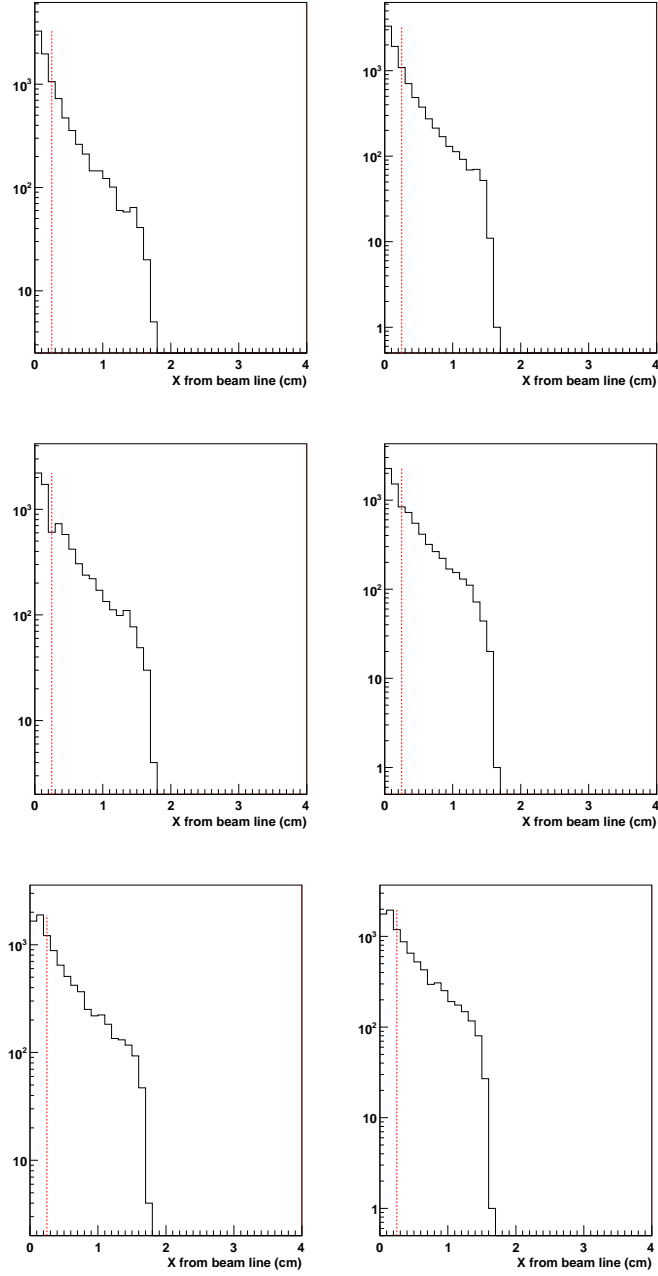


Figure 8.4: Distributions in x for protons at the plane at 220 m in beam 1 (left) and beam 2 (right) around IP1. The distributions are for single protons arising from the central exclusive production of an object with mass 180 GeV (upper), 240 GeV (centre), 360 GeV (lower).

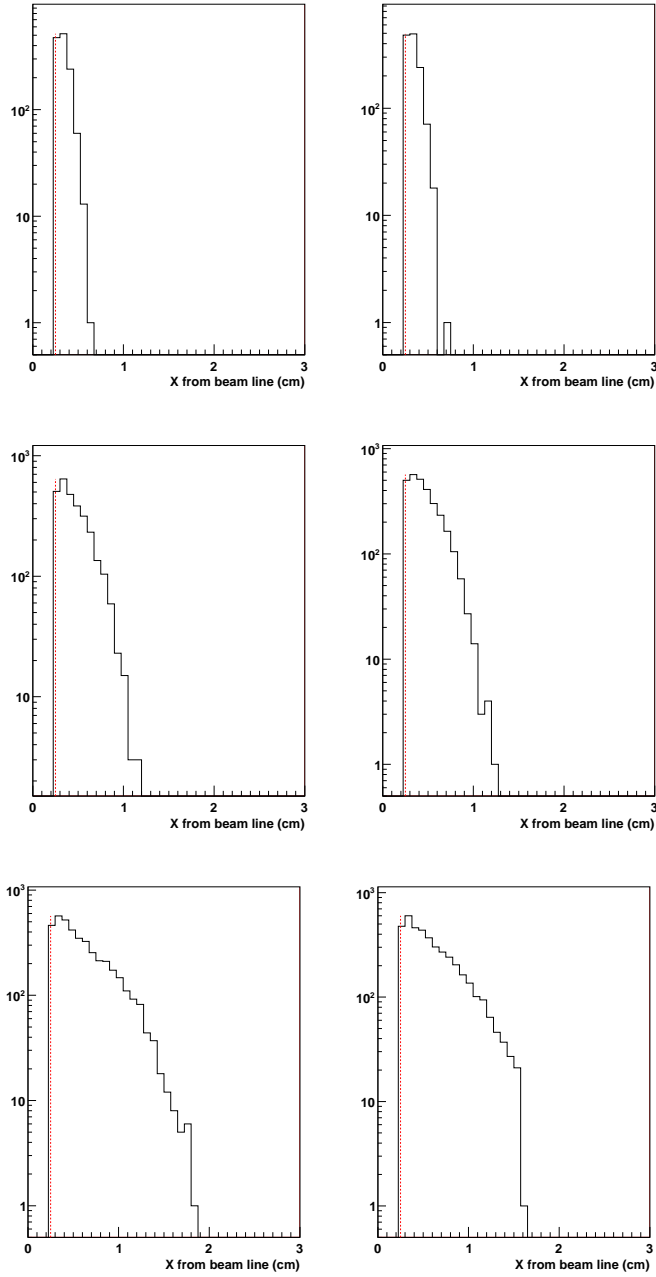


Figure 8.5: Distributions in x for protons at the plane at 220 m in beam 1 (left) and beam 2 (right) around IP1. The distributions are for protons from the central exclusive production of an object with mass 360 GeV (upper), 480 GeV (centre), 600 GeV (lower). Both protons are required to emerge at a distance of at least 2mm from the beam.

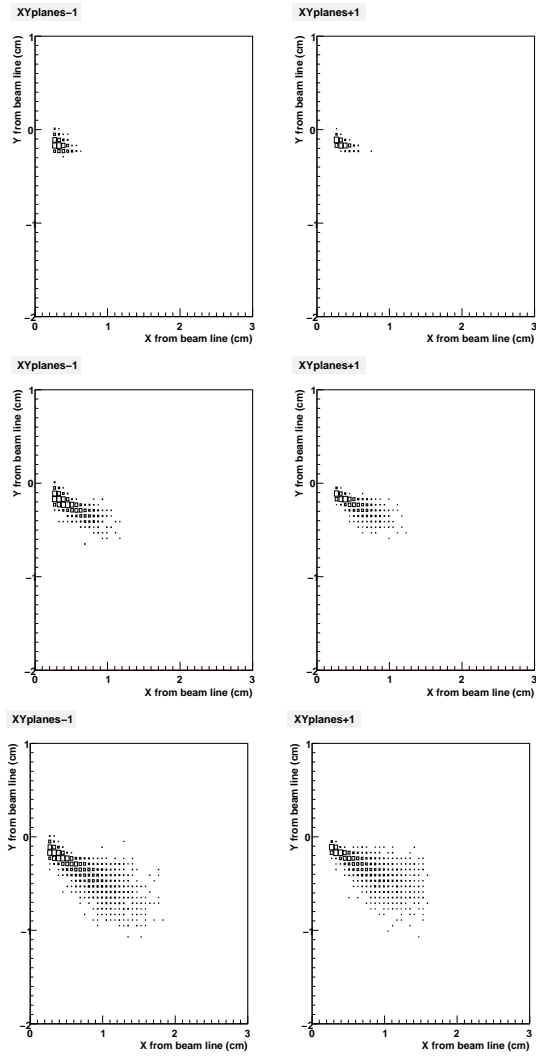


Figure 8.6: Distributions in x, y for protons at the plane at 220 m in beam 1 (left) and beam 2 (right) around IP1. The plots are for objects with mass 360, 480 and 600 GeV (first, second and third lines) when both protons are detected.

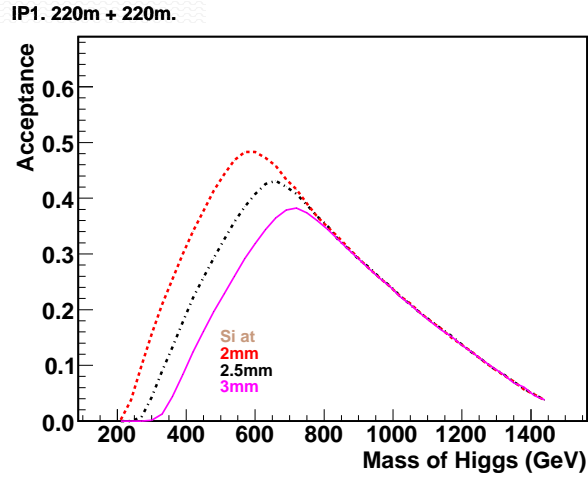


Figure 8.7: Acceptance as a function of centrally produced mass for 220 + 220 m proton tags for the edge of the silicon detector active region located at different distances from the beam. The collimators are closed.

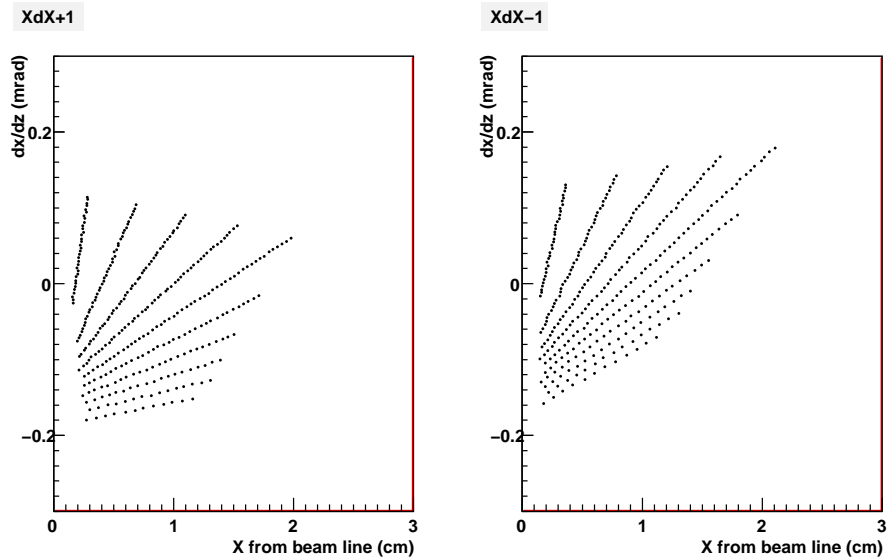


Figure 8.8: Chromaticity distributions for the 220m detectors in beam 1 (left) and beam 2(right). The radially distributed sets of points are for protons at energies of 6900 GeV, 6800 GeV, etc, starting at the left of each plot and reading clockwise. Within each set, the points denote protons emerging from the primary interaction at intervals of $10 \mu\text{rad}$ in the horizontal plane.

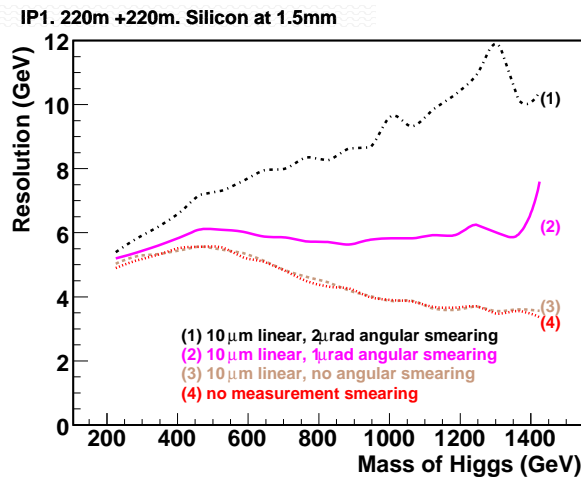
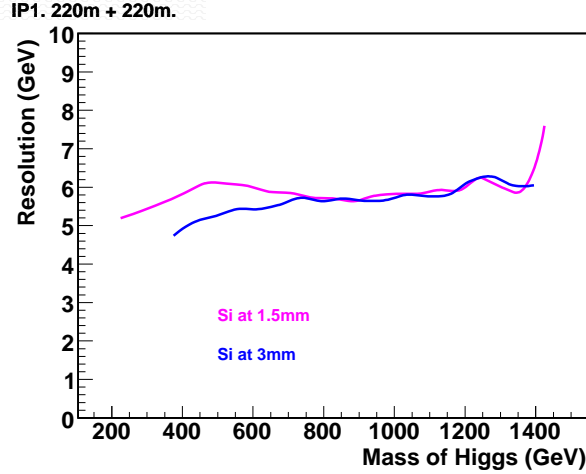


Figure 8.9: Reconstructed mass resolution for production of central objects of various masses. First plot: applying nominal measurement resolution and experimental smearings, the resolution for two different values of the silicon distance from the beam is compared. Second plot: effect of various values of measurement resolution on the mass resolution. The fluctuations on the curves are of a statistical origin.

1700 of the forward proton given the final measured parameters.[60]

1701 8.4 Mass measurement

1702 From the momenta of the pair of oppositely emerging protons in an event, the mass of the
 1703 centrally produced system can be calculated by a missing-mass formula [61]. The mass resolution
 1704 was evaluated by a Gaussian fit to the difference of the calculated and input masses. Minimizing
 1705 this resolution is important for the physics capabilities of the proposed new detectors. For present
 1706 purposes, we consider protons whose event vertex is at the nominal position of the interaction
 1707 point. Effects of variations of the x and z are easily included, and we find that they are not
 1708 large. It is to be noted that the vertex position is well-measured by the central detector for
 1709 every event, and the average value of x and z for a given run will also be well-measured; both
 1710 quantities are expected to be quite stable within a run. Thus offline corrections

1711 for the mean variations and event-by-event are easily applied.

1712 The following factors affect the measured mass resolution of a narrow object produced in
1713 the exclusive double diffraction process:

- 1714 • The Gaussian width of the momentum distribution of the circulating proton beam. This
1715 is specified as 0.77 GeV.
- 1716 • The lateral uncertainty of the position of the interaction point. This is taken to be 11.8 μm
1717 from the intrinsic beam width, but can be improved if the central silicon detector system
1718 provides a better measurement on an event-by-event basis.
- 1719 • The angular spread of the interacting beams, corresponding to a lateral momentum smear-
1720 ing of 0.21 GeV on the outgoing proton.
- 1721 • The position measurement uncertainty in the detector system
- 1722 • The angular measurement uncertainty in the detector system.

1723 Figure 8.9 shows the affect of the above factors on the mass resolution. We first confirm that
1724 the resolution is not greatly dependent on the distance of the silicon detectors from the beam,
1725 provided that the acceptance is present, by fixing the smearing conditions at some standard
1726 values (Item (2) below). We then examine the effects of fixing the silicon distance at a minimum
1727 value of 1.5 mm, and varying the smearing that is applied (lower plot):

- 1728 • (1) Applying 10 μm linear and 2 μrad angular smearing on the x measurement of the
1729 proton at 220m.
- 1730 • (2) As (1), but with the angular smearing reduced to 1 μrad .
- 1731 • (3) As (1) but with no angular smearing
- 1732 • (4) With no measurement smearings, but including all the intrinsic smearings.

1733 It can be seen that an accurate angular measurement is critical, but to achieve a reasonable value
1734 of $\pm 1\mu\text{rad}$ in this quantity, we must measure the positions to high precision. As the momentum
1735 loss ξ of the protons emerging from the primary interaction increases, the missing mass increases
1736 but the momentum measurement becomes increasingly dependent on the angular measurement,
1737 as noted in discussing the chromaticity plots.

1738 It is possible to measure the transverse momentum of the proton as it emerges from the
1739 interaction point, again by means of polynomial-based parametrization formulae using the mea-
1740 surements in the detector stations. Both x and y measurements are required to determine the
1741 full transverse momentum of the proton. The measurement is degraded by two factors. The
1742 angular beam spread at the interaction points is equivalent to a ± 0.21 GeV transverse mo-
1743 mentum spread, both horizontally and vertically, and the poorer measurement uncertainty in
1744 the y direction increases the overall uncertainty on p_T significantly. Studies are continuing to
1745 determine the requirements for particular physics studies and whether they can be achieved.

1746 8.5 Calibration

1747 Consistent alignment of the silicon system relative to the magnets, the beamline and the exper-
1748 imental hall can be achieved by means of beam position monitors, as discussed in the relevant
1749 section of this proposal. However to take account of any unknown or unforeseen effects, it is

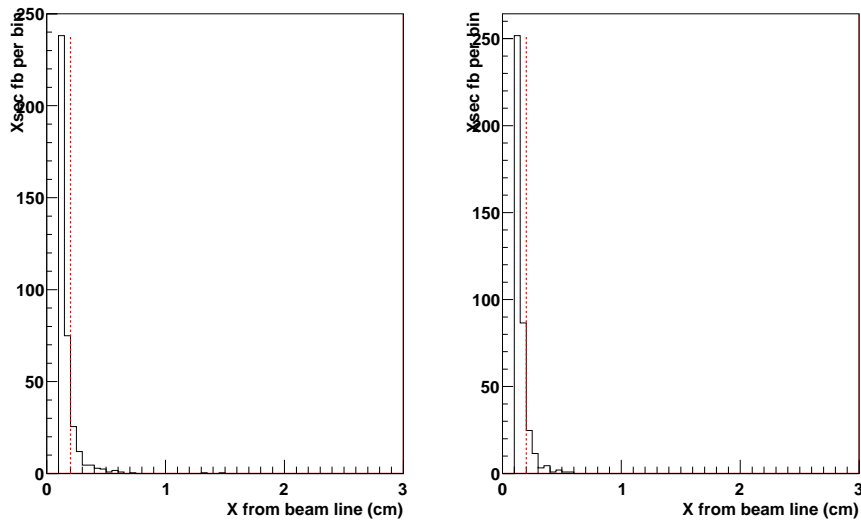


Figure 8.10: Cross section for detecting a forward proton accompanying a muon pair produced by the photon-photon process in the central detector within a rapidity range of ± 2.5 . Left, beam 1; right; beam 2; upper, muon $p_T > 6$ GeV. The plotted cross sections are fb per bin in x measured in the silicon planes.

1750 necessary to calibrate the momentum measurement of the protons. This can be done by means
 1751 of the production of lepton pairs, of which muon pairs give best precision, in the central ATLAS
 1752 detector. Triggers exist that should be able to record events in which a muon pair is produced
 1753 by the photon-photon process where the photons radiate off the protons. At present, we foresee
 1754 a trigger on muon pairs where each muon has transverse momentum of at least 6 GeV, however
 1755 a lower value could be helpful.

1756 The accurately measured momenta of the muons allow the momenta of the forward protons
 1757 to be accurately evaluated. If either of the latter is measured in the respective forward system,
 1758 its measured momentum can be compared with the value obtained from the muon pairs, and
 1759 with sufficient statistics a calibration can be achieved. It is not necessary to record both of the
 1760 forward protons that emerge in any given event.

1761 Using the LPAIR program to generate muon pairs produced within an overall rapidity range
 1762 of ± 2.5 , we have estimated the rates of calibration events that can be obtained in this way. They
 1763 are shown in fig. 8.10 and their values should allow a suitable calibration to be made over
 1764 a period of time: to calibrate a shift of the mean momentum of one-seventh of its measured
 1765 resolution, 50 events would be required, since the backgrounds will be small. With the silicon
 1766 distance from the beam at 2.0, 2.5, 3.0 mm, the integrated cross section for each beamline is 43,
 1767 19, 7.5 fb, respectively, so that integrated luminosities of 1.1, 2.6 and 6.6 fb^{-1} will be required
 1768 to make a calibration. Obviously the situation is assisted if the detectors can be moved as close
 1769 as possible to the beam, which is desirable anyway.

1770 Another possible calibration method that we are considering is to use the bremsstrahlung
 1771 photons recorded in the ZDC. The energy of such a photon has been lost by the forward proton,
 1772 whose energy is thereby calibrated. There are serious backgrounds in this method, however, and
 1773 it is harder to implement than the muon-pair method, although the cross section is very much
 1774 higher. Also, the ZDC may be removed, according to current plans; further study is required.

1775 **8.6 Summary**

1776 The beam optics at LHC allows protons that have lost momentum in a diffractive interaction
1777 to emerge from the beam envelope at regions 220 m from the interaction point. By placing
1778 silicon detector arrays in these locations we can detect the protons and obtain good acceptance
1779 for diffractively produced objects with a wide range of masses above 180 GeV, the precise
1780 acceptances depending on how close it is possible to place the detectors relative to the beam.
1781 The expected position and angle resolutions for the protons obtained in the silicon stations are
1782 expected to yield mass resolutions of around 6 GeV from the proton pair alone.

Chapter 9

Appendix III: A possible extension of the AFP project using 420 m detectors

In order to detect centrally produced objects in the mass range ~ 120 GeV it will be necessary to install proton tagging detectors in the cold region of the LHC 420m from the ATLAS IP. The FP420 Collaboration commissioned the CERN design office, working with the TS/MME group to design a cost effective and safe replacement for the 420m connection cryostat. The main design parameters were to provide warm beam pipes and sufficient space to install moveable silicon tracking and fast timing detectors with little or no disruption to the LHC itself. In this chapter, we describe the new connection cryostat design, as well as the physics motivations of such an extension of our proposal.

9.1 Physics program in 220+420 stage

With the 420 m extension of the forward proton detecting system, much broader spectrum of physics applications will be reached. A detailed complete description is given in [24]. Here we summarize those topics that were not possible with the 220 m detectors only. As a rule of thumb, the acceptance in ξ for detectors at 220+420 m corresponds to $0.0015 < \xi < 0.1$ and is dominated by very low t .

9.2 Central Exclusive Production

There are three important reasons why CEP is especially attractive for studies of new particles. Firstly, if the outgoing protons remain intact and scatter through small angles then, to a very good approximation, the primary active di-gluon system obeys a $J_z = 0$, C-even, P-even, selection rule [7]. Here J_z is the projection of the total angular momentum along the proton beam axis. This selection rule readily permits a clean determination of the quantum numbers of any new resonance. Secondly, because the process is exclusive, the energy loss of the outgoing protons is directly related to the invariant mass of the central system, allowing an excellent mass measurement irrespective of the decay mode of the central system [61]. Even final states containing jets and/or one or more neutrinos are measured with $\sigma_M \sim 2$ GeV/ c^2 . Thirdly, in many topical cases and in particular for Higgs boson production, a signal-to-background ratio of order 1 or better is achievable. This ratio becomes significantly larger for Higgs bosons in certain

1813 regions of MSSM parameter space [62]. The CEP cross sections in the following discussion are
 1814 calculated using the KMR model [7].

1815 9.2.1 $h \rightarrow b\bar{b}$

1816 As an example of what may be possible with ATLAS FP, we briefly review a detailed analysis
 1817 carried out in [62] of the $h \rightarrow b\bar{b}$ channel in a specific MSSM scenario. The MSSM point chosen
 1818 for this analysis is $m_A = 120$ GeV and $\tan\beta=40$. The lightest Higgs boson, h , has a mass
 1819 of 119.5 GeV and the cross section \times branching ratio is approximately 20 fb. ATLAS FP is
 1820 particularly well suited to observing the Higgs sector in certain regions of MSSM parameter
 1821 space; at high $\tan\beta$ the CEP cross sections are in general enhanced with respect to the Standard
 1822 Model and the branching ratio to $b\bar{b}$ can be as high as 90% if the light SUSY decay channels
 1823 are not allowed. Furthermore, the $J_z = 0$ selection rule suppresses the irreducible $b\bar{b}$ continuum
 1824 background significantly, thus enhancing the signal to background ratio with respect to standard
 1825 search channels. Finally, because the pseudo-scalar A cannot be produced in CEP, ATLAS
 1826 FP will provide a clean measurement of the mass and quantum numbers of h and H even
 1827 when m_A is close to m_h or m_H , which can occur at high $\tan\beta$. CEP can therefore provide
 1828 complementary information about the Higgs bosons if the MSSM is realised in nature and could
 1829 allow a measurement of the $Hb\bar{b}$ coupling, which may be difficult in other production channels.

1830 The challenge is controlling the overlap (or pile-up) background at high luminosity. The
 1831 primary overlap background consists of a three-fold coincidence in one bunch crossing between
 1832 an event producing a hard scatter, with the signature of interest detected in ATLAS, and two
 1833 single diffractive events that produce forward protons within the acceptance of the forward
 1834 detectors. The overlap background is most problematic for dijet final states because there is
 1835 a large cross section for non-diffractive dijet production at the LHC. For example, the overlap
 1836 background to $h \rightarrow b\bar{b}$ is estimated to be a factor of 10^5 (10^7) larger than the signal for a
 1837 luminosity of 10^{33} (10^{34}) $\text{cm}^{-2} \text{s}^{-1}$.

1838 There are several techniques that can be employed to reject the overlap background: (i)
 1839 vertex matching using the di-jet vertex and fast-timing detectors, (ii) topological requirements,
 1840 (iii) kinematic matching between the di-jet system and central system measured by the forward
 1841 detectors and (iv) charged track veto which discriminates against the much larger track multi-
 1842 plicity in non-diffractive events due to multiple parton-parton interactions. The result is that
 1843 the overlap background in the $h \rightarrow b\bar{b}$ channel is negligible up to $\sim 2 \times 10^{33} \text{ cm}^{-2} \text{s}^{-1}$ and smaller
 1844 than the other backgrounds up to $\sim 5 \times 10^{33} \text{ cm}^{-2} \text{s}^{-1}$. At instantaneous luminosities up to
 1845 $10^{34} \text{ cm}^{-2} \text{s}^{-1}$ it becomes desirable to upgrade the fast timing system to a resolution of 5 to 10
 1846 ps.

1847 Figure 9.1 (a) shows the expected mass distribution for protons tagged at 420 m for this
 1848 parameter choice given 60 fb^{-1} of data collected at $2 \times 10^{33} \text{ cm}^{-2} \text{s}^{-1}$. The significance is
 1849 3.5σ . Figure 9.1 (b) shows the same distribution but for 300 fb^{-1} of data collected equally at
 1850 $7.5 \times 10^{33} \text{ cm}^{-2} \text{s}^{-1}$ and $10^{34} \text{ cm}^{-2} \text{s}^{-1}$ and assuming improved timing rejection. The significance
 1851 increases to 4.5σ .

1852 A detailed study of the coverage in the $M_A - \tan\beta$ plane afforded by forward proton detectors
 1853 at 420m and 220m from the interaction point was carried out in [62] for several benchmark MSSM
 1854 scenarios. Figure 9.2 shows the 3σ contours for $h \rightarrow b\bar{b}$ observation (upper plot) and $H \rightarrow b\bar{b}$
 1855 observation (lower plot). Curves are shown for 60 fb^{-1} and 600 fb^{-1} . The 60 fb^{-1} scenario
 1856 was presented as 3 years of data taking at ATLAS and CMS at $10^{33} \text{ cm}^{-2} \text{s}^{-1}$, which was a
 1857 scenario with negligible overlap background. The 600 fb^{-1} scenario corresponds to 3 years of
 1858 data taking by both ATLAS and CMS at $10^{34} \text{ cm}^{-2} \text{s}^{-1}$. Figure 9.2 shows that a large region of
 1859 the $M_A - \tan\beta$ can be covered at the 3σ level given enough luminosity. For example, if $\tan\beta = 40$

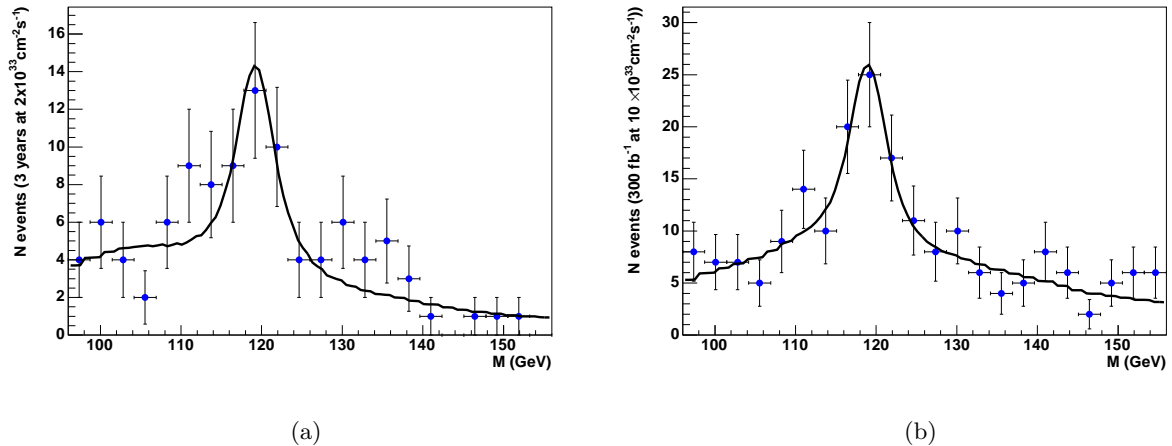


Figure 9.1: Typical mass fits for the 120 GeV/c² MSSM $h \rightarrow b\bar{b}$ for (a) 3 years of data taking at $2 \times 10^{33} \text{ cm}^{-2} \text{ s}^{-1}$ (60 fb⁻¹, 3.5 σ , 10 ps timing) and (b) 1.5 years of data taking at $7.5 \times 10^{33} \text{ cm}^{-2} \text{ s}^{-1}$ and 1.5 years of data taking at $10^{34} \text{ cm}^{-2} \text{ s}^{-1}$ (300 fb⁻¹, 4.5 σ , 5 ps timing).

1860 and $M_A = 120 \text{ GeV}/c^2$, then $h \rightarrow b\bar{b}$ would be observed with 3.8 σ significance with 60 fb⁻¹ of
 1861 data (upper plot). For $\tan\beta > 30$, the significance is 5 σ or above. Such a measurement would
 1862 provide a unique determination of the quantum numbers of the Higgs boson.

1863 It is also possible to test for CP-violation in the MSSM Higgs sector. The azimuthal asym-
 1864 metry in the outgoing tagged protons is expected to be quite sizable in some MSSM scenarios
 1865 [63, 64]. In addition, the cross sections can become so large in the MSSM that the excellent
 1866 mass resolution of the forward detectors could allow to distinguish between Higgs bosons that
 1867 are almost degenerate in mass, as shown for the tri-mixing scenario in [63].

1868 9.2.2 $h \rightarrow \tau\tau$

1869 In the MSSM, the branching ratio of the Higgs bosons to $\tau\tau$ is approximately 10% for $M_{H/A} >$
 1870 $150 \text{ GeV}/c^2$ if the decays to light SUSY particles are not allowed. The τ 's decay primarily to
 1871 1-prong (85%) or 3-prong (15%) track topologies; therefore requiring no additional tracks on
 1872 the $\tau\tau$ vertex is very effective at reducing non-exclusive background.

1873 The possibility of observing the Higgs boson through its decay to $\tau\tau$ was investigated in [62],
 1874 It was shown that the heavy neutral Higgs, H , can be observed at 3 σ in this channel across
 1875 a large area of the $M_A - \tan\beta$ plane; for $m_A \sim 120 \text{ GeV}$, the 3 σ contour extends as low as
 1876 $\tan\beta \sim 10$ and at higher masses, $m_A \sim 200 \text{ GeV}$, the $\tau\tau$ channel is observable for $\tan\beta > 40$.
 1877 The light Higgs boson, h , can be observed at 3 σ confidence for $m_A < 130 \text{ GeV}$ and $\tan\beta > 15$.

1878 9.2.3 $h \rightarrow 4\tau$

1879 The possibility of a Higgs boson decaying to 4τ arises in the NMSSM, which extends the MSSM
 1880 by the inclusion of a singlet superfield, \hat{S} [63]. The Higgs sector of the NMSSM contains three
 1881 CP-even and two CP-odd neutral Higgs bosons, and a charged Higgs boson. According to [65]
 1882 the part of parameter space that has no fine-tuning problems results in the lightest scalar Higgs
 1883 boson decaying predominantly via $h \rightarrow aa$, where a is the lightest pseudo-scalar. The scalar
 1884 Higgs boson has a mass of $\sim 100 \text{ GeV}/c^2$. If the a has a mass of $2m_\tau \lesssim m_a \lesssim 2m_b$, which is

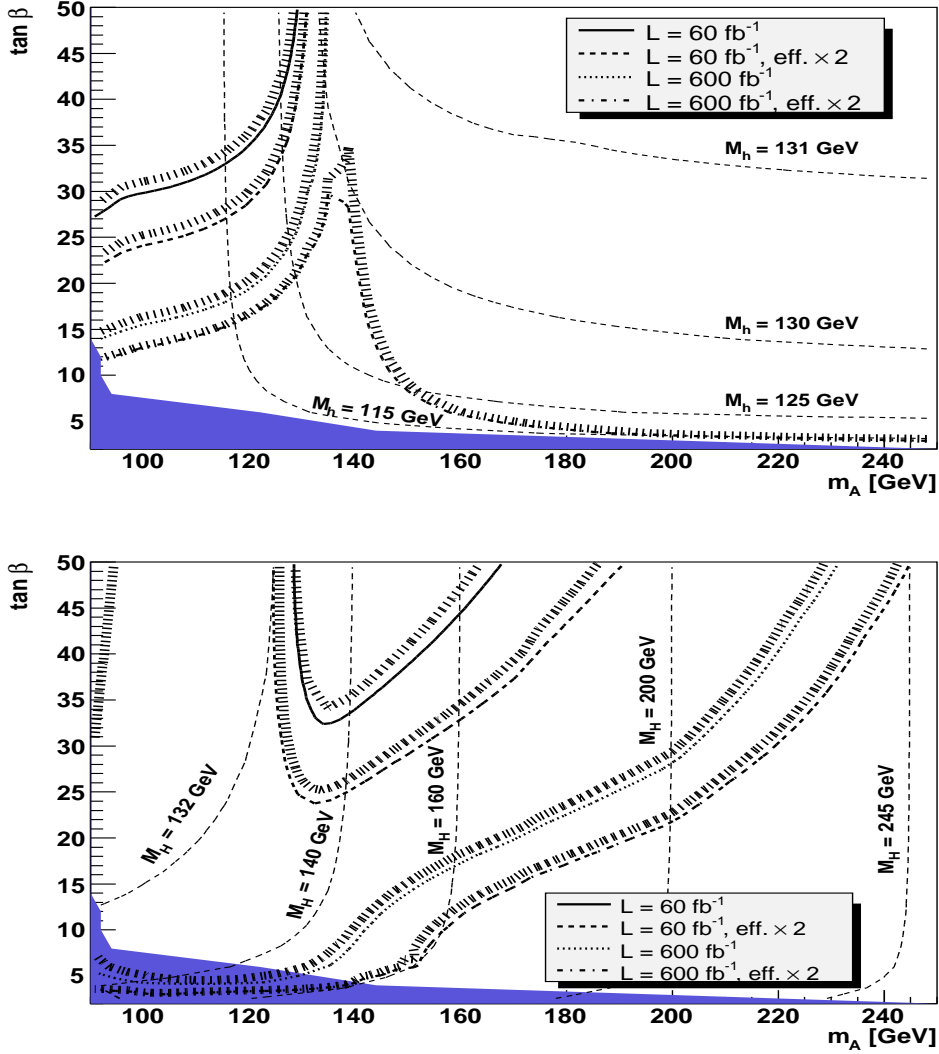


Figure 9.2: 3σ contours for $h \rightarrow b\bar{b}$ (upper plot) and $H \rightarrow b\bar{b}$ (lower plot) in the M_A - $\tan\beta$ plane of the MSSM within the M_h^{max} benchmark scenario (with $\mu = +200\text{GeV}$) for different luminosity scenarios as described in the text. The values of the mass of the Higgs bosons, m_h and M_H , are indicated by contour lines. Overlap background considered to be negligible. The dark shaded (blue) region corresponds to the parameter region that is excluded by the LEP Higgs boson searches.

1885 preferred on general theoretical grounds, then the decay channel $h \rightarrow aa \rightarrow 4\tau$ would become
1886 the dominant decay chain. This is not excluded by LEP data and in such a scenario the LHC
1887 could fail to discover any of the Higgs bosons [65].

1888 It was shown in [66] that the lightest Higgs boson could be discovered in CEP using forward
1889 proton detectors at ATLAS. It is expected that approximately 3-4 events will be retained (after
1890 all cuts) using a muon trigger of $p_T > 10$ GeV given three years of data taking if the instantaneous
1891 luminosity is greater than $10^{33} \text{ cm}^{-2} \text{ s}^{-1}$. The event rates double if a combination of lepton
1892 triggers are used [24]. There is no appreciable background. The mass of the h is obtained using
1893 the missing mass method to an accuracy of $2 - 3 \text{ GeV}/c^2$ (per event). Furthermore, using the
1894 kinematic information provided by the forward detectors and the tracking information from the
1895 central detector, it is also possible to make measurements of the a mass; in the above scenario
1896 the mass measurement is $9.3 \pm 2.3 \text{ GeV}/c^2$.

1897 9.2.4 Photon-Photon physics

1898 The increase in forward detectors acceptance will ensure high rates of dilepton events used
1899 for calibration of 420 m detectors and for the luminosity measurement as already discussed
1900 Section 2.3.1. The rates for SM WW two-photon production are greatly enhanced and the
1901 production can be measured right from the kinematic mass threshold.

1902 Easiest to observe experimentally are the fully leptonic decay channels; requiring no addi-
1903 tional tracks on the $l^+ l^-$ vertex, large lepton acoplanarity and large missing transverse momen-
1904 tum strongly reduces the backgrounds, such as $\gamma\gamma \rightarrow \tau^+ \tau^-$. The cross section for events where
1905 both W bosons decay into a muon or electron with $p_T > 25$ GeV and a neutrino $E_T^{\text{miss}} > 20$ GeV
1906 is $\sim 2\text{fb}$ if both protons are tagged in a forward detector at either 220m or 420m [4]. For 30 fb^{-1}
1907 collected at low luminosity, one would expect approximately 60 events. The double proton tag
1908 requirement is necessary at high luminosity in order to efficiently suppress the overlap back-
1909 ground from inclusive (partonic) WW production. Thus for 100 fb^{-1} , one would expect 200
1910 events with two proton tags. It was shown in [4] that the SM two-photon could be observed at
1911 5σ CL with thus 5fb^{-1} of data.

1912 It is possible to investigate the higher rate semi-leptonic decay channel, although further
1913 studies are required to determine the effect of the overlap background. It was shown in [9] that
1914 the production cross section has a sharp turn on at $\sim 2m_W$, which allows an *in situ* calibration of
1915 the absolute forward detector energy scale to much better than 1% given 100 fb^{-1} of data. This
1916 process is also an interesting probe of the $WW\gamma$ vertex. The coupling enters the cross section
1917 calculation to the fourth power and so should be extracted with less than 1% uncertainty given
1918 100 fb^{-1} of data. This constraint is competitive with the standard measurement from non-
1919 diffractive $W\gamma$ production and is insensitive to many of the systematics involved in that case.

1920 The opportunity to investigate anomalous gauge boson couplings in vector boson pair pro-
1921 duction is to some extent possible with 220 m detectors only. With combined detector acceptance,
1922 distributions of the background processes (arising from for example QCD double pomeron ex-
1923 change WW production) can be well measured and the contamination in the signal sample can
1924 be well determined by cut inversion methods. In this way the background will be determined
1925 from data and derived limits on anomalous gauge couplings coupling will be more robust.

1926 9.2.5 Supersymmetric particle production

1927 Exclusive two-photon production of new charged particles provides a simple mechanism for the
1928 production of new physics beyond the Standard Model. Two photon production of SUSY leptons
1929 has been investigated in [67] and the cross section for $\gamma\gamma \rightarrow \tilde{l}^+ \tilde{l}^-$ can be as large as 1 fb, while

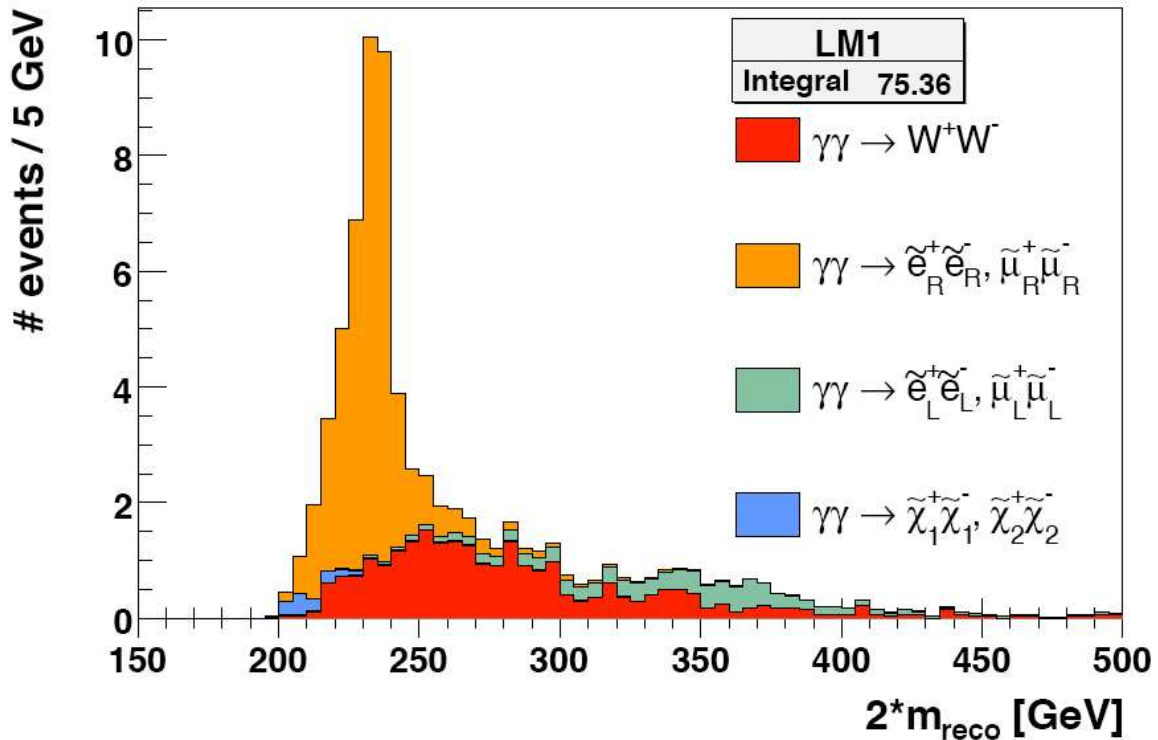


Figure 9.3: Distribution of the reconstructed mass for the LM1 SUSY signal and the WW background for an integrated luminosity of 100 fb^{-1} .

1930 remaining consistent with the direct search limits from LEP. The production via $\gamma\gamma$ fusion has
 1931 the added advantage over standard LHC production mechanisms of being a direct QED process,
 1932 with minimal theoretical uncertainties.

1933 In [67], the two-photon production of charged SUSY pairs is investigated for three benchmark
 1934 points in mSUGRA/CMSSM parameter space. The two-photon production of $\tilde{e}^+\tilde{e}^-$, $\tilde{\mu}^+\tilde{\mu}^-$,
 1935 $\tilde{\tau}^+\tilde{\tau}^-$ and charginos (χ_1, χ_2) in the fully leptonic decay channels are considered, which means
 1936 that the final state consists of two leptons and a large amount of missing energy carried by the
 1937 LSP and, in the case of $\tilde{\tau}/\chi$ pair production, neutrinos. Around 50 signal events with $S/B \sim 2$
 1938 in 100 fb^{-1} are expected depending on the benchmark point chosen. Results for the LM1 SUSY
 1939 point are shown in Figure 9.3.

1940 .

1941 9.3 New connection cryostat

1942 The LHC dispersion suppressor and arc magnets are placed in one continuous cryostat from the
 1943 Q7 quadrupole downstream of an IP, all the way to the Q7 quadrupole of the next IR [68].
 1944 At the position of the missing magnet of the dispersion suppressor, some 420 m downstream
 1945 of each IP, there is a 14 m long Connection Cryostat (CC) which contains cold beam-pipes,
 1946 the 2K heat exchanger, or X-line, and various cryo-lines which run throughout the continuous
 1947 cryostat. The CC also carries the superconducting busbars of the main bending magnets and
 1948 quadrupoles and nearly 100 superconducting cables for corrector magnets and other systems.

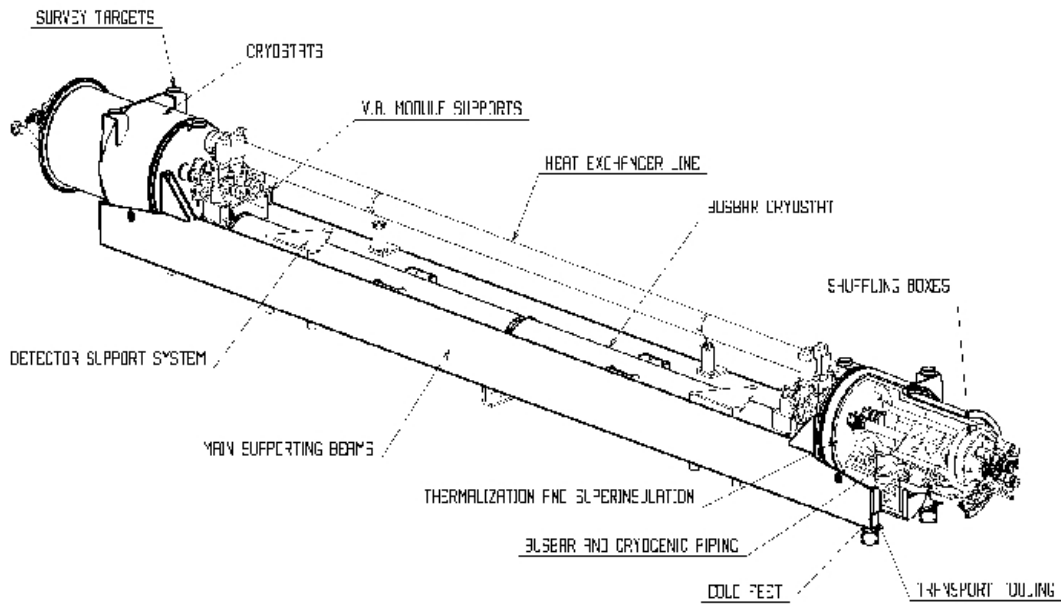


Figure 9.4: The new connection cryostat for FP420

1949 There are sixteen CCs in the LHC, each made to be as similar as possible to a standard dipole
 1950 magnet cryostat, at least as far as interconnection and handling are concerned. At this 420 m
 1951 point, the dispersion function D , with the standard high luminosity optics, is approximately 2 m
 1952 and hence protons from the IP which have lost around 1% of their momentum are well separated
 1953 from the circulating beam, as described in Chapter 8. In order to allow the use of near-beam
 1954 detectors at this 420 m position it is proposed to replace the existing connection cryostats on
 1955 each side of IP1 with a warm beam-pipe section and a cryogenic bypass. A New Connection
 1956 Cryostat (NCC) with approximately 8 m of room temperature beam-pipes has been designed
 1957 using a modified Arc Termination Module (ATM) at each end.

1958 In addition to two modified ATMs and warm beam-pipes, the NCC shown in Fig. 9.4 has a
 1959 small cross section cryostat below the beam-pipes carrying all the cryo-lines and superconduct-
 1960 ing circuits and a new specially designed cryostat for the X-line. All this is supported by two
 1961 longitudinal beams to make a single unit which can be directly exchanged for an existing con-
 1962 nection cryostat. The passage of the X-line through the ATM modules is the main modification
 1963 needed to the standard ATMs and the geometrical layout of this passage has been arranged to
 1964 be as far away as possible from the downstream beam-pipe in order to leave adequate space
 1965 for near-beam detectors and their associated equipment. The cross-section of the NCC, with
 1966 the space around the beam-pipes available for detectors and associated mechanics, is shown in
 1967 Fig. 9.5.

1968 The existing connection cryostat contains a box structure of lead plates of 15 mm thickness
 1969 enclosing the two beam-pipes to reduce the radiation field in the tunnel, essentially replacing
 1970 the shielding provided by the cold mass in a standard arc dipole cryostat. The same thickness of
 1971 lead shielding will be provided around the warm beam-pipes and detector stations of the NCC.

1972 There are also short lengths of cylindrical shielding in the form of collars around the beam-

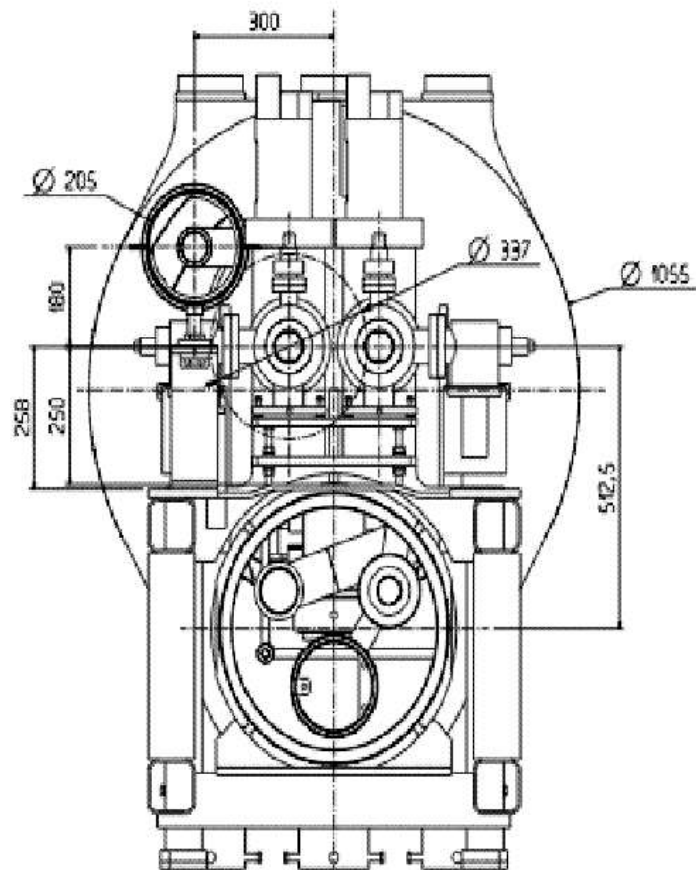


Figure 9.5: Cross-section view of the new connection cryostat for FP420

1973 pipes at each end of the existing connection cryostat to limit the risk of quenching adjacent
 1974 superconducting magnets. Similar collars will be incorporated into the modified ATM's at each
 1975 end of the NCC in order to ensure that the NCC is at least equal to the existing cryostat in
 1976 terms of influence on the local radiation fields and quench performance.

	Normal Days
Warmup from 1.9K to 4.5 K	1
Warmup from 4.5K to 300 K	15
Venting	2
Dismantling interconnection	10
Removal of the connection cryostat	2
Installation of the FP420 cryostat	5
Realization of the interconnections	15
Leak test and electrical test	4
Closing of the vacuum vessel	1
Evacuation/repump	10
Leak test	2
Pressure test	4
Cooldown from 300 K to 4.5 K	15
Cooldown from 4.5K to 1.9 K	3
Total [days]	89

Table 9.1: The estimated time in days required to install one NCC

1977 The final engineering design of the new connection cryostat still has to be completed in the
 1978 CERN central design office of the TS/MME group. The design aim is to meet or exceed the
 1979 same specifications as the existing connection cryostat, whilst providing the maximum useable
 1980 space for the silicon and timing detectors at 420 m. The preliminary design offers acceptable
 1981 solutions for all cryogenic and mechanical engineering aspects as well as integration into the
 1982 LHC environment [69, 70]. The final cryogenic performance will depend on the detailed design,
 1983 but it has already been established that the additional static heat load arising from the two
 1984 additional cold to warm transitions will be tolerable for the LHC cryogenic system. During
 1985 LHC operation, simulations show that the NCC actually contributes a slightly lower dynamic
 1986 heat load than the existing connection cryostat, because in the 8 m long warm section some
 1987 synchrotron radiation is being absorbed at room temperature.

1988 Since the completion of the preliminary design of the NCC the LHC collimation group have
 1989 finalised their stage II collimator requirements and work has started on the construction of
 1990 so-called 'cryo-collimators' for IR3, to be installed in the 2012/2013 long shutdown. The cryo-
 1991 collimators are to be installed in what are currently cold sections of the LHC and a new cryo
 1992 by-pass has been designed and is already under construction, based on similar ideas to the
 1993 NCC [72] as shown in Fig. 9.6. In view of this it is now intended to base the final NCC design
 1994 on the components of the new LHC cryo by-pass. Because the new collimators must be installed
 1995 in the shortest possible beam length the original ATM based design used for the NCC has been
 1996 abandoned and a new cold to warm transition designed in only 1.25 m. The new cryo by-pass
 1997 provides 1.7 m of warm beampipe for the collimators in an over-all length of 4.2 m. Adapting
 1998 this new mechanical concept to the NCC design should thus increase the distance available for
 1999 detector stations by up to two metres, but the increased thermal contraction of the 14 m long
 2000 NCC, compared to the 4.2 m by-pass, will have to be correctly taken into account and the

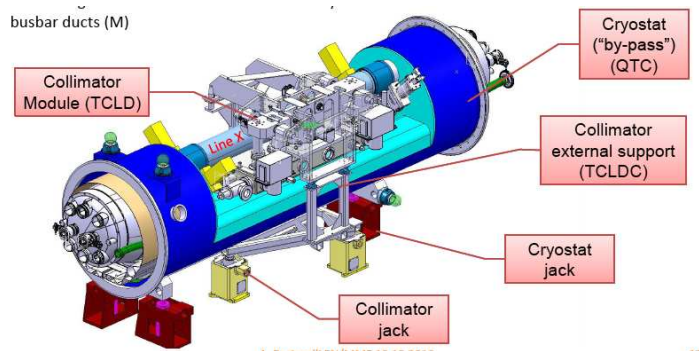


Figure 9.6: Schematic view of the cryo-bypass and collimator (Courtesy of V. Parma).

2001 horizontal displacement of the X-line needed to allow access to the detectors will have to be
 2002 made by means of dog-legs in the warm section. Both of these modifications should be straight-
 2003 forward, but will reduce the gain in space along the beamline. It also has to be noted that the
 2004 cryo by-pass leaves only 100 mm below the beampipes for the collimator support and moving
 2005 mechanism. This same distance was 250 mm with the preliminary NCC and hence the free
 2006 space available has to be increased for the final NCC or the moving beampipe system will have
 2007 to adopt the new collimator support and moving system. The latter solution would be preferable
 2008 from the LHC machine point of view, but both possible solutions require a detailed engineering
 2009 study. It has to be noted that the increased distance was needed to allow the detectors to be
 2010 mounted on a separate table for stability and alignment reasons. Finally it is clear that the
 2011 construction and installation of the cryo by-passes in the LHC in 2013 will greatly simplify the
 2012 preparation and work needed to construct and install NCC's in 2016. While more design work
 2013 will be needed to finalise the NCC's, all engineering solutions will have been checked out on
 2014 the LHC and methods of construction and installation tried and tested. The cost of the NCC's
 2015 should also be reduced [71].

2016 The cutting and removal of the existing connection cryostat and its replacement by an NCC
 2017 is very similar to the replacement of a standard LHC dipole and the task has been evaluated
 2018 by the group responsible for all the LHC interconnections. Table 9.1 shows the sequence of
 2019 operations and the estimated time needed in normal working days to complete the exchange of
 2020 a connection cryostat from start of warm-up to being ready for beam. It is thus conceivable
 2021 that the installation of an NCC cryostat and near-beam detectors could be completed in a three
 2022 month shutdown. A preliminary study of the transport aspects has shown that adequate tooling
 2023 exists and it can be expected that the time needed will be in the shadow of other operations
 2024 shown in Table 9.1. However, the number of Connection Cryostats that can be replaced in any
 2025 one shutdown will depend on the work load of the interconnection teams.

2026 9.4 Summary

2027 In summary, a preliminary design for a replacement connection cryostat that would allow near
 2028 beam detectors to be placed in the 420 m region has been completed, and a final design can
 2029 profit from the new cryo bypasses being installed in IR3 in 2013. The solution proposed is
 2030 expected to have an acceptable cryogenic performance and give similar radiation profiles in
 2031 the region. With the appropriate approvals and funding, two such cryosats could be built and
 2032 ready for installation in the long shutdown of 2016, with negligible risk to LHC operations and
 2033 performance for physics.

2034

Bibliography

- 2035 [1] A. Brandt, B. Cox, C. Royon *et al.* [AFP Collaboration], “Letter of Intent for ATLAS FP: A
2036 Project to Install Forward Proton Detectors at 220 m and 420 m Upstream and Downstream
2037 of the ATLAS Detector,” http://jenni.web.cern.ch/jenni/AFP.loi_atlas.pdf.
- 2038 [2] <http://www-hep.uta.edu/~brandta/ATLAS/AFP/AFP.html>
- 2039 [3] V. M. Budnev, I. F. Ginzburg, G. V. Meledin and V. G. Serbo, Phys. Rept. **15** (1974) 181.
- 2040 [4] E. Chapon, O. Kepka, C. Royon, Phys. Rev. **D81** (2010) 074003; O. Kepka and C. Royon,
2041 Phys. Rev. D **78** (2008) 073005.
- 2042 [5] J. de Favereau de Jeneret *et al.*, arXiv:0908.2020 [hep-ph].
- 2043 [6] A. Bialas and P. V. Landshoff, Phys. Lett. B **256** (1991) 540.
- 2044 [7] V. A. Khoze, A. D. Martin and M. G. Ryskin, Eur. Phys. J. C **23** (2002) 311; V. A. Khoze,
2045 A. D. Martin, R. Orava and M. G. Ryskin, Eur. Phys. J. C **19** (2001) 313; A. B. Kaidalov,
2046 V. A. Khoze, A. D. Martin and M. G. Ryskin, Eur. Phys. J. C **33**, 261 (2004); V. A. Khoze,
2047 A. D. Martin and M. G. Ryskin, Eur. Phys. J. C **19** (2001) 477 [Erratum-ibid. C **20** (2001)
2048 599].
- 2049 [8] J. R. Cudell, A. Dechambre, O. F. Hernandez, arXiv 1011.3653; J. R. Cudell, A. Dechambre,
2050 O. F. Hernandez, I. P. Ivanov, Eur. Phys. J. C **61** (2009), 369; A. Dechambre, O. Kepka,
2051 C. Royon, R. Staszewski, arXiv:1101.1439.
- 2052 [9] M. Boonekamp, R. Peschanski, C. Royon, Phys. Rev. Lett. **87** (2001) 251806; Nucl. Phys.
2053 **B669** (2003) 277; Phys. Lett. **B598** (2004)243; M. Boonekamp, A. De Roeck, R. Peschan-
2054 ski, C. Royon, Phys. Lett. **B550** (2002) 93; M. Boonekamp, C. Royon, J. Cammin and
2055 R. B. Peschanski, Phys. Lett. B **654** (2007) 104 [arXiv:0709.2742 [hep-ph]].
- 2056 [10] T. Aaltonen *et al.* [CDF Run II Collaboration], arXiv:0712.0604 [hep-ex]; T. Aaltonen *et*
2057 *al.* [CDF Collaboration], Phys. Rev. Lett. **99** (2007) 242002
- 2058 [11] A. Abulencia *et al.* [CDF Collaboration], Phys. Rev. Lett. **98** (2007) 112001.
- 2059 [12] K. Piotrkowski, Phys. Rev. **D63** (2001) 071502.
- 2060 [13] G. Abbiendi *et al.* [OPAL Collaboration], Phys. Rev. D **70** (2004) 032005
- 2061 [14] P. J. Bell, Eur. Phys. J. C **64** (2009) 25 [arXiv:0907.5299 [hep-ph]].
- 2062 [15] C. Grojean (CERN & Saclay, IPhT), James D. Wells (CERN & Michigan U., MCTP),
2063 private communication.

2064
2065
2066
2067
2068
2069
2070
2071
2072
2073
2074
2075
2076
2077
2078
2079
2080
2081
2082
2083
2084
2085
2086
2087
2088
2089
2090
2091
2092
2093
2094
2095
2096
2097
2098
2099
2100

[16] A. Brandt *et al.* [UA8 Collaboration], Phys. Lett. B **297** (1992) 417.

[17] V. Barone and E. Predazzi, *High-energy particle diffraction*, Springer, 2002.

[18] S. Alekhin *et al.*, “HERA and the LHC - A workshop on the implications of HERA for LHC physics: Proceedings Part B”, arXiv:hep-ph/0601013.

[19] M. Arneodo and M. Diehl, “*Diffraction for non-believers*”, hep-ph/0511047 (2005).

[20] M. Albrow *et al.* [CMS and TOTEM Collaborations], CERN-LHCC-2006-039; The FP420 R&D Project: Higgs and New Physics with forward protons at the LHC, JINST 4 T10001, hep-ex/0806.0302 (June 2008), accepted in J. Inst.: <http://www.iop.org/EJ/abstract/1748-0221/4/10/T10001>.

[21] M. Deile *et al.*, arXiv:1002.3527 [hep-ph], page 6.

[22] V. A. Khoze, A. D. Martin and M. G. Ryskin, Eur. Phys. J. C **18** (2000) 167 [arXiv:hep-ph/0007359].

[23] K. Piotrzowski, U. Schneekloth, Proc. of the ZEUS Collaboration Meeting, March 1994, DESY, Hamburg.

[24] M. G. Albrow *et al.* [FP420 R&D Collaboration], arXiv:0806.0302 [hep-ex].

[25] A. Guerrero *et al.*, “CERN front-end software architecture for accelerator controls,” (ICALEPCS 2003), Korea, Oct 2003. in Gyeongju 2003, Accelerator and large experimental physics control systems, p. 342.

[26] M. Slater *et al.*, “Cavity BPM tests for the ILC energy spectrometer”, SLAC-PUB-13031.

[27] S. Walston *et al.*, “Performance of a High Resolution Cavity Beam Position Monitor System”, unpublished.

[28] CERN-LHCC-2010-013 / ATLAS-TDR-019 5/09/2010 <https://espace.cern.ch/atlas-ib1/Shared%20Documents/ATLAS-TDR-019.pdf>; <http://indico.cern.ch/conferenceDisplay.py?confId=127>

[29] T. E. Hansen *et al.*, First Fabrication of Full3D Detectors at SINTEF, JINST 4 (2009) P03010.

[30] G. Pellegrini *et al.*, First Double-Sided 3-D Detectors Fabricated at CNM-IMB, Nucl. Inst. Meth. **A592** (2008) 38.

[31] S. Parker, C. Kenney and J. Segal, 3D-A proposed New Architecture for Solid-State Radiation Detectors, Nucl. Inst. Meth. **A395** (1997) 328.

[32] C. Kenney *et al.*, Silicon detectors with 3-D electrode arrays: fabrication and initial test results, IEEE Tr. Nucl. Sci **46** (1999) 1224.

[33] M. Mathes *et al.*, Test Beam Characterizations of 3D Silicon Pixel Detectors, IEEE Tr. Nucl. Sci 55 (2008) 3731.

[34] P.O. Hansson *et al.*, 3D Silicon Pixel Sensors: Recent Test Beam Results, Nucl. Inst. Meth. **A321** (2010).

[35] C. Da Via *et al.*, 3D Active Edge Silicon Sensors with Different Electrode Configurations: Radiation Hardness and Noise Performance, Nucl. Inst. Meth. **604** (2009) 505.

- 2101 [36] G. Aad et al., ATLAS Pixel Detector Electronics and Sensors, JINST **3** (2008) P07007.
- 2102 [37] A. Lounis et al., TCAD Simulations of the ATLAS Pixel Ring and Edge Structure for
2103 SLHC Upgrade, Internal Report ATL-UPGRADE-PUB-2010-001, ATL-COM-UPGRADE-
2104 2009-013, CERN, Geneva, Jan 2010.
- 2105 [38] G. Kramberger et al., Comparison of Pad Detectors Produced on Different Silicon Materials
2106 after Irradiation with Neutrons, Protons and Pions, Nucl.Inst.Meth. **A 612** (2010) 288.
- 2107 [39] L. Andricek et al., Processing of Ultra-Thin Silicon Sensors for Future Linear Collider
2108 Experiments, IEEE Tr. Nucl. Sci **51** (2004) 1117.
- 2109 [40] L. Andricek et al., Nucl. Inst. Meth. (2010) in press, In Proc. of 7th International Hiroshima
2110 Symposium on Development and Applications.
- 2111 [41] I. Mandic et al., Observation of Full Charge Collection Efficiency in Heavily Irradiated n+p
2112 strip Detectors Irradiated up to 3×10^{15} n(eq)/cm², Nucl. Inst. Meth. **A612** (2010) 474.
- 2113 [42] G. Casse et al., Enhanced Efficiency of Segmented Silicon Detectors of Different Thicknesses
2114 After Proton Irradiations up to 1×10^{16} n(eq)/cm², Nucl. Inst. Meth. In Press (2010).
- 2115 [43] E. Mandelli et al., IEEE Trans. Nucl. Sci. **49** (4) (2002) 1774.
- 2116 [44] L. Blanquart et al., IEEE Trans. Nucl. Sci. **49** (4) (2002) 1778.
- 2117 [45] L. Blanquart et al., IEEE Trans. Nucl. Sci. **51** (4) (2004) 1358.
- 2118 [46] ATLAS Collab., JINST **3** (2008) P07007.
- 2119 [47] CMS Collab., NIM **A 552** (2005) 232.
- 2120 [48] P-909: <http://www.cdf.fnal.gov/upgrades/btb.proposal.ps>.
- 2121 [49] M. Akatsu, *et al.*, Nucl. Instr. and Meth. **A 440** (2000) 124; M. Akatsu, *et al.*, Nucl. Instr.
2122 and Meth. **A 528** (2004) 763; Y. Enari, *et al.*, Nucl. Instr. and Meth. **A 547** (2005) 490.
- 2123 [50] L. Bonnet, T. Pierzchala, K. Piotrkowski, P. Rodeghiero. Acta Phys. Polon. **B38** (2007)
2124 477-482; hep-ph/0703320.
- 2125 [51] CERN/LHCC 2002-016 Addendum to the ALICE TDR 8, 24 April 2002.
- 2126 [52] http://www.nightvision.com/products/military/case_study-gen3.htm
- 2127 [53] N. Kishimoto, *et al.*, Nucl. Instr. and Meth. **A 564** (2006) 204; T. Mori, "Life-
2128 time of HPK Square-shape MCP-PMT," Cracow Fast Timing Workshop, Dec. 2010
2129 (<http://www-d0.fnal.gov/royon/timing-cracow/>).
- 2130 [54] I. Baichev, J.-B. Jeanneret and G.R. Stevenson, *Beam losses far downstream of the high*
2131 *luminosity interaction points of LHC - intermediate results*, LHC-Project Note 208, CERN,
2132 2000
- 2133 [55] E. Forest, F. Schmidt and E. McIntosh, "Introduction to the Polymorphic Tracking Code",
2134 CERN-SL-2002-044-AP, KEK report 2002-3, July 2002.
- 2135 [56] R. Assmann *et al.*, The proceedings of PAC03, pag. 3496.

- 2136 [57] The LHC design report, CERN-2004-003 (2004)
- 2137 [58] P.J. Bussey and W. Plano, FPTrack, in preparation.
- 2138 [59] J. Monk and A. Pilkington, *Comput. Phys. Commun.* **175** (2006) 232 [arXiv:hep-
2139 ph/0502077]; M. Boonekamp, A. Dechambre, V. Juranek, O. Kepka, M. Rangel, C. Royon,
2140 R. Staszewski, [arXiv:1102.2531].
- 2141 [60] R Staszewski et al., ATL-COM-LUM-2009-016, *Nucl. Instr. Meth. A* **609** (209) 136
- 2142 [61] M. G. Albrow and A. Rostovtsev, arXiv:hep-ph/0009336.
- 2143 [62] B. Cox, F. Loebinger, A. Pilkington, *JHEP* **0710** (2007) 090; S. Heinemeyer et al.,
2144 *Eur. Phys. J. C* **53** (2008) 231.
- 2145 [63] J. R. Ellis, J. F. Gunion, H. E. Haber, L. Roszkowski and F. Zwirner, *Phys. Rev. D* **39**
2146 (1989) 844; J. R. Ellis, J. S. Lee and A. Pilaftsis, *Phys. Rev. D* **71** (2005) 075007 [arXiv:hep-
2147 ph/0502251].
- 2148 [64] V. A. Khoze, A. D. Martin and M. G. Ryskin,
- 2149 [65] R. Dermisek, J.F. Gunion. *Phys. Rev. Lett.* **95** (2005) 041801. *Eur. Phys. J. C* **34** (2004)
2150 327
- 2151 [66] J. R. Forshaw, J. F. Gunion, L. Hodgkinson, A. Papaefstathiou and A. D. Pilkington, *JHEP*
2152 **0804** (2008) 090 [arXiv:0712.3510 [hep-ph]].
- 2153 [67] J. Ohnemus, T.F. Walsh and P.M. Zerwas, *Phys. Lett. B* **328** (1994) 369-373; G. Bhat-
2154 tacharya *et al.*, *Phys. Rev. D* **53**, (1996) 2371; M. Drees *et al.*, *Phys. Rev. D* **50**, (1994)
2155 2335; N. Schul and K. Piotrkowski, arXiv:0806.1097.
- 2156 [68] “LHC Design Report Vol. 1”, CERN-2004-003, CERN, Geneva, Switzerland (2004).
- 2157 [69] T. Columbet, “Cryogenics preliminary calculation for the FP420 cryostat”,
2158 <https://edms.cern.ch/document/827775>.
- 2159 [70] S. Pattalwar *et al.* “A New Connection Cryostat to insert FP420 Proton Tagging Detectors
2160 in the LHC Ring”, *Proceeds APAC* (2007) 103.
- 2161 [71] R. Folch, “FP420 Cryostat Modules Workpackage”,
2162 <https://edms.cern.ch/document/823322>.
- 2163 [72] V. Parma, talk at the Chamonix Workshop, January 2011.